Novel Lithium Ionic Conducting Perovskite Materials for Lithium-Air Batteries

Muneerah Almohareb

uOttawa

Thesis Submitted to the Faculty of Graduate and Postdoctoral Studies as Part of the Requirement for the M.Sc. Degree in Chemistry

Department of Chemistry and Biomolecular Sciences, Faculty of Science, University of Ottawa

Supervisor: Javier Giorgi

117 D'Iorio Hall, 10 Marie Curie, Ottawa ON Canada, K1N 6N5

DEDICATION

For my mother who taught me how to live the life, for my father who said in one day " Oh Muneerah; when can I see you as a doctor" one big step is left my dad, for my husband Badr who loves, helps and supports me all of the time, for my boys Naif and Fahd who I will never give up to love and support them, for my friend Salimah who shared with me this period of my study…

Thank you for being in my life

ACKNOWLEDGMENT

This present thesis could not be done without numerous support and encouragement. First of all, I would like to thank King Abdullah bin Abdul-Aziz program for external scholarship administered by Saudi cultural bureau in Canada to support me financially to study and live in Canada. Secondly, I would like to express my gratitude to my supervisor Dr. Javier Giorgi for accepting me in his lab and giving me the opportunity to be one of the chemistry students in this great scientific edifice at the University of Ottawa. Additionally, many thanks and appreciations are directly to him for his patience, support, encourage and help during the period of my study. I would also like to thank Dr. Abdelhamid Sayari and Dr. Paul Mayer for being a part of my thesis committee. I would provide my appreciations Dr. Yun for helping me on SEM/EDS, and Dr. Wendy Pell for working with me in the IES and her important and suitable knowledge in the electrochemistry field. Also, I would like to thank Dr. Nike Alderman how give me his time and explain to me how to run a sample in XRD, and Dr. Bulat Gabidullin for helping me in XRD analysing software.

Finally, Thanks to All

TABLE OF CONTENT

LIST OF FIGURES

Figure 2. 4: The cycle performance of the Li-O_2 cells with pristine Li electrode (Red), PEDOT-PEG coated Li electrode (Blue) and PEDOT-PEG/AlF_3 coated Li electrode (Green) at a limited capacity of 1000 mAh/g, with permission from reference [34].

Figure 2. 5: Voltage profiles for cycle number 1, 2, 5, 8, 10 and 15 of a lithiated-silicon/carbon-oxygen cell (Li_xSi/O_2) carried out at a 1000 mAh/g of carbon, with permission from reference [35].

Figure 2. 6: A diagram representation for two Models of the reaction zones for catalytic ORR. (a) The model for aqueous electrolyte-based cell with "three phase reaction zone" and (b) The model for Non-aqueous electrolyte-based cell with "two phase reaction zone, adapted from reference [41].

Figure 2. 7: The discharge curves of lithium air cells with different electrolytes in ambient atmosphere at the discharge current density of 0.02 mA cm^{-2}. The electrolytes are (A) LiTFSI-PMMITFSI based non-catalyzed lithium air battery (solid), (B) LiTFSI-PMMITFSI–silica–PVdF-HFP polymer composite electrolyte based non-catalyzed lithium air battery (dash) and (C) LiTFSI-PMMITFSI–silica–PVdF-HFP polymer composite electrolyte based on α-MnO_2 catalyzed lithium air battery (dot), adapted from reference [53].

Figure 2. 8: (a) A diagram of the proposed lithium air cell, (b) The cycling performance of the oxygen evolution electrode at a low current density of 0.1 mA/cm^2, adapted from reference [66].

Figure 2. 9: (a) SEM image of the porous anodized aluminum oxide (AAO) filter after thin film deposition using electron beam evaporation and (b) SEM image of the AAO filter after Nano fiber growth, adapted from reference [78].

Figure 2. 10: "(a) Schematic structure of a functionalized graphene sheet (upper

Figure 5. 9: Magnified region for the XRD patterns of all samples fired at 1350°C and the Standard $SmFeO_3$ perovskite (01-086-1330) and $LiFeO_2$ phase (01-070-2711).

Figure 5. 10: SEM images for all SLFO* Perovskites presented in LEI and COMPO modes, a) and b) for $Sm_{0.3}Li_{0.6}FeO_{3-\delta}$, c) and d) for $Sm_{0.3}Li_{0.5}FeO_{3-\delta}$, e) and f) for $Sm_{0.4}Li_{0.4}FeO_{3-\delta}$, g) and h) for $Sm_{0.5}Li_{0.3}FeO_{3-\delta}$ and i) and j) for $Sm_{0.6}Li_{0.3}FeO_{3-\delta}$. a, c, e, g, i obtained by LEI detection; b, d, f, h, j collected by COMPO detection. Areas marked in red correspond to locations where EDS measurements were performed.

Figure 5. 11: Nyquist plots present the AC data measurement points in red color and the calculated fitting curve in green color for the second group of lithium perovskites SLFO* calcined at 1350°C for 6 h.

Figure 5. 12: Lithium Ionic conductivity and atomic lithium concentration for $Sm_{(x)}Li_{([1-x]-[0.1]\text{ or }[0.2])}FeO_{3-\delta}$, where (x = 0.3, 0.4, 0.5 and 0.6).

LIST OF TABLES

LIST OF ABBREVIATIONS

AC / Alternative current

C_{dl} / Double layer capacitance

COMPO / Composition image

C_{sei} / Solid-state interface layer capacitor

EDS / Energy dispersive x-ray spectroscopy

EIS / Electrochemical impedance spectroscopy

L / Inductor

LEI / Low secondary electron image

LLTO / Lanthanum lithium titanate

Li-O_2 / Lithium-air

PXRD / Powder x-ray diffraction

Q_{dl} / Constant Phase element for the double layer

Q_{gb} / Constant Phase element for grain boundary

r_A / Ionic radius of the A-site

r_B / Ionic radius of the B-site

R_b / Bulk resistance

R_{ct} / Charge transfer resistance

R_{gb} / Grain boundary resistance

r_O / Ionic radius of oxygen ion

R_{sei} / Solid-state interface layer resistance

ROS / Relative oxidation state

S / Siemens = Ω^{-1}

SEM / Scanning electron microscopy

SFO / Samarium ferrite

SLFO / Samarium lithium ferrite without vacancies

SLFO* / Samarium lithium ferrite with vacancies

SSR / Solid state reaction

t / Tolerance factor

XRD / X-ray diffraction

Z' / Real part of impedance

Z'' / Imaginary part of impedance

n / The order of the diffraction peak (1, 2, 3, etc.)

λ / The wavelength of the x-ray radiation

d / The spacing of the crystal layers

θ / The incident angle (the angle between incident ray and the scatter plane)

ABSTRACT

Lithium Air (Li/O_2) batteries are energy conversion devices that produce electricity from the oxidation of lithium metal at the anode and the reduction of molecular oxygen at the cathode. These batteries are considered as promising rechargeable cells for high power applications due to their high power density ranging from 1000 to 2000 Wh/kg. However, one of the most significant challenges is the need to separate the metallic lithium anode from any oxygen or water-containing environment while at the same time allowing fast and efficient lithium ion transport through the electrolyte. Therefore, lithium ion conducting materials that are water and CO_2 resistant are a prerequisite.

Common materials used as anode protective films and/or Li^+ conducting electrolytes for lithium air batteries are perovskite-type oxides (formula: ABO_3). Perovskites are good candidates for this application because of their versatility, particularly in regards to ionic conductivity. In the present work, a low cost perovskite family such as SFO ($SmFeO_3$) is developed as a lithium ion conducting material by the introduction of Li^+ into its lattice.

The perovskites have been synthesized using a solid-state reaction method (SSR) and characterized using different techniques such as powder X-ray diffraction (PXRD), scanning electron microscopy (SEM), energy dispersive X-ray Spectroscopy (EDS) and electrochemical impedance spectroscopy (EIS). The synthesized perovskites are based on samarium lithium ferrite and divided into two groups depending on the formal presence of vacancies in the stoichiometric formula. The first group (SLFO) with no formal vacancies has the stoichiometric formula of $Sm_xLi_{1-x}FeO_{2+x}$ (where x = 0.1, 0.2, 0.3, 0.5 and 0.7). While the second group (SLFO*) was generated with less metal atoms than specified in the perovskite structure, thereby

generating a structure with intrinsic vacancies and with the formula, $Sm_{(x)}Li_{([1-x] - [0.1] \text{ or } [0.2])}FeO_{3-\delta}$ (where x = 0.3, 0.4, 0.5 and 0.6). Finally, the effect of varying Li and Sm concentrations in both groups and vacancies created in the lattice for the second group, on the ionic conductivity is explored.

THESIS OUTLINE

The thesis is divided into six chapters:

- **Chapter 1** introduces the perovskite type oxide materials having the general formula ABO_3. It also gives a brief description of the work carried out in the present study.
- **Chapter 2** gives an introduction to the lithium-air batteries and an extensive literature review on its primary components, which are anode, electrolyte, and cathode.
- **Chapter 3** focuses on the experimental consideration for the lithium perovskites, the synthesis method and the characterization techniques used to analyze the samples.
- **Chapter 4** describes the results obtained for the first group of the lithium samarium iron oxides $Sm_xLi_{1-x}FeO_{2+x}$ (where x = 0.1, 0.2, 0.3, 0.5 and 0.7). In addition, it discuses the effect of amount of lithium ions added to perovskite lattice on the ionic conductivity of the synthesized perovskites.
- **Chapter 5** contains the results and the discussion for the second group of the lithium samarium iron oxides $Sm_{(x)}Li_{([1-x]-[0.1]\text{ or }[0.2])}FeO_{3-\delta}$ (where x = 0.3, 0.4, 0.5 and 0.6). Moreover, it explains the impact of using different amounts of lithium ions and corresponding vacancies on the lithium ionic conductivity for these perovskites.
- **Chapter 6** presents the conclusions of the present study and proposes some developments for future work on the Li-perovskites.

Chapter 1

Introduction

1. 1 Thesis objective:

The goal of the present work is to study the synthesis and characterization of new perovskite materials that are cost-effective and highly lithium ionic conducting. Such materials can be used as a protective layer on the lithium metal surface in the rechargeable non-aqueous lithium air batteries. The reason to use this layer is to protect the lithium metal from the unwanted reactions and the dendrites inside the non–aqueous electrolyte.

To achieve this goal, perovskite oxides **(ABO_3)** were chosen for this work due to their tunability for ionic and electronic conductivity. For this, lithium ions were inserted into the lattice of the samarium ferrite family $SmFeO_3$ **(SFO)** to get high lithium ionic conductivity. Ten synthesized perovskites were divided into two groups and each group contains five Li perovskites. The perovskites in the first group were synthesized using different amount of Li and Sm ions at the A-site, with formula **$Sm_{[x]}Li_{[1-x]}FeO_{2+x}$ (SLFO)** where (x= 0.1, 0.2, 0.3, 0.5 and 0.7). While the perovskites in the second group were prepared in the same way as the first group perovskites, however, additional vacancies were created at the A-site of the perovskite, following this formula **$Sm_{[x]}$ $Li_{([1-x]\ -\ [0.1]\ or[0.2])}$ $FeO_{3-\delta}$ (SLFO*)** where (x= 0.3, 0.4, 0.5 and 0.6).

This task comprises the following stages:

- Synthesis and characterization of new low cost $SmFeO_3$ perovskite family by inserting Li ions into the perovskite lattice.

- Study the impact of lithium ion amount that is inserted into the perovskite lattice on the lithium ionic conductivity of the perovskites.
- Study the effect of number of vacancies added to the A-site that increase the lithium ionic conductivity in the perovskites.

The remaining of this chapter and the next will review the literature pertinent to the project. The aim is not to list the extensive number of studies regarding perovskites, but rather to focus on previous work that helps discuss and clarify the present thesis work.

1. 2 Perovskites:

1. 2. 1. Definition and Historical Background:

Perovskites are the series of compounds that have the same crystal structures as the mineral perovskite $CaTiO_3$ and have a general formula of ABO_3. Gustav Rose discovered the first perovskite in 1839, which was later named after the Russian mineralogist Lev A. Perowski [1]. The perovskite structure has been widely studied because altering the constituent elements at the A and/or B sites greatly influences its physical and electronic properties. In addition, perovskite materials further exhibit more properties like ferromagnetism, magneto-resistance, super conductivity and ionic conductivity, which are crucial parameters in designing innovative technologies [1]. However, the structures of perovskite-type oxide materials were not well characterised before the 1980's [2]. Later on, many theoretical and experimental works have been performed to understand the structure and properties of perovskites containing oxygen vacancies and/or cations with mixed valencies. These studies were focused on improving the ionic and electronic properties of the perovskite materials that are very important for many different applications such as batteries, solid oxide

fuel cells (SOFCs) and oxygen sensors [1, 3]. Moreover, the essential properties of perovskites are strongly related to subtle structural variations. For instance, varying the degree of octahedral orientation in a perovskite changes the extent of orbital overlap through the BO_6 octahedral network. This slight change highly affects its electronic properties such as conductivity, magnetism and certain dielectric properties [4].

1. 2. 2. The Crystal Structure of the Perovskites:

In an ideal cubic-symmetry structure, the A cations are at the corners of the cube and correspond to cations with a large ionic radius, such as Ca, Sr, Ba or Ln (rare-earth element). These cations are connected to 12 oxygen atoms, which are at the face center position of the lattice. While the B position is occupied by small transition-metal elements in 6-fold coordination and appear at the center of the cube with the oxygen ions forming a corner sharing octahedral network BO_6, as shown in **(figure 1. 1)** [5].

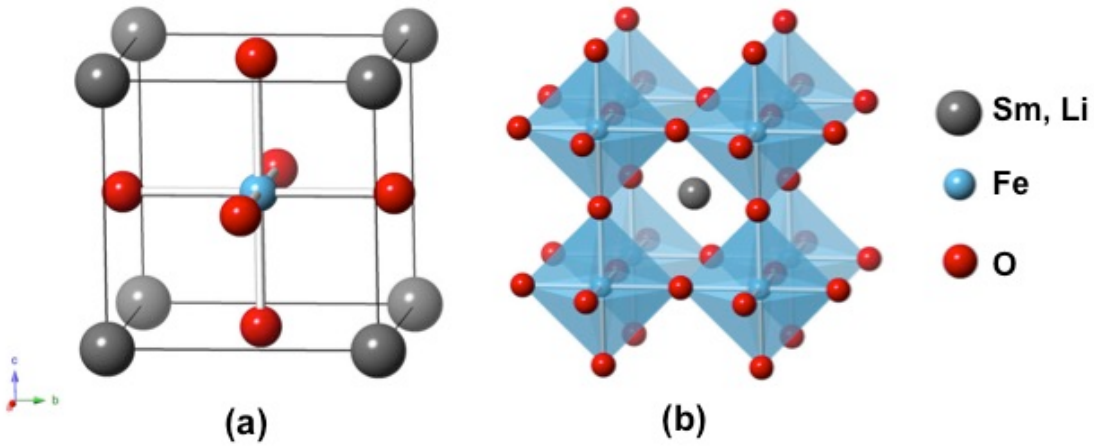

Figure1. 1: "The ideal cubic structure of the ABO_3 perovskite oxides, (a) is the lattice and (b) is the polyhedral", adapted from reference [5].

The perovskite compounds have attracted attention in the last five decades since they can accommodate almost all the elements in the periodic table. The elements in perovskite structures can be selected in a flexible manner, from numerous types and with different concentrations. In addition, it is possible to have a variety of perovskite compounds by the partial substitution of cations at A and B sites, which can be obtained with the formula ($A_{1-x}A^*_xB_{1-y}B^*_yO_{3-\delta}$). This substitution can improve the ionic and/or the electronic conductivity of the perovskite [6]. The perovskite structure is also affected by the relative oxidation states of the A and B site cations as shown in (**table 1. 1)**.

Table 1. 1: The relative oxidation state (ROS) of A and B cations in the perovskite and some examples.

ROS of A and B cations	Examples
$\boldsymbol{A^{1+}B^{5+}O_3}$	$NaWO_3$
$\boldsymbol{A^{2+}B^{4+}O_3}$	$SrTiO_3$ / $BaFeO_3$
$\boldsymbol{A^{3+}B^{3+}O_3}$	$LaTiO_3$ / $SmFeO_3$

Additionally, the radius of the cation inserted in the A and/or B sites can change the ideal cubic structure to smaller or larger symmetry. This relationship can be described according to the Goldschmidt's tolerance factor, which is an indicator for the stability and the distortion of the crystal structures, **equation (1. 1)** [7],

$$t = \frac{r_A + r_O}{\sqrt{2}\,(r_B + r_O)} \qquad (1.\ 1)$$

Where t is the tolerance factor, r_A is the ionic radius of the A-site, r_B is the ionic

radius of the B-site and r_O is the ionic radius of oxygen ion. By calculating the tolerance factor, it is possible to determine the stability of the perovskite structure. The perovskite having *t* values in the range 0.75 to 1.0 shows that the perovskite structure is stable. For t values less than 0.75, the distorted perovskite is unstable and A ion needs a smaller site while with values above than 1, B ion requires a smaller site. Moreover, the ideal cubic structure of the perovskite exists when *t* is from 0.9 to 1.0. The perovskite structure changes to orthorhombic symmetry as the tolerance factor decreases from 0.9 and to tetragonal or hexagonal shape as it increases beyond the value of 1.0 [7].

1. 2. 3. The Ionic Conduction in Perovskites:

1. 2. 3. 1. *Defects:*

The ionic conduction of a solid material is defined as the transportation of ions through the material. In perovskites, the ions are arranged tightly in the crystalline structure, which makes it difficult to move across the material. However, practically, there are some defects present in the crystalline structures of these materials. These defects include vacancies (Schottky defect), interstitial atoms, vacancy-interstitial pairs (Frenkel defect) and substitutional defects with different-sized atoms [8], as shown in **(figure 1. 2)**.

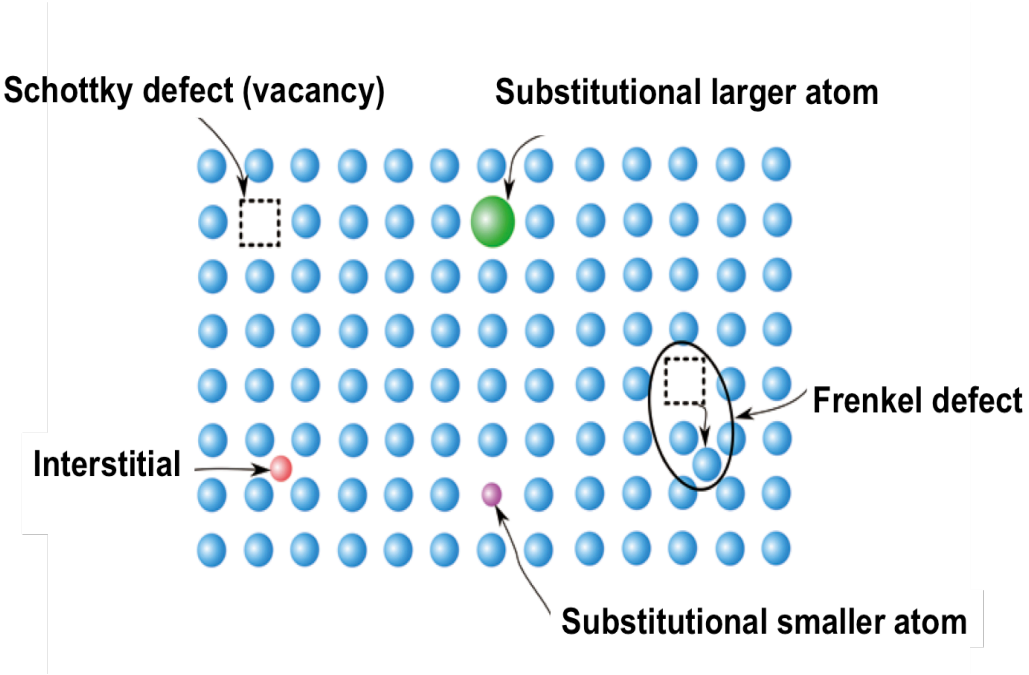

Figure 1. 2: Possible defects in the crystal structure of the perovskite materials, adapted from reference [8].

The Schottky defect (vacancy) can be defined as the elimination of an anion and/or cation that leaves vacant sites within the crystal and the Frenkel defect (vacancy-interstitial pair) is described as an anion or cation moving to an interstitial site. The substitutional defects (extrinsic defects), on the other hand, happen when an atom with different valency is doped into a stoichiometric crystal.

In this work, the first group of perovskites (SLFO) are formed by substitutional defects and the second group is made by both substitutional defects and Schottky defects. The substitutional defects in the first group are created by replacing a specific amount of Sm^{3+} with Li^{+} in $SmFeO_3$ perovskite family. This replacement will enhance the ionic conductivity in this kind of perovskite material because it facilitates the lithium ions transport through the crystal structure, often by a hoping mechanism. In addition to the substitutional defects, in the second group, Schottky defects are used to further improve the ionic conductivity of Li perovskites. This is

done because, now, the lithium ion can jump into a neighbouring cationic vacancy site and then leaves a vacant site behind to allow another lithium ion to accommodate into this unfilled site. Moreover, when the substitutional defect is introduced in the lattice, the charge changes and the material compensates by adjusting the concentration of O^{2-} in the lattice. Therefore, anionic vacancies are also present.

1. 2. 3. 2. *Conductivity Measurements:*

The conductivity measurements for the lithium ionic conductor materials are usually done using electrical impedance spectroscopy (EIS), which gives a frequency-dependent complex resistance. A specific equivalent circuit is used in many studies to measure the lithium ionic conductivity in the ABO_3 perovskite samples. The model of the equivalent circuit is shown in (**figure 1. 3)** and can be written as $\mathbf{R_b(R_{sei}C_{sei})(R_{ct}C_{dl}W)}$. $\mathbf{R_b}$ is the bulk resistance, $\mathbf{R_{sei}}$, $\mathbf{C_{sei}}$ are the resistance and the capacitor of the solid-state interface layer formed (grain boundary), $\mathbf{R_{ct}}$ is the electrolyte/electrode interface resistance, which can be modeled as charge transfer resistance, C_{dl} is the double layer capacitance and **W** is the Warburg impedance at the last sloping data. This **W** is associated with the diffusional effects of lithium ion on the interface between the active material particles and electrolyte. Each (RC) component in the model corresponds to one semicircle in the Nyquist plot [9], **(figure 1. 3)**, where Z' is the real part of the resistance and Z'' is the imaginary part of the resistance.

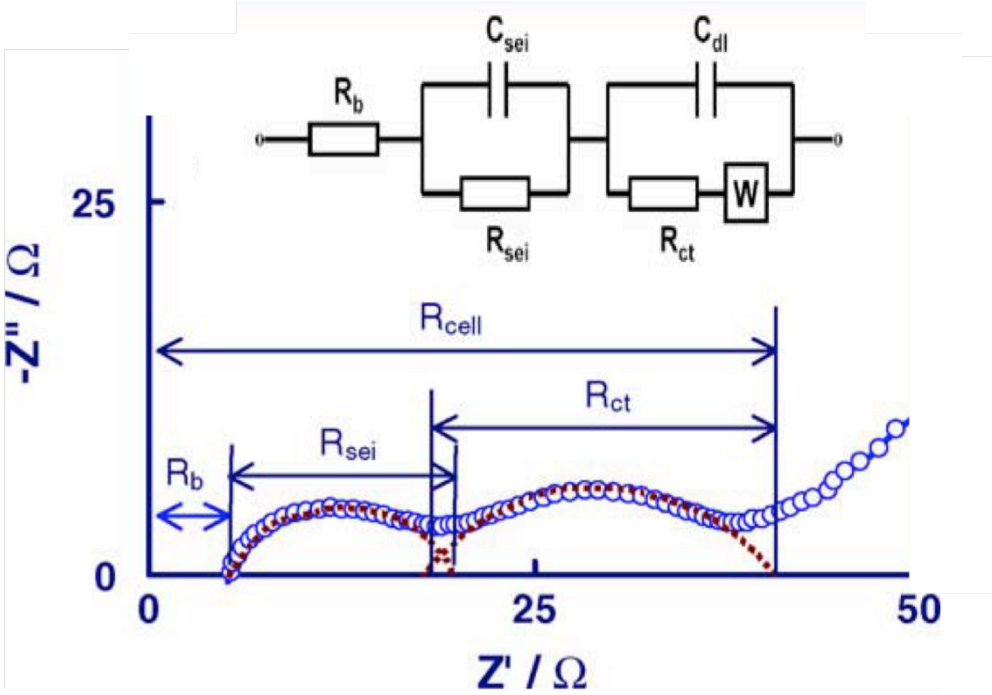

Figure 1. 3 Electrochemical impedance spectroscopy (EIS) for the Li-ion cell and the equivalent circuit used to fit the EIS actual data, adapted from reference [9].

Thus, having two (RC) components in the model of the equivalent circuit explains three different conduction mechanisms in the Li-perovskites. The first mechanism is the bulk crystal conduction determined by the high frequency intercept. The second mechanism (first arc) corresponds to the grain boundary diffusion, at the mid frequency region. The third mechanism (second arc) is the interface between the solid electrolyte and the electrodes at the lower frequency region.

1. 2. 3. 3. *An Example of Li-Perovskites:*

Until now, the Li-perovskite with the highest ionic conductivity is Lithium lanthanum titanate (LLTO). Hence, LLTO is widely studied as a reference perovskite. The first synthesis of LLTO perovskite was carried out by Brous *et al.* [10] in 1953. They replaced the Ca^{2+} ions at the A-sites of the perovskite structure with La^{3+} and Li^{+} ions

($Li_{0.5}La_{0.5}TiO_3$), making this a perovskite with no A-site vacancies, similar to our first group perovskites structure (SLFO). After that, many experimental investigations were carried out to determine the electrical properties of this material. The highest ionic conductivity obtained at room temperature for the bulk crystal of $Li_{0.33}La_{0.557}TiO_3$ perovskite, which is similar to the second group perovskite structure (SLFO*), was 1.0 x 10^{-3} S/cm [11-14]. The high conductivity is likely due to the large amount of equivalent sites in this LLTO perovskite for lithium ions to freely hop from one site to the other.

1. 2. 4. The Use of Perovskites in Lithium-Air Batteries:

ABO_3 perovskite type oxides have been widely found in many different energy storage applications, such as batteries, solid oxide fuel cells, solar cells and electrochemical gas sensors. Specifically, the Li-perovskites synthesised in the present work (SLFO and SLFO*) can be used as a protective layer on the lithium anode or as electrolyte in the lithium air batteries. The different employments of the ABO_3 perovskites in lithium-air batteries are discussed in the following sections.

1. 2. 4. 1. *ABO_3 Perovskite Oxides As Bifunctional Catalysts:*

ABO_3 Perovskite-type oxides are considered as great electrocatalysts for oxidation-reduction reaction (ORR) and/or oxidation-evolution reaction (OER) for many different applications such as catalytic oxidation, sensors, visible-light photocatalysis, and solid oxide fuel cells and metal-air batteries [15-18]. These kinds of perovskites have established great potential for these applications due to their interesting physical-chemical properties, high catalytic activities, cost effectiveness and eco-friendly nature. One example of using ABO_3 perovskite as an efficient ORR

and OER electrocatalyst for lithium air batteries is the work done by Zhang and co-workers [19]. They successfully prepared a 3D ordered macroporous $LaFeO_3$ perovskite by colloidal crystal template method to be used as electrocatalysts. Recently, Meilin Liu and Wei Zhou [20] reported a successful strategy to enhance the ORR and OER electrocatalytic activity of $LaFeO_3$ by introducing A-site cation deficiency (without other modifications) having formula: $La_{1-x}FeO_{3-\delta}$ (where x = 0.02, 0.05 and 0.1). The best bifunctional electrocatalysts synthesised by them for ORR and OER activities in the alkaline solution is L0.95F. These activities are highly efficient and are attributed to the creation of surface oxygen vacancies and the small amount of Fe^{4+} species in the lattice, **Figure (1. 4)** [20].

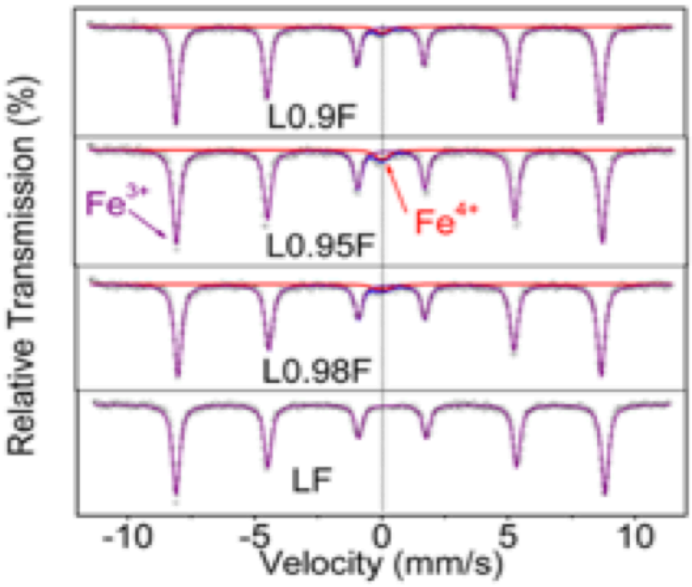

Figure 1. 4: "Room temperature Mössbauer spectra of LF, L0.98F, L0.95F, and L0.9F samples", with permission from reference [20].

1. 2. 4. 2. *ABO_3 Perovskite Oxides As Electrolyte Separator:*

Lithium ionic conducting perovskites have been paid much attention since it was discovered the highest ionic (bulk) conductivity for LLTO, as mentioned previously

[11]. However, it was considered that LLTO is not suitable for solid electrolytes in lithium-air batteries due to their low reduction stability against lithium metal [21]. In addition, it has a low total conductivity value, which is not more than 1×10^{-4} S/cm, due to the high resistance at grain boundaries [21-23]. Therefore, most of the current research is focused on studying LLTO perovskite as an electrolyte separator for rechargeable aqueous-type Li-air batteries. Yoshiyuki Inaguma [24] had successfully prepared LLTO electrolyte ceramics to be used as an electrolyte separator as shown in (**figure 1. 5)**. His LLTO has high total lithium ion conductivity value from 3 to 5×10^{-4} S/cm at 300K. The increment in the total conductivity is due to the high temperature treatment (1450°C) for 6 h, thus, increasing the grain size and reducing the resistance due to grain boundaries, (**figure 1. 6).**

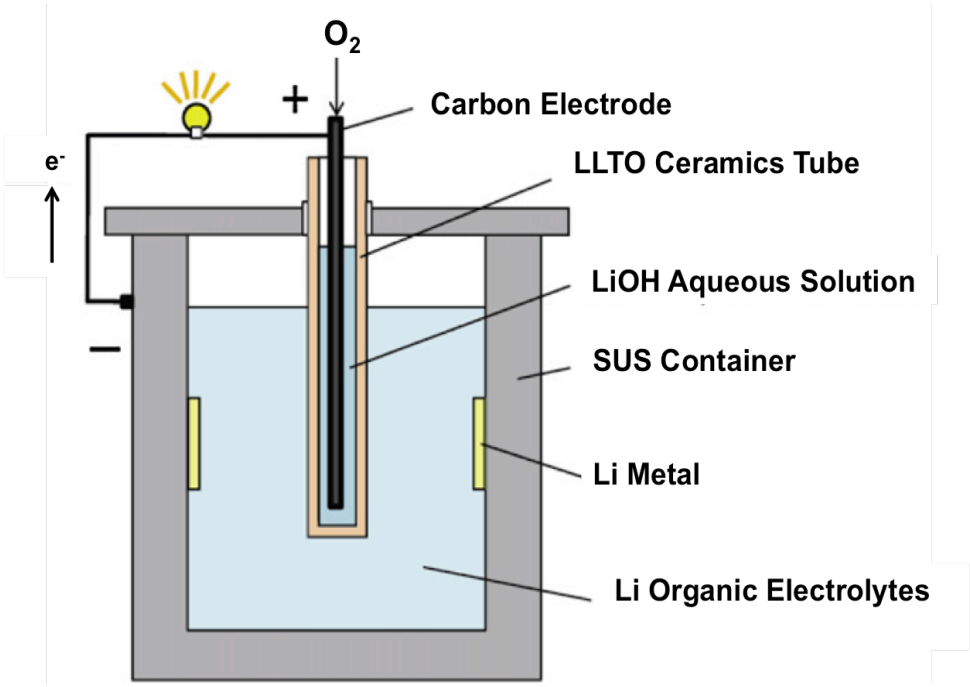

Figure 1. 5: A diagram shows a rechargeable Li-air cell using LLTO perovskite as an electrolyte separator, adapted from reference [24].

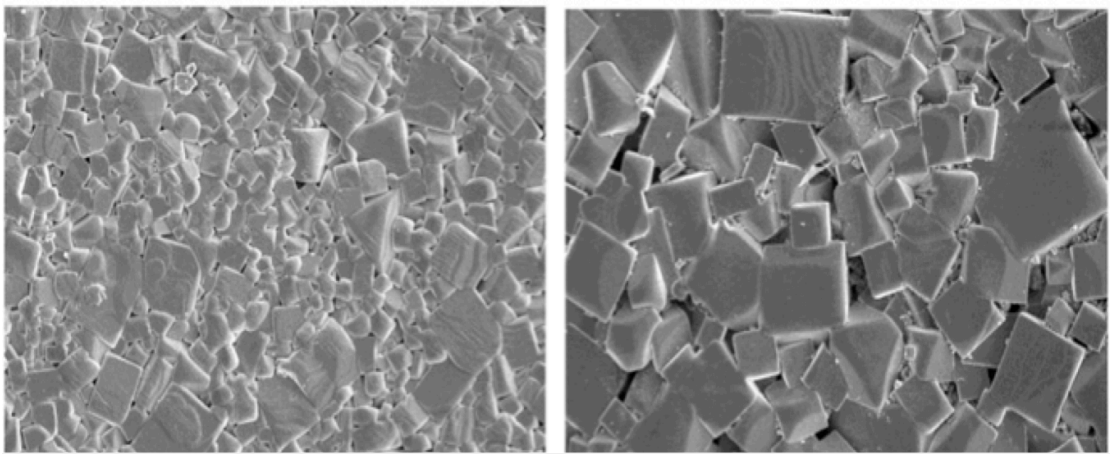

Figure 1. 6: Scanning electron microscopy images for LLTO perovskite sintered at (a) 1400°C and (b) for 6 h, adapted from reference [24].

1. 3. Summary:

A definition and historical background about the ABO_3 perovskite type oxide are addressed at the beginning of this chapter. The crystal structure of this perovskite is provided with the possible relative oxidation states of the A and B site cations. In addition, the ionic conductivity of this perovskite is discussed in terms of having different types of defects in the structure, measuring the ionic conductivity and reporting the highest ionic conductivity published for LLTO as 1×10^{-3} S/cm. Different use of ABO_3 perovskites in lithium air batteries are also provided at the end of this chapter.

1. 4. References:

[1] Tilley, R. J. (2016). Perovskites: structure-property relationships. doi:10.1002/9781118935651

[2] Anderson, M., Greenwood, K., Taylor, G., & Poeppelmeier, K. (1993). B-cation arrangements in double perovskites. Progress in Solid State Chemistry, 22(3), 197-233. doi:10.1016/0079-6786(93)90004-b

[3] Wong, S. S., Zhou, H., & Mao, Y. (2010). Synthesis, Properties, and Applications of Perovskite-Phase Metal Oxide Nanostructures. Material Matters, Retrieved June 30, 2017, from http://www.sigmaaldrich.com/technical-documents/articles/material-matters/synthesis-properties.html

[4] Goodenough, J. B. (2004). Electronic and ionic transport properties and other physical aspects of perovskites. Reports on Progress in Physics, 67(11), 1915-1993. doi:10.1088/0034-4885/67/11/r01

[5] Du, H., Lin, X., Xu, Z., & Chu, D. (2015). Electric double-layer transistors: a review of recent progress. Journal of Materials Science, 50(17), 5641-5673. doi:10.1007/s10853-015-9121-y

[6] Peña, M. A., & Fierro, J. L. (2001). Chemical Structures and Performance of Perovskite Oxides. Chemical Reviews, 101(7), 1981-2018. doi:10.1021/cr980129f

[7] Goldschmidt, V. M. (1926). Die Gesetze der Krystallochemie. Die Naturwissenschaften, 14(21), 477-485. doi:10.1007/bf01507527

[8] Chen, D., Chen, C., Baiyee, Z. M., Shao, Z., & Ciucci, F. (2015). Nonstoichiometric Oxides as Low-Cost and Highly-Efficient Oxygen Reduction/Evolution Catalysts for Low-Temperature Electrochemical Devices. Chemical Reviews, 115(18), 9869-9921. doi:10.1021/acs.chemrev.5b00073

[9] Zhang, S., Xu, K., & Jow, T. (2004). Electrochemical impedance study on the low temperature of Li-ion batteries. Electrochimica Acta, 49(7), 1057-1061. doi:10.1016/j.electacta.2003.10.016

[10] Brous, J., Fankuchen, I., & Banks, E. (1953). Rare earth titanates with a perovskite structure. Acta Crystallographica, 6(1), 67-70. doi:10.1107/s0365110x53000156

[11] Robertson, A., West, A., & Ritchie, A. (1997). Review of crystalline lithium-ion conductors suitable for high temperature battery applications. Solid State Ionics, 104(1-2), 1-11. doi:10.1016/s0167-2738(97)00429-3

[12] Stramare, S., Thangadurai, V., & Weppner, W. (2003). Lithium Lanthanum Titanates: A Review. ChemInform, 34(52). doi:10.1002/chin.200352244

[13] Qian, D., Xu, B., Cho, H., Hatsukade, T., Carroll, K. J., & Meng, Y. S. (2012). Lithium Lanthanum Titanium Oxides: A Fast Ionic Conductive Coating for Lithium-Ion Battery Cathodes. Chemistry of Materials, 24(14), 2744-2751. doi:10.1021/cm300929r

[14] Cao, C., Li, Z., Wang, X., Zhao, X., & Han, W. (2014). Recent Advances in Inorganic Solid Electrolytes for Lithium Batteries. Frontiers in Energy Research, 2. doi:10.3389/fenrg.2014.00025

[15] Wei, Y., Liu, J., Zhao, Z., Chen, Y., Xu, C., Duan, A., He, H. (2011). Highly Active Catalysts of Gold Nanoparticles Supported on Three-Dimensionally Ordered Macroporous LaFeO3for Soot Oxidation. Angewandte Chemie, 123(10), 2374-2377. doi:10.1002/ange.201006014

[16] Natile, M. M., Ponzoni, A., Concina, I., & Glisenti, A. (2014). Chemical Tuning versus Microstructure Features in Solid-State Gas Sensors: LaFe1-xGaxO3, a Case Study. Chemistry of Materials, 26(4), 1505-1513. doi:10.1021/cm4018858

[17] Thirumalairajan, S., Girija, K., Hebalkar, N. Y., Mangalaraj, D., Viswanathan, C., & Ponpandian, N. (2013). Shape evolution of perovskite LaFeO3 nanostructures: a systematic investigation of growth mechanism, properties and morphology dependent photocatalytic activities. RSC Advances, 3(20), 7549. doi:10.1039/c3ra00006k

[18] Maguire, E. (2000). Cathode materials for intermediate temperature SOFCs. Solid State Ionics, 127(3-4), 329-335. doi:10.1016/s0167-2738(99)00286-6

[19] Xu, J., Wang, Z., Xu, D., Meng, F., & Zhang, X. (2014). 3D ordered macroporous LaFeO3 as efficient electrocatalyst for Li–O2 batteries with enhanced rate capability and cyclic performance. Energy & Environmental Science, 7(7), 2213. doi:10.1039/c3ee42934b

[20] Zhu, Y., Zhou, W., Yu, J., Chen, Y., Liu, M., & Shao, Z. (2016). Enhancing Electrocatalytic Activity of Perovskite Oxides by Tuning Cation Deficiency for Oxygen Reduction and Evolution Reactions. Chemistry of Materials, 28(6), 1691-1697. doi:10.1021/acs.chemmater.5b04457

[21] Inaguma, Y., Liquan, C., Itoh, M., Nakamura, T., Uchida, T., Ikuta, H., & Wakihara, M. (1993). High ionic conductivity in lithium lanthanum titanate. Solid State Communications, 86(10), 689-693. doi:10.1016/0038-1098(93)90841-a

[22] Inaguma, Y. (1995). Lithium ion conductivity in the perovskite-type LiTaO3-SrTiO3 solid solution. Solid State Ionics, 79, 91-97. doi:10.1016/0167-2738(95)00036-6

[23] Mei, A., Wang, X., Feng, Y., Zhao, S., Li, G., Geng, H., . . . Nan, C. (2008). Enhanced ionic transport in lithium lanthanum titanium oxide solid state electrolyte by introducing silica. Solid State Ionics, 179(39), 2255-2259. doi:10.1016/j.ssi.2008.08.013

[24] Inaguma, Y., & Nakashima, M. (2013). A rechargeable lithium–air battery using a lithium ion-conducting lanthanum lithium titanate ceramics as an electrolyte separator. Journal of Power Sources, 228, 250-255. doi:10.1016/j.jpowsour.2012.11.098

Chapter 2

Lithium Air Battery

(Introduction and literature review)

2. 1. Introduction:

In the present scenario, around 85% of the world's energy needs mostly depend on the non-renewable fuels such as coal, oil and natural gas, despite the fact that they are unsustainable, depleting rapidly and are the primary contributors to global climate change. This is because these fuels release large amounts of CO_2 to the atmosphere. Modern society is increasingly switching from fossil fuels to a clean energy based economy to reduce their negative impact to the environment. Renewable energy resources such as wind and solar energy have efficiently emerged as the clean energy alternatives. However, these energy sources are limited by several challenges, most significantly the intermittent power supply. A satisfactory solution to protect the device from the intermittent renewable energy supply is to integrate the electrochemical energy storage to the conversion systems. Such storage systems when used in automobile will help to reduce the need of total primary energy source, which is petroleum, by 34% [1, 2].

Electrochemical energy storage and conversion devices, most prominently lithium-ion batteries, super-capacitors, low-temperature fuel cells (LTFCs), and metal-air batteries are intensely studied regarding to their enhanced energy storing ability and long-lasting stability. Most of these studies are focused on cost effectiveness and long–term stabilities to make this technology commercially viable. In this chapter, the primary emphasis is on one of the most feasible energy conserving metal-air batteries, which is the non-aqueous rechargeable lithium- air battery [1].

The rechargeable Li-air battery is an electrochemical energy conversion system based on the electrochemical reaction between the Lithium metal and easily accessible oxygen molecules from the environment. This kind of battery is very attractive to many research groups due to the highly reactive lithium metal at the anode with oxygen at the cathode. This reaction generates an enormous amount of energy density with extended life cycles of the battery. Additionally, it is considered as a promising rechargeable cell for high power applications such as electrical vehicles (EVs). This is due to its high potential energy density, which varies from 1000 to 2000 Wh/kg, **figure (2. 1)**, depending on the type of electrolyte, membrane, cathode design and materials used. The advanced energy storage capability and the electrochemical technology in this battery will soon replace the conventional Li-ion batteries. Further, it will increase the range of the electric vehicles to drive more than 500 miles (per charge), which is similar to the range of the gasoline vehicles [3].

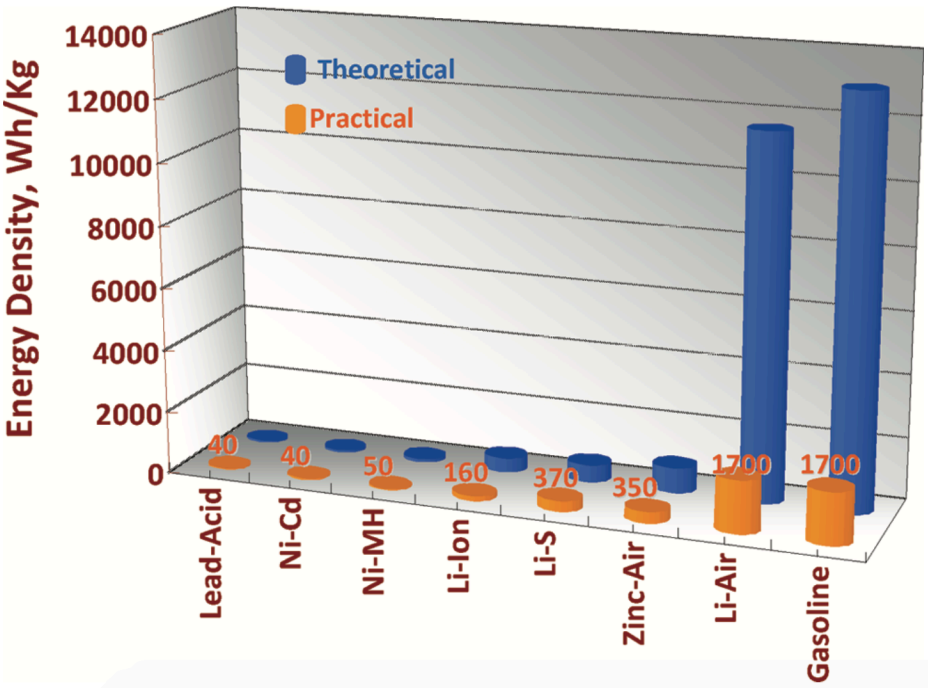

Figure 2. 1: Gravimetric energy densities (Wh/kg) for different types of rechargeable batteries compared to gasoline. Blue bars present the theoretical density, and red bars

show the practically achievable density, with permission from reference [4].

2. 2. Historical Background:

Back in 1979, Blurton and Sammells [5] were the first to review primary metal-air batteries. These batteries have theoretically higher energy densities compared to the ion-based batteries because they use atmospheric oxygen as a cathode reagent. Since then and until the 1990s, not a single practical application was seen for the aqueous Li-air cell chemistry in vehicles, as compared to Zn/air batteries [6]. Conversely, high theoretical gravimetric energy density for Li-air batteries was observed (11,148 Wh k/g) with Li_2O as discharge product.

As an improvement to aqueous Li-air batteries, Abraham and Jiang [7] discovered the first rechargeable non-aqueous lithium-air battery in 1995. They used lithium metal as anode, a gel polymer as the electrolyte, and a carbon substrate for the cathode. Oxygen molecules arrives through the pores of the carbon cathode to serve as the active cathode reagent. Under discharge, the electron reduces the oxygen molecule to its anions, which get stored in the pores of the carbon electrode. The Li-ion conducting gel polymer electrolytes were made from polyacrylonitrile (PAN) and polyvinylidene fluoride (PVdF).

In the following decade, Li-air batteries did not lead to any technically viable products due to some chemical issues, such as dendrites formation at the Li surface, and the formation of unwanted products, that prevented these batteries from achieving higher energy density and longer life cycle. However, a paper published in 2006 by Bruce and co-workers [8] attracted attention to Li-air batteries, especially due to their greater rechargeability. They replaced the polymer electrolyte with an organic electrolyte, propylene carbonate (PC), and used a porous cathode with manganese

dioxide. After that, the Li-air battery regained attention around the world due to its relatively simple structure and huge specific capacity. Moreover, the Li/air technology solves the low-energy-density challenges when used in conjunction to electrochemical storage systems [9,10].

Most of the researchers are developing the advanced catalysts and the cathode substrates to improve efficiency and life cycle of Li-air batteries, especially for organic electrolytes. Porous carbon, graphene and carbon nanotubes (CNT) [11] or carbon nanofibers (CNF) [12] are used as cathode materials whereas metal oxides (MnO_2 [13], Co_3O_4 [14]), noble metals [15, 16], and others [17] are used as catalysts in these batteries.

On the other hand, many researchers study the cycling-stable electrolyte for Li-air batteries in terms of the discharge capacity and the rate capability as they are affected by the electrolyte construction. Also, the performance of the Li-air batteries is investigated based on the influence of the solubility, diffusion coefficients, and partial pressure of O_2 on the electrolyte [18, 19]. At the industrial level, in 2009, IBM and its partners have launched the Battery 500 project to evaluate Li–air batteries for automotive application to ensure a 500-mile driving range per one charge [20]. Certainly, the lithium-air battery becomes a critical investigation area for next-generation energy power, and it could make electric vehicles (EVs) a realistic future vehicle.

2. 3. Types of Lithium-Air Batteries:

The rechargeable lithium-air batteries can be classified according to the electrolyte architecture: (a) aqueous, (b) aprotic (non-aqueous), (c) hybrid and (d) all-solid-state batteries [21], **figure (2. 2)**.

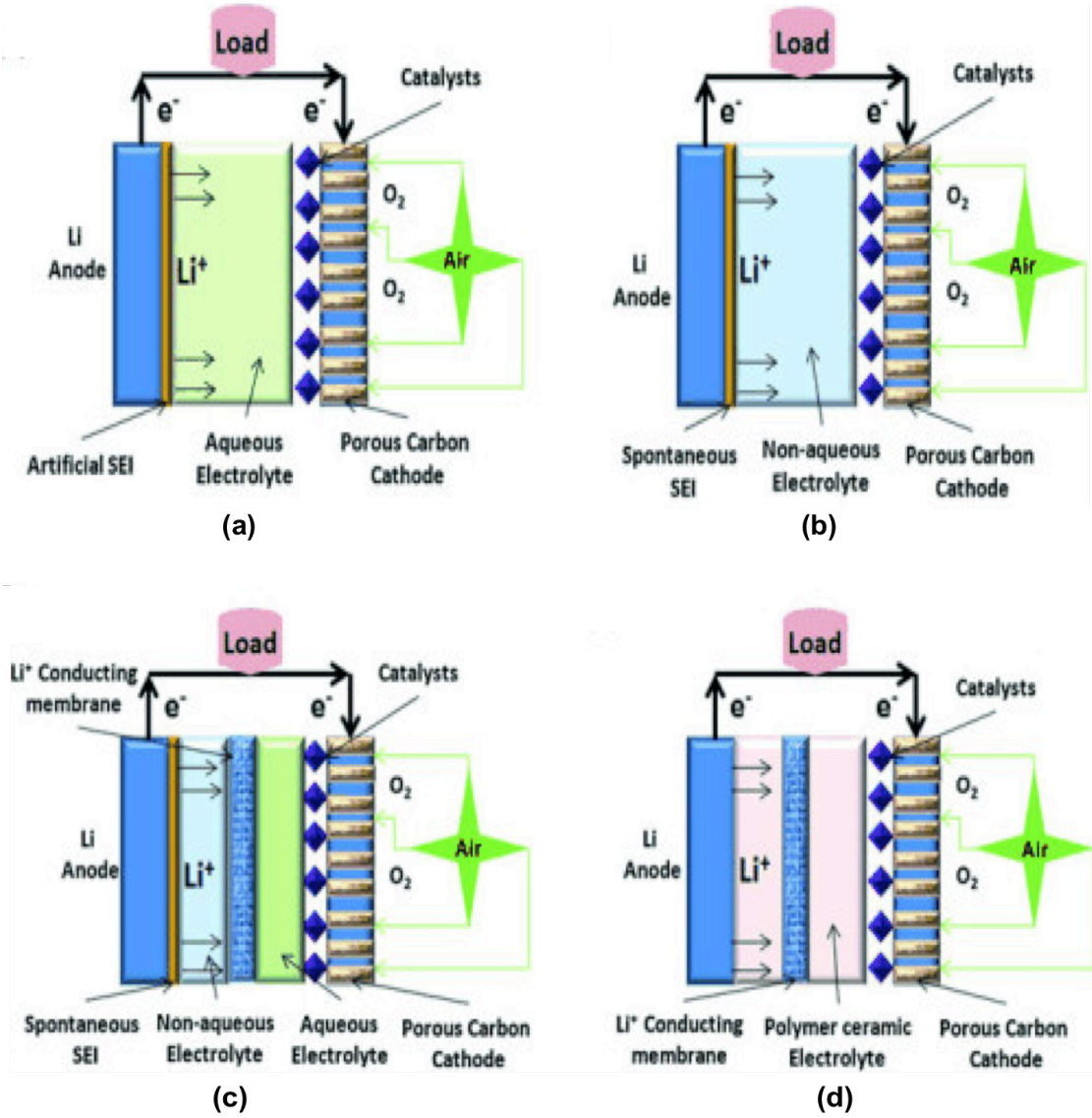

Figure 2. 2: Diagram of the four different designs of Li–air batteries, where (a) is the aqueous battery, (b) is the aprotic (non-aqueous) battery, (c) is the hybrid (mixed aqueous and non-aqueous) battery and (d) is the all-solid-state battery, adapted from reference [21].

The first three design batteries have a liquid electrolyte whereas the all-solid-state battery is designed with a solid electrolyte. Most of the electrolyte systems are

considered as useful systems because they can promote the oxygen reduction reaction (ORR) and the oxygen evolution reaction (OER) during the discharge and charge processes. Also, since water is used as electrolyte for the fast transport of Li^+ in the case of aqueous and hybrid cells, an additional layer must be added to protect the lithium anode from spontaneously reacting. Moreover, the aqueous system has lower theoretical energy density than the non-aqueous system due to the presence of water or acid, which can be involved in the reactions [8]. In addition, the all-solid-state system has not received much attention since the solid-state electrolyte is not sufficiently fast to transfer the lithium ions to the air cathode [22]. As a result of that, the non-aqueous lithium-air battery has attracted considerably more attention because of its potentially high energy density and rechargeability. Currently, many representative research groups are trying to improve the non-aqueous Li–air batteries in terms of the discharge mechanism, electrode materials, electrolyte structure, catalysts, charge–discharge reversibility and cycling ability.

2. 4. The Reaction Mechanism in Li-Air Battery:

The reaction mechanism in a lithium-air battery depends on the rates of redox reactions at the negative electrode and oxygen redox reactions at the positive electrode as follows [3]:

$$xLi \rightarrow xLi^+ + xe^- \qquad \textit{(Anode Side)} \qquad [2.1]$$

$$yO_2 + xe^- \rightarrow yO_2^{-2} \qquad \textit{(Cathode Side)} \qquad [2.2]$$

$$xLi^+ + yO_2{}^{-2} \rightarrow Li_xO_y \qquad [2.3]$$

The reaction of oxygen molecules with lithium metal can theoretically form

three types of products, which are lithium oxide, lithium superoxide and lithium peroxide as shown from equations [2.4] to [2.6] [23, 24].

Lithium oxide: $2\,Li_{(s)} + \frac{1}{2}\,O_2 \rightarrow Li_2O$ [2.4]

Lithium Superoxide: $2\,Li_{(s)} + 2\,O_2 \rightarrow 2\,LiO_2$ [2.5]

Lithium peroxide: $2\,Li_{(s)} + O_2 \rightarrow Li_2O_2$ [2.6]

In 2011, Bruce *et al*. identified the reaction products and their intermediates using the spectroscopic methods [25]. His proposed mechanism aimed to define the chemical reactions at the cathode during the charge and discharge processes and can be summarized below:

- The discharge course:

[1] Oxygen molecule is reduced with the presence of electron to its anion,

$$O_2 + e^- \rightarrow O_2^- \quad [2.7]$$

[2] The oxygen anion reacts with the Lithium cation to produce unstable and disproportionate lithium superoxide on the electrode surface,

$$O_2^- + Li^+ \rightarrow LiO_2 \quad [2.8]$$

[3] The presence of two molecules of lithium superoxide on the cathode surface promotes these molecules to bind together and generate a stable lithium peroxide and oxygen gas,

$$2\,LiO_2 \rightarrow Li_2O_2 + O_2 \quad [2.9]$$

- The charge course:

[1] Lithium peroxide can be directly dissociated into lithium ions and oxygen gas [3],

$$Li_2O_2 \rightarrow 2\,Li^+ + O_2 + 2\,e^- \quad [2.10]$$

As seen from the above reactions, the discharge path has different reaction

steps to get Li_2O_2, while the charge path can be done in one reaction step to evolve O_2 and Li^+. Later, Peng *et al*. in 2012 [26], proposed lithium superoxide as an intermediate in his work. He suggested that lithium superoxide is not stable in presence of lithium ion and thus it is reduced electrochemically into Li_2O_2 as the following equation [23, 26].

$$LiO_2{}^* + Li^+ + e^- \rightarrow Li_2O_2 \qquad [2.11]$$

2. 5. Current Limitations for Li-Air Batteries:

The lithium-air battery is one of the most attractive technologies, especially for long-range electric vehicles (EV), due to their high theoretical specific energy. The Li-air battery consists of a lithium metal anode, a non-aqueous or aqueous electrolyte and an air cathode. In the discharge course, lithium is oxidized into Li^+ and e^- at the anode and then Li^+ ions travel through the electrolyte towards the cathode while e^- flow through an external circuit to react with Li^+ and O_2 at the cathode side to create Li_2O_2. While in the charging process, lithium peroxide is dissociated directly into lithium ions and oxygen gas, as previously discussed. However, there are some challenges that hinder these reactions to occur in the lithium air batteries. These challenges are described below and corrective measures proposed:

- Lithium is a highly reactive metal, in particular with any oxygen or water-containing environment that may cause unwanted products such as LiOH and Li_2CO_3 and the dendrite formation on the lithium metal surface. As a result, lithium anodes need a protective layer to limit the harmful effects of environment on lithium and prevent dendrite growth. Besides, this layer has to be a Li^+ conducting material to allow fast and efficient lithium ion transport through the electrolyte at high current densities [27].

- The air electrode has to be porous to allow the fast diffusion of oxygen from the air into the reaction sites. Also, it needs to have a membrane to avoid the unwanted parasitic reaction with the air components such as H_2O, CO_2, CO and N_2, which limit the lifetime of the lithium air batteries. Additionally, it requires electrocatalysts to improve the ORR performance for the cathode and then improve overall rate of charge/discharge processes for lithium air battery [27].
- The nature of the electrolyte is an important factor that affects the cycling performance of the Li-air batteries. For example, the discharge products (Li_2O_2 and LiO_2) in the non-aqueous system are insoluble, which can block the reaction sites on the cathode surface and then prevent the future reactions, as shown in **figure (2. 3)** [4]. Thus, the electrolyte should have an effective catalyst to reduce the overall potential of the discharge-charge reaction to enhance the power density in the discharge reaction, the electrical efficiency in the discharge-charge cycle and the life-time of the battery.

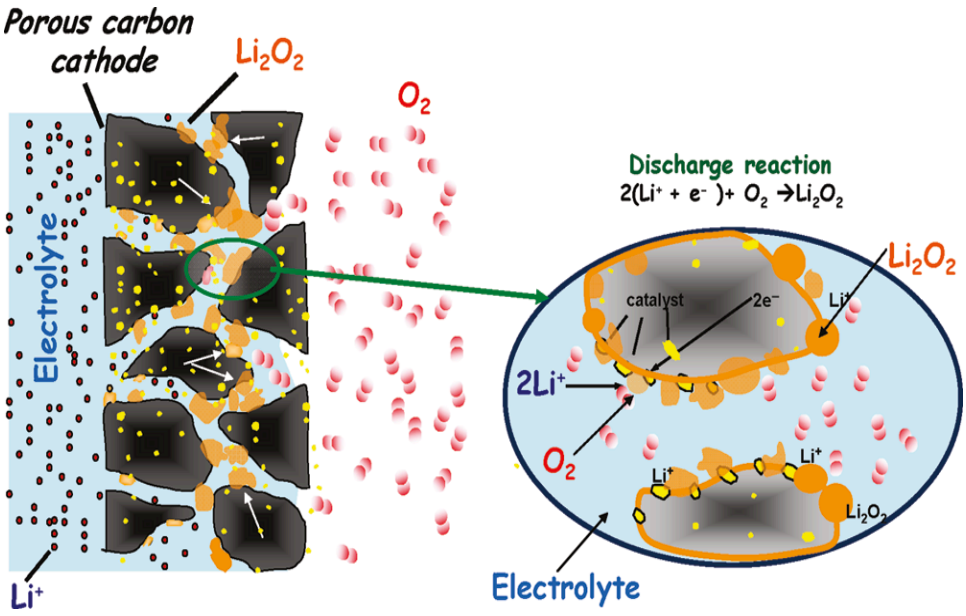

Figure 2. 3: Diagram picture of the air cathode and proposed chemistry at the air

cathode. The left side of the diagram presents the electrolyte (with Li^+ ions), the porous carbon cathode flooded with the electrolyte, catalyst particles, and the product Li_2O_2.while the right side shows the reaction products of Li_2O_2 deposited at the porous carbon cathode, with permission from reference [4].

2. 6. Literature Review:

2. 6. 1. Anode (Lithium Electrode):

The anode side of the lithium air battery contains metallic lithium, which oxidizes to lithium ions during the discharge process. However, the stability loss for the long-term operation of this electrode is one of the most challenging issues. The Li metal at the anode reacts with the ambient atmosphere to form lithium hydroxide (LiOH) and lithium carbonate (Li_2CO_3) [28]. Also, lithium metal in the organic electrolytes faces another problem with dendrites formation after many charge-discharge cycles. The growth of dendrites can create short-circuits between the cathode and the anode due to the prolonged deposition/dissolution of lithium in the electrolyte [29]. Furthermore, the diffusion of lithium ions can be limited due to the electrolyte incompatibility resulting in the formation of a resistive film barrier onto the anode [30]. As a result, life cycle and safety of rechargeable Li-air technology are decreased due to the use of lithium metal as an anode electrode.

A good solution to prevent the lithium electrode from contacting the liquid electrolyte is by its separation from the electrolyte by an interfacial or protective layer made of polymer, ceramics, or glasses. This layer is coated on the lithium metal and provides conductivity for the lithium ions [31]. For example, Aleshin *et al*. [32] coated the lithium metal anode with a protective ceramic layer composed of lithium-aluminum-germanium-phosphorus (LAGP) glass-ceramics. This helped to prevent

anode degradation and further stabilized the Li/air battery performance. However, the cell performance was only examined for ten cycles, making it hard to evaluate the long-term effect of such a ceramic protective layer. Another measure to prevent moisture and electrolyte decomposition products in the cathode was addressed by Crowther *et al*. [33]. They developed a silicone rubber oxygen-selective membrane to increase the oxygen permeation, cover the external cathode surface from reacting with the moisture in the atmosphere and prevent the solvent loss from the cell to the air. Recently, Kim's group [34] succeeded to improve the cycling performance of the lithium-air battery by using a protective layer comprising a conductive polymer and aluminum fluoride particles (AlF_3) on lithium metal. They were able to stabilize the lithium electrode and get better performance by reducing the reductive decomposition of the liquid electrolyte and preventing the growth of lithium dendrites, **figure (2. 4)**.

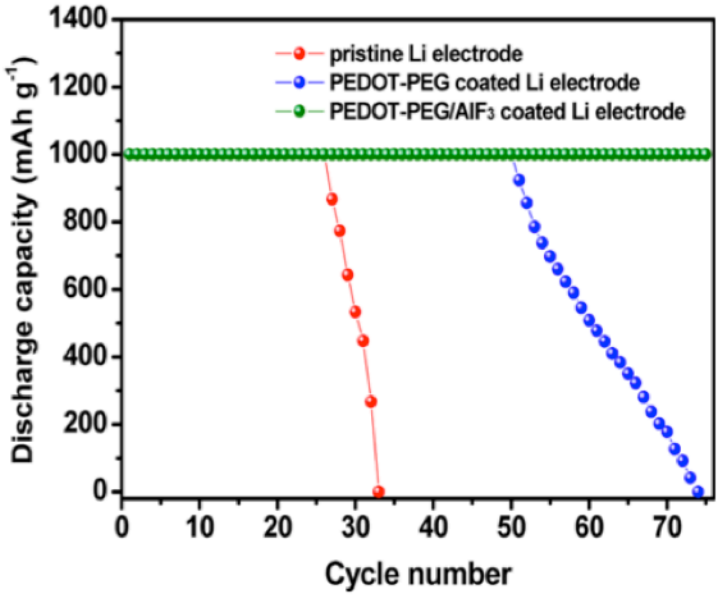

Figure 2. 4: The cycle performance of the Li-O_2 cells with pristine Li electrode (Red), PEDOT-PEG coated Li electrode (Blue) and PEDOT-PEG/AlF_3 coated Li electrode (Green) at a limited capacity of 1000 mAh/g, with permission from reference [34].

Moreover, Hassoun *et al*. [35] have made a typical type of a "Li-air battery" structure by replacing the lithium metal with a lithiated silicon-carbon composite, Li_xSi-C. Nonetheless, their battery is no longer being used because it decays after operating reversibly at a capacity of 1000 mAh/g for about 15 cycles as a result of the oxygen crossover at the cathode side, **figure (2. 5)**.

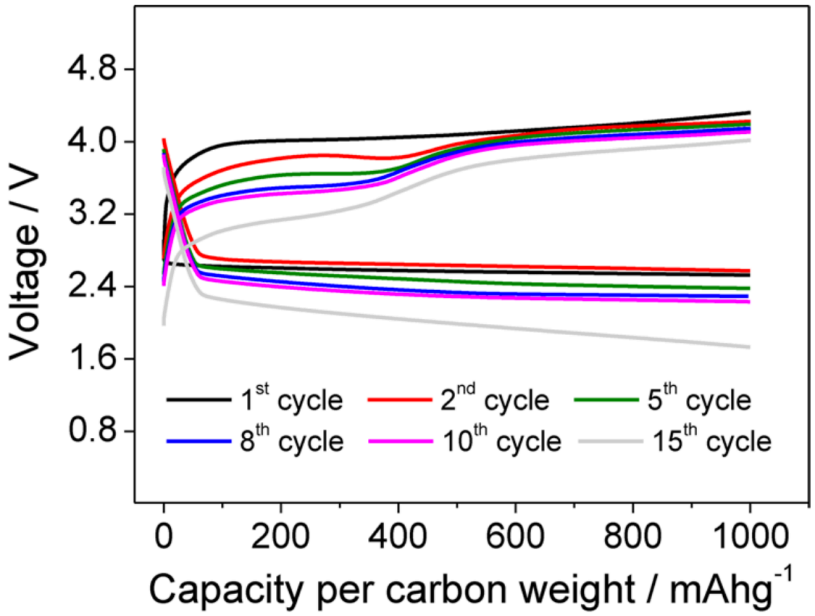

Figure 2. 5: Voltage profiles for cycle number 1, 2, 5, 8, 10 and 15 of a lithiated-silicon/carbon-oxygen cell (Li_xSi/O_2) carried out at a 1000 mAh/g of carbon, with permission from reference [35].

Lithium metal at the anode is one of the most important factors that affects the energy density of Li-air batteries. However, most of the studies are focused on the performance of the cathode and the electrolyte since they influence the discharge-charge potential and the battery capacity [14, 36] significantly.

2. 6. 2. Electrolyte:

In the lithium air battery, the capacity can be defined as the ability of the electrolyte to transport the lithium ions from the lithium anode to the air cathode. During the last ten years, the electrolyte has not been receiving much attention because most of the researchers have been occupied on the development of novel catalysts and cathode materials for this kind of batteries. However, it has been seen that the electrolyte highly affects the efficiency of lithium-air battery [2, 3]. For instance, its performance is influenced by the essential properties of the electrolyte such as viscosity, volatility, ionic conductivity and reactants and products solubility [18, 37-39]. Moreover, the amount of electrolyte (liquid) plays an important role in the void space of the porous carbon network at the cathode side when it is filled with the electrolyte through the discharge process. Xu *et al*. [40] have demonstrated maximum amount of the discharge capacity as a function of the liquid electrolyte. The specific discharge capacity for their coin cell is higher than 160 mAh g/c with about 125 mL of 1.0 M LiTFSI in propylene carbonate PC: EC (1:1 by wt).

The two forms of electrolytes used in Li-air batteries can be more specifically classified into non-aqueous and aqueous electrolytes. Although the oxygen reduction reaction (ORR) is the same for both systems in the discharge course, the electrochemical reactions of non-aqueous and aqueous electrolytes show different behaviors inside the porous cathode material. For example, in the non-aqueous cells, the products of the ORR can fill the open pores on the cathode surface since they are insoluble in the electrolyte. This blocks the reaction sites on the cathode surface and hence prevents the oxygen diffusion through the pores. As a result, the actual specific capacity of the Li-air batteries is found to be less than the theoretical value.

Zhang and Foster [41] have proposed two models of the catalytic ORR regions

in both non-aqueous and aqueous system, as shown in **figure (2. 6)**. The aqueous system can be described as a "three-phase reaction zone", **figure (2. 6. a)**, namely liquid (electrolyte), solid (catalyst/carbon) and gas phase (oxygen). While in the non-aqueous system, the discharge process can be presented as a "two-phase reaction zone", **figure (2. 6. b),** namely liquid (electrolyte) and solid (carbon/catalyst). The aqueous electrolyte shows the formation of soluble discharge products resulting in no pore blocking. The non-aqueous electrolyte shows insoluble discharge products, which can prevent the oxygen diffusion to the surfaces of carbon. Consequently, the oxygen reduction reaction cannot be continuous as indicated in the "three-phase reaction zone" model.

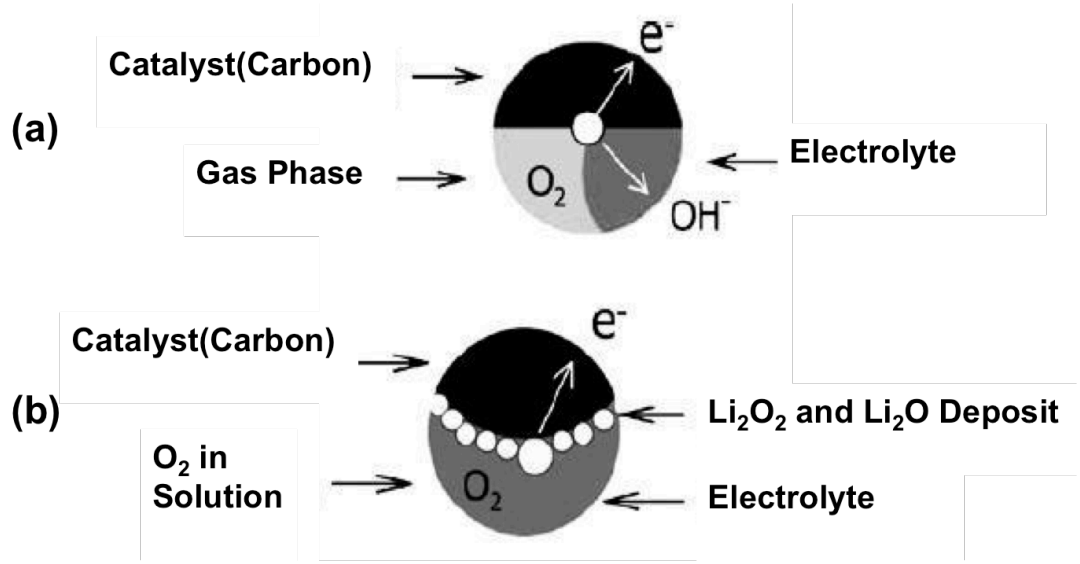

Figure 2. 6: A diagram representation for two Models of the reaction zones for catalytic ORR. (a) The model for aqueous electrolyte-based cell with "three phase reaction zone" and (b) The model for Non-aqueous electrolyte-based cell with "two phase reaction zone, adapted from reference [41].

Comparing the benefits and the drawbacks of both systems, the pore blocking that occurs due to the existence of the insoluble products during the discharge course in the non-aqueous electrolyte is not observed in the aqueous electrolyte. However, the cell fabrication in the aqueous electrolyte is actually difficult because a protective layer is needed on the Li anode to prevent its surface from water corrosion. In addition, aqueous cells demonstrate a lower specific capacity and a poorer rechargeability than non-aqueous cells. In the following section, non-aqueous and aqueous Li-air batteries are reviewed.

2. 6. 2. 1. *Non-aqueous Electrolytes:*

Non-aqueous electrolytes have been extensively studied and developed in the last two decades, and effectively employed in the contemporary and commercial Li-ion batteries. However, they cannot be directly applied to Li-air batteries because they are still facing some challenges. Although there are many publications on Li-air batteries every year, the best non-aqueous electrolyte for these batteries has not been found yet. Based on these studies, an ideal non-aqueous electrolyte for Li-air batteries should have the following properties: high Li^+ conductivity, high chemical-electrochemical stability, especially in the presence of oxygen radicals and Li_2O_2, low vapor pressure or no volatility to get long-term operation, high oxygen solubility and diffusivity and possible solubility of Li_2O_2. The first two features are the basics for non-aqueous electrolytes for their use in Li-air batteries, and the last two features are not crucial, however, they help to improve the battery performance. The non-aqueous electrolyte can be classified into three types called organic liquid carbonates and other solvents, hydrophobic ionic liquids, and polymer (gel) electrolytes. The organic carbonate-based electrolytes are widely used in the conventional Li-ion batteries because of their

low volatility, good Li compatibility, high ionic conductivity and oxidation stability with respect to the Li/Li^+ couple. In Li/air batteries, these electrolytes are tested for different composition of propylene carbonate (PC) and co-solvents like ethylene carbonate, ethers or glymes, to check the decrease in solution viscosity and the increase in oxygen solubility, ionic conductivity and polarity [40,42]. Xu *et al.* [38] examined the effect of using different salts and solvent mixtures to investigate the impact of salt and solvent compositions on the cell performances. They found that the nature of the salt could change the discharge capacity and energy density in the lithium-air battery. For example, the cells with (LiTFSI) showed higher O_2 solubility (5.68 mg/L) and lower viscosity (7.10 mPa.s) than both ($LiPF_6$) and ($LiClO_4$) salts in a propylene carbonate/ethylene carbonate PC/EC mixture electrolyte, **table (2. 1)** [38]. Additionally, using this electrolyte with the Li-air cells exhibited a much greater discharge capacity equal to 167.5 mAh/g of carbon, than using ether-based or glyme-based electrolytes. Since the ethers and glymes-based electrolytes have higher accessibility to the porous carbon structure that leads to block the oxygen pathways. However, all these carbonate-based electrolytes could not be used in lithium-air batteries because of the solvent degradation that occurs due to the formation of the intermediate superoxide during the discharge course. This leads to the unfavorable products like H_2O, CO_2, and Li_2CO_3 at the porous cathode [43-45].

Table 2. 1: Physical properties of the electrolyte of 1.0 M different lithium salts in PC/EC (1:1 wt) and their discharge performances in Li/air coin cells at room temperature.

	Electrolyte properties		Cell Discharge Performance	
Lithium Salt	**O_2 Solubility (mg/L)**	**Viscosity (mPa.s)**	**Discharge time (h)**	**Specific capacity (mAh/g carbon)**
$LiPF_6$	5.19	7.41	77.0	156.8
LiTFSI	5.68	7.10	82.2	167.5
$LiClO_4$	5.22	7.17	88.1	179.3

Further, another stable electrolyte is required for genuinely rechargeable Li-air batteries in order to eliminate the electrolyte degradation effects on carbonate solvent. Ether-based electrolytes have been used for Li-air batteries instead of carbonate-based electrolytes because of their good stability, excellent rate capacity high oxygen solubility and low viscosity [46]. In 2006, Read [19] first employed an ether-based electrolyte with different salts in a non-aqueous Li-air battery, and he confirmed that viscosity is the key factor to control the maximum cell capacity when the oxygen solubility reaches a certain level. Another research on ether-based electrolytes using crown ethers as an addition to the electrolytes has been done by Xu *et al* [47]. Their electrolytes have the capability to coordinate with lithium ions and thus increase their ionic conductivity. Bryantesev *et al.* [48] calculated the stability for a range of organic solvents against the O^{2-} radical by using density functional theory. Their computations show that ether-based electrolytes are more suitable than carbonate-based ones. However, a recent study by Freunberger *et al.* [49] investigated an adverse impact of using ether-based electrolytes during the operation process, which is the electrolyte decomposition. The formation of Li_2O_2 occurs in the first discharge for the Li-air cell

using ether-based electrolytes, however, it disappears in the following cycles. The electrolyte then decomposes to produce a mixture of Li_2CO_3, HCO_2Li, CH_3CO_2Li, polyethers/esters, CO_2 and H_2O. As a result, ether-based solvents may not be suitable as an electrolyte for the Li-air batteries. Thus, finding alternative electrolytes for these batteries is one of the most important challenges for the construction of a good lithium-air battery.

The second class of the non-aqueous electrolyte used for lithium-air batteries is hydrophobic ionic liquids (ILs). The advantage of using this kind of electrolytes in the lithium-air batteries is because they cause no vapor pressure and reduce the compatibility problems with the Li anode. Kuboki *et al*. [50] were the first group to study the discharge behaviors of the air electrode by using an ionic liquid composed of 1-ethyl-3methyl1imidazolinium bis (trifluoromethanesulfonimide) (EMITFSI) Tetrafluoroborate. After 56 days of testing, the cell showed a high discharge capacity equals to 5360 mAh/g at a very low current density of 0.01 mA/cm in 60% humidity. Using this compound prevents electrolyte evaporation and hydrolysis of the anode electrode. Another study by Giorgio *et al* [51] was done in 2011. They have employed different component systems such as pyrrolidinium (PYR14-TFSI), ether pyrrolidinium (PYR12O1-FAP), and (EMITFSI) to determine the effect of the ionic liquid electrolyte on the ORR. They found that the presence of lithium salt could affect both the ORR and OER. For example, Abraham *et al*. [52] have demonstrated that Li_2O and Li_2O_2 are highly rechargeable for ORR after several cycles without electrode passivation by using (EMITFS) ionic liquid electrolyte. In addition, Zhang *et al*. [53] have synthesized a propyl imidazolinium-TFSI-silica-PVdF-HFP gel to be used as a Li-air electrolyte. The advantage of using this material with a polymer is to reduce the anode corrosion due to moisture by stabilizing the anode/electrolyte

interface. As a result, there is an increase in the discharge capacity to 2800 mAh/g, which is higher than the discharge capacity of a pure ionic liquid system (1500 mAh/g), **figure (2. 7)**. Thus, the hydrophobic ILs can be considered as worthy candidates for building long-term rechargeable Li-air batteries. It is, however, too hard to use them for practical applications, especially with the instability of their interface with the electrodes. Henceforth, researchers show more interest in the all-solid-state Li/air batteries because of their advantages in terms of increased interfacial stability, safety, and longer life cycle.

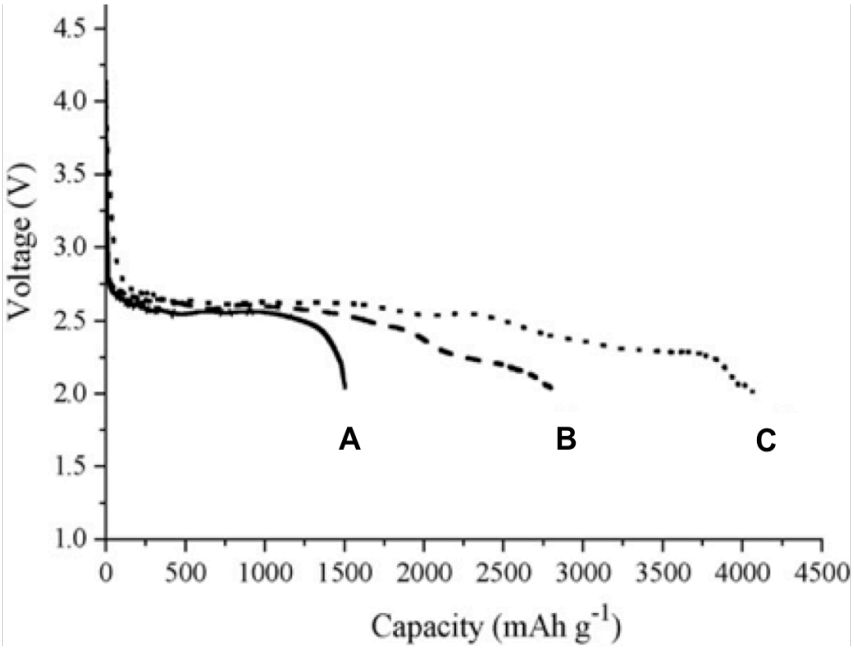

Figure 2. 7: The discharge curves of lithium air cells with different electrolytes in ambient atmosphere at the discharge current density of 0.02 mA cm^{-2}. The electrolytes are (A) LiTFSI-PMMITFSI based non-catalyzed lithium air battery (solid), (B) LiTFSI-PMMITFSI–silica–PVdF-HFP polymer composite electrolyte based non-catalyzed lithium air battery (dash) and (C) LiTFSI-PMMITFSI–silica–PVdF-HFP polymer composite electrolyte based on α-MnO_2 catalyzed lithium air battery (dot), adapted from reference [53].

Several reports have recommended the use of polymer systems and less conventional laminated glass ceramic/polymer ceramic systems [54-56]. In 2011, Hassoun *et al*. [56] studied the oxygen redox reaction in Li-air cells using a polymer based on polyethylene oxide (PEO) electrolyte, which belongs to the class of polymer composite electrolyte (PCE). They found that the lithium and carbon electrodes and the (PCE) electrolyte remain in excellent condition after the discharge-charge processes test, which confirms the protective role of the PEO matrix. Also, their cyclic voltammetry (CV) run at low currents show two peaks related to the discharge formation products of Li_2O_2 and Li_2O and one peak associated to the charge accumulation product of Li^+.

2. 6. 2. 2. ***Aqueous Electrolytes:***

There are different types of non-aqueous electrolytes, although, the aqueous electrolytes are just limited to weak or strong acid or basic solutions. The prime advantage of using this electrolyte is that the discharge products (Li_2O_2 and Li_2O) are soluble in the aqueous solution. In addition, the discharge potentials for the aqueous systems are higher than the non-aqueous counterparts and lie generally between 3.0 to 3.3 V range depending on the pH of the solution. The standard aqueous solution is a mixture of Lithium hydroxide, lithium chloride, and H_2O [57, 58], where the concentration of LiCl and/or its pH can be adjusted, especially when its acidity affects the amount of LiOH during the discharge process. In addition, many other types of aqueous electrolytes are considered such as diluted LiOH, $HCl/LiClO_4$, $HNO_3/LiNO_3$, etc. [59]. The anode in the aqueous electrolyte needs a protective layer with high Li^+ conductivity in order to prevent the lithium metal corrosion. Aono *et al*. were using NASICON-type lithium ion conducting solid electrolyte $Li_{1+x}A_xM_{2-x}(PO_4)_3$ (A = Al,

Sc, Y, M = Ti, Ge) as a protective layer in their experiments [60, 61]. After that, Kumer *et al*. [62] have studied this type of solid lithium conductor and reported the highest conductivity of 4.6×10^{-3} S/cm for glass ceramics of $Li_{1+x}Al_xGe_{2-x}(PO_4)_3$. Moreover, the protective layer should be stable in presence of water. Imanishi *et al*. [63–65] have examined the water stability of $Li_{1+x}Al_xTi_{2x}(PO_4)_3$ (LTAP) and $Li_{1.4}Al_{0.4}Ge_{1.6}(PO_4)_3$ (LAGP). They found that LTAP and LGAP were stable in an aqueous solution saturated with LiOH and LiCl but not in an aqueous solution of 1 M LiOH. However, it is not possible to use one of the LATP and LAGP protective layers without an interface layer such as a thin Li_3N layer, between them and the lithium anode. This is because they will be unstable if they are in direct contact with lithium metal. Stevens and co-workers have performed different experimental studies by applying non-aqueous electrolyte as a protective layer between the lithium anode and LTAP [66-68]. They used an anion exchange membrane and an oxygen evolution electrode as shown in **figure (2. 8. a).** Their cell performance is found to be more than 100 cycles without any degradation at a low current density of 0.1 mA/cm^2 for a short polarization period of 0.2 h at room temperature. The corresponding cell performance for this electrolyte is presented in **figure (2. 8. b)**.

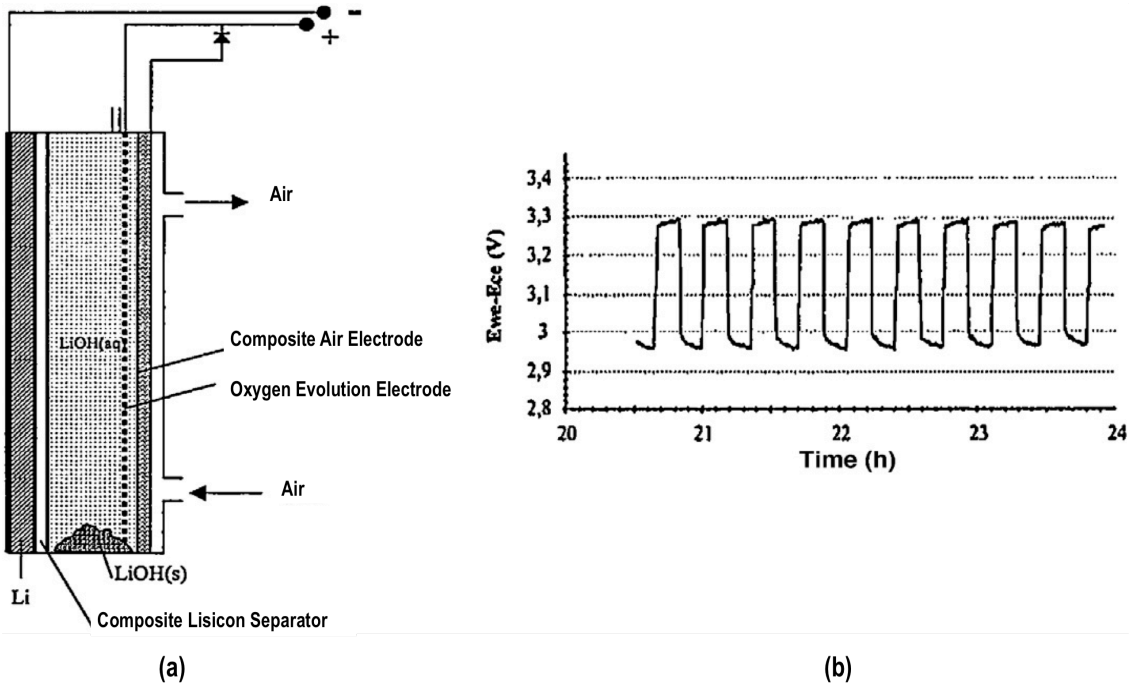

Figure 2. 8: (a) A diagram of the proposed lithium air cell, (b) The cycling performance of the oxygen evolution electrode at a low current density of 0.1 mA/cm^2, adapted from reference [66].

Imanishi and co-workers [69] were studying the cell performance of the aqueous lithium air battery with a limited amount of water. Their battery was designed as Li/$LiClO_4$-EC-DME/LTAP/saturated LiOH and LiCl aqueous solution/carbon black, where the platinum mesh with platinum black was applied as the oxygen evolution electrode. Using one gram of water, the discharge capacity is found to be 300 mAh based on the 30% utility of water, and the energy density was computed from the discharge capacity and open circuit voltage (OCV) of 3.0 V to be 853 Wh/kg. In addition, they have also studied the discharge and charge cell performance using an aqueous solution of acetic acid (HOAc) and lithium acetate (LiAc). Their Li-air cell design (Li/PEO_{18}LiTFSI–10 wt% $BaTiO_3$/LTAP/HAc- H_2O-LiAc/carbon) shows an excellent cyclic performance at current density of 0.5 mA/cm^2

at 60°C. The discharge capacity was high as 225 mAh per 1 gram of HOAc with consumption of 56% HOAc, and the energy density calculated as 779 Wh/kg based on the weight of lithium anode and acetic acid. This lithium-air cell could recollect a discharge-charge capacity of 250 mAh/g for 15 cycles. From these studies, it is possible to say that the discharge capacity of the aqueous lithium–air battery is dependent on the amount of the aqueous electrolyte.

2. 6. 3. Cathode (Air Electrode):

The kind of air electrode (cathode) material in lithium-air batteries is one of the most important elements that affect the overall cell performance. Most of the previous researchers tried to develop the cathode materials to achieve the best of many different characteristics like chemical stability, electrical conductivity, surface area and porosity [3]. The cathode materials should have a stable porous structure to store the discharge products and provide channels for oxygen diffusion into the reaction sites. Many cathode materials have been tested to provide these features for non-aqueous lithium air batteries, more specifically carbon-based materials. Carbon-based materials have been the most attractive materials studied due to their excellent electrical conductivity and large surface areas [70, 71]. They are widely applied as a catalyst support, conductive agents and electrode material for many different applications such as fuel cells, lithium-ion batteries, electrochemical supercapacitors, and recently in lithium-air batteries [1]. Also, it is possible to classify the carbon-based materials into three different groups, which are porous carbon, carbon nanotubes, and graphene.

Porous carbon materials have been widely applied as air electrode for most lithium-air cells due to the high charge transfer for the electrochemical reactions and

the high storage for the discharge products. Moreover, it is possible to achieve higher specific capacity using metallic lithium as an anode material and porous carbon as a cathode material because of the small mass of the porous carbon electrode. These materials show positive catalytic activities toward the ORR as a result of the presence of defect sites on the carbon surface. Various types of carbon have been commercially investigated as cathode materials for non-aqueous Li-air batteries such as activated carbon (AC) [72], Super P [73,74], Vulcan XC-72 [75] and Ketjen black (KB) [76]. Recent works have considered some other new carbon-based materials that show high performance due to their unique structures and the greater number of defects/vacancies. These materials are mesoporous carbon [77], carbon nanofibers [78, 79] and carbon microfibers [80]. In 2011, Mitchell *et al*. [78] were using hollow carbon fibers as a cathode material in the lithium air battery. The benefit of using these materials is due to their non-attachment to the binder because they are directly grown-up on a ceramic porous substrate, as shown in **figure (2. 9)**. The binder materials such as nanocarbon binder were previously used to prevent the undesirable deformation and improve the stability of preform shape. These carbon fiber electrodes established a very high discharge capacity equal to 7200 mAh/g of carbon and energy density of 2500 Wh/kg, which is four-times that of the advanced lithium compounds like $LiCoO_2$ (600 Wh/kg). In addition, the carbon fibers materials are able to give a clear imagining to the Li_2O_2 formation and morphological evolution during discharge process because of their unique structure.

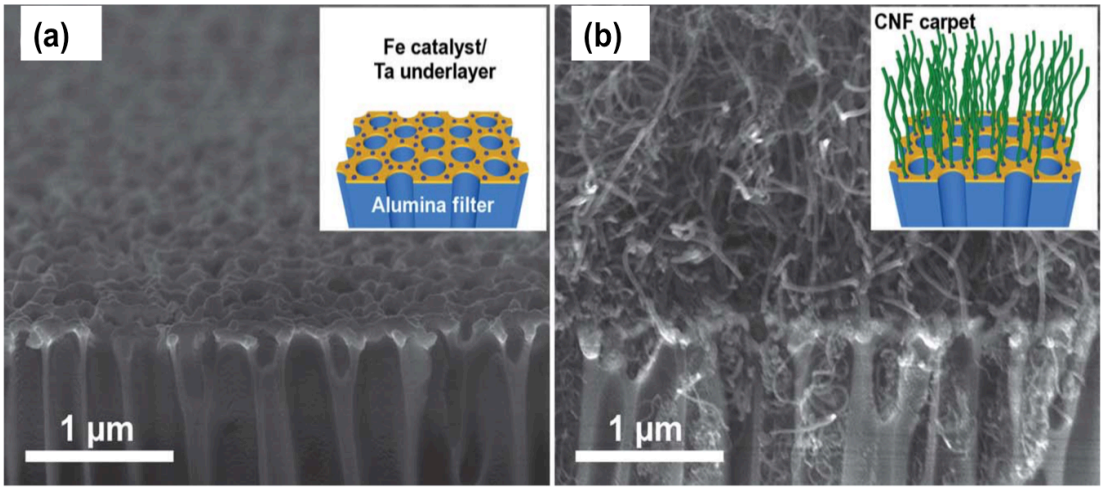

Figure 2. 9: (a) SEM image of the porous anodized aluminum oxide (AAO) filter after thin film deposition using electron beam evaporation and (b) SEM image of the AAO filter after Nano fiber growth, adapted from reference [78].

Carbon nanotube materials (CNTs) are recently used for the non-aqueous lithium-air batteries because of their high chemical and thermal stability, high elasticity, high tensile strength and high conductivity resulting from their structures. In 2013, Shen *et al*. [81] reported that their pure CNTs sponge electrode could exhibit a specific capacity of 6424 mAh/g and discharge voltage of 2.45 V at a current density of 0.05 mA/cm^2. Moreover, in the same year, Li *et al*. [82] applied partly cracked CNTs to the substrate, and found that the capacity of cracked CNTs is almost twice as large as that of non-cracked CNTs (1513 mAh/g vs. 800 mAh/g).

Graphene has attracted considerable attention as a carbon cathode applicant due to the high electron transfer rate, the large surface area (theoretical value 2630 m^2/g), and the high electronic conductivity (10^3 to 10^4 S/m). Hence, it has been widely used in many different applications such as fuel cells [83,84] and Li-ion batteries [85]. Recently, it has been examined as an air electrode material for lithium-air batteries because the oxygen molecule can access both sides of graphene nanosheets

(GNSs) [86]. Li *et al*. [87] applied the GNS material as a cathode electrode in non-aqueous lithium-air batteries. Their cell discharge capacity was higher as 8705.9 mAh/g at a current density of 75 mA/g than the commercial carbon electrode. The high discharge capacity is due to the active sites at the edges of graphene, which is contributed to the superior electrocatalytic activity towards the ORR. Recently, graphene was synthesized directly on the skeleton of porous nickel foam (3D-G electrode) using a chemical vapor deposition (CVD) method to be used in lithium-air batteries [88]. This material was tested at a current density of 0.083 mA/cm^2 to give a discharge capacity equal to 970 mAh/g. However, the highest discharge capacity of a graphene-based cathode was reported in 2011 by Xiao *et al*. [89]. They used a novel hierarchical arrangement of structural and functional graphene sheets to facilitate the diffusion of oxygen into the microporous channels and provide storage for the discharge products of lithium oxides, **figure (2. 10. a)**. The discharge capacity achieved by them is 15,000 mAh/g at a current density of 0.1 mA/cm^2, **figure (2. 10. b)**. In conclusion, it should be noted that different carbon-based materials have various optimum behaviors based on their unique characteristics to be used effectively in Li-air batteries.

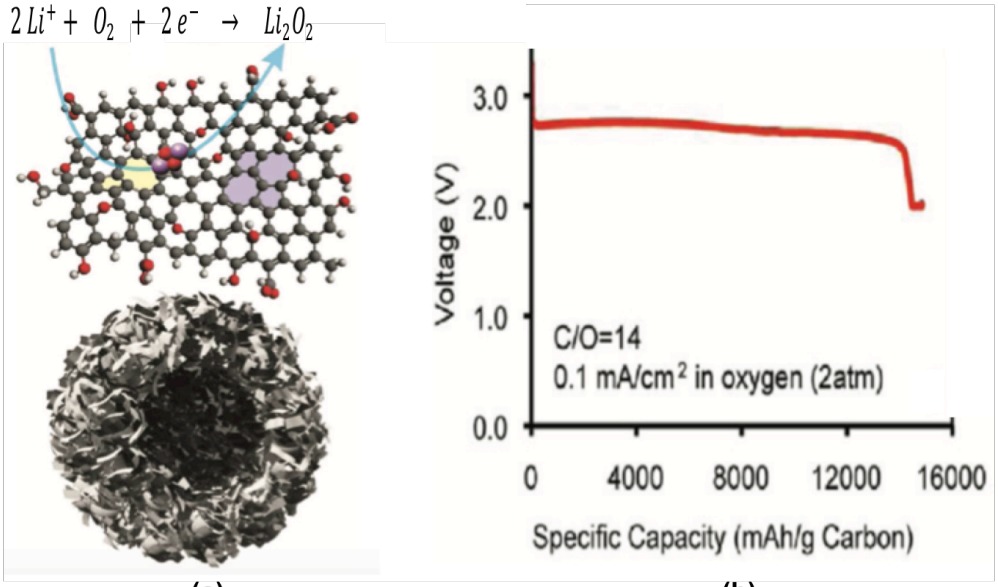

Figure 2. 10: "(a) Schematic structure of a functionalized graphene sheet (upper image) with an ideal bimodal porous structure (lower image) (b) The discharge curve of a Li-O_2 cell using functionalized graphene sheets FGS (C/O = 14) as the air electrode (P_{O2} = 2atm)", adapted from reference [89].

2. 8. Summary:

This chapter gives an introduction and a literature review for lithium-air batteries. The introduction is divided into different sections, which are historical background, types of Li-Air batteries, their general reaction mechanisms, and current limitations. The literature review is organized mainly into three sub sections, which are anode, electrolyte and cathode. Each section provides the most significant studies that have been recently published. These studies are based on the development of lithium-air batteries in terms the used material, the stability, the energy density and its life cycle.

2. 9. References:

[1] Yang, Z., Zhang, J., Kintner-Meyer, M. C., Lu, X., Choi, D., Lemmon, J. P., & Liu, J. (2011). Electrochemical Energy Storage for Green Grid. Chemical Reviews, 111(5), 3577-3613. doi:10.1021/cr100290v

[2] Chen, D., Chen, C., Baiyee, Z. M., Shao, Z., & Ciucci, F. (2015). Nonstoichiometric Oxides as Low-Cost and Highly-Efficient Oxygen Reduction/Evolution Catalysts for Low-Temperature Electrochemical Devices. Chemical Reviews, 115(18), 9869-9921. doi:10.1021/acs. chemrev. 5b00073

[3] Ma, Z., Yuan, X., Li, L., Ma, Z., Wilkinson, D. P., Zhang, L., & Zhang, J. (2015). A review of cathode materials and structures for rechargeable lithium–air batteries. Energy Environ. Sci., 8(8), 2144-2198. doi:10.1039/c5ee00838g.

[4] Girishkumar, G., Mccloskey, B., Luntz, A. C., Swanson, S., & Wilcke, W. (2010). Lithium−Air Battery: Promise and Challenges. The Journal of Physical Chemistry Letters, 1(14), 2193-2203. doi:10.1021/jz1005384

[5] Blurton, K. F., & Sammells, A. F. (1979). Metal/air batteries: Their status and potential — a review. Journal of Power Sources, 4(4), 263-279. doi:10.1016/0378-7753(79)80001-4

[6] Powers, M. J., Sammells, A. F., & Blurton, K. F. (1980). Assessment of air cathodes for metal/air batteries. Journal of Power Sources, 5(4), 348-349. doi:10.1016/0378-7753(80)80039-5

[7] Abraham, K. M. (1996). A Polymer Electrolyte-Based Rechargeable Lithium/Oxygen Battery. Journal of The Electrochemical Society, 143(1), 1. doi:10.1149/1.1836378

[8] Ogasawara, T., Debart, A., Holzapfel, M., Novak, P., & Bruce, P. G. (2006). Rechargeable Li2O2 Electrode for Lithium Batteries. ChemInform, 37(18). doi:10.1002/chin.200618011

[9] Scrosati, B., Hassoun, J., & Sun, Y. (2011). Lithium-ion batteries. A look into the future. Energy & Environmental Science, 4(9), 3287. doi:10.1039/c1ee01388b

[10] Peng, Z., Freunberger, S. A., Hardwick, L. J., Chen, Y., Giordani, V., Bardé, F., Bruce, P. G. (2011). Oxygen Reactions in a Non-Aqueous Li Electrolyte. Angewandte Chemie, 123(28), 6475-6479. doi:10.1002/ange.201100879

[11] Li, Y., Wang, J., Li, X., Liu, J., Geng, D., Yang, J., Sun, X. (2011). Nitrogen-

doped carbon nanotubes as cathode for lithium–air batteries. Electrochemistry Communications, 13(7), 668-672. doi:10.1016/j.elecom.2011.04.004

[12] Zhang, G. Q., Zheng, J. P., Liang, R., Zhang, C., Wang, B., Hendrickson, M., & Plichta, E. J. (2010). Lithium–Air Batteries Using SWNT/CNF Buckypapers as Air Electrodes. Journal of The Electrochemical Society, 157(8), A953-A956. doi:10.1149/1.3446852

[13] Débart, A., Paterson, A., Bao, J., & Bruce, P. (2008). α-MnO_2 Nanowires: A Catalyst for the O_2 Electrode in Rechargeable Lithium Batteries. Angewandte Chemie International Edition, 47(24), 4521-4524. doi:10.1002/anie. 200705648H. Cheng and K. Scott, Journal of Power Sources, 2010, 195, 1370-1374.

[14] Lu, Y., Xu, Z., Gasteiger, H. A., Chen, S., Hamad-Schifferli, K., & Shao-Horn, Y. (2010). Platinum−Gold Nanoparticles: A Highly Active Bifunctional Electrocatalyst for Rechargeable Lithium−Air Batteries. Journal of the American Chemical Society, 132(35), 12170-12171. doi:10.1021/ja1036572

[15] Cheng, H., & Scott, K. (2011). Selection of oxygen reduction catalysts for rechargeable lithium–air batteries—Metal or oxide? Applied Catalysis B: Environmental, 108-109, 140-151. doi:10.1016/j.apcatb.2011.08.021

[16] Zhang, S. S., Ren, X., & Read, J. (2011). Heat-treated metal phthalocyanine complex as an oxygen reduction catalyst for non-aqueous electrolyte Li/air batteries. Electrochimica Acta, 56(12), 4544-4548. doi:10.1016/j. electacta. 2011. 02.072

[17] Ren, X., Zhang, S. S., Tran, D. T., & Read, J. (2011). Oxygen reduction reaction catalyst on lithium/air battery discharge performance. Journal of Materials Chemistry, 21(27), 10118-10125. doi:10.1039/c0jm04170j

[18] Read, J. (2002). Characterization of the Lithium/Oxygen Organic Electrolyte Battery. Journal of The Electrochemical Society, 149(9), A1190-A1195. doi:10.1149/1.1498256

[19] Read, J. (2006). Ether-Based Electrolytes for the Lithium/Oxygen Organic Electrolyte Battery. Journal of The Electrochemical Society, 153(1), A96-A100. doi:10.1149/1.2131827

[20] IBM Research Boosts Battery 500 Project with New Materials Partners. (2012, April 20). Retrieved from https://www-03.ibm.com/press/us/en/pressrelease/37511.wss

[21] Rahman, M. A., Wang, X., & Wen, C. (2013). A review of high energy density lithium–air battery technology. Journal of Applied Electrochemistry, 44(1), 5-22. doi:10.1007/s10800-013-0620-8

[22] Lee, J., Kim, S. T., Cao, R., Choi, N., Liu, M., Lee, K. T., & Cho, J. (2011). Metal-Air Batteries with High Energy Density: Li-Air versus Zn-Air. Advanced Energy Materials, 1(1), 34-50. doi:10.1002/aenm.201000010

[23] Zheng, J. P., Liang, R. Y., Hendrickson, M., & Plichta, E. J. (2008). Theoretical Energy Density of Li–Air Batteries. Journal of The Electrochemical Society, 155(6), A432-A437. doi:10.1149/1.2901961

[24] Laoire, C. O., Mukerjee, S., Abraham, K. M., Plichta, E. J., & Hendrickson, M. A. (2010). Influence of Nonaqueous Solvents on the Electrochemistry of Oxygen in the Rechargeable Lithium−Air Battery. The Journal of Physical Chemistry C, 114(19), 9178-9186. doi:10.1021/jp102019y

[25] Bruce, P. G., Freunberger, S. A., Hardwick, L. J., & Tarascon, J. (2011). Li–O2 and Li–S Batteries with High Energy Storage. Nature Materials, 11(1), 19-29. doi:10.1038/nmat3191

[26] Peng, Z., Freunberger, S. A., Chen, Y., & Bruce, P. G. (2012). A Reversible and Higher-Rate Li-O2 Battery. Science, 337(6094), 563-566. doi:10.1126/science.1223985

[27] Bhatt, M. D., Geaney, H., Nolan, M., & O'dwyer, C. (2014). Key scientific challenges in current rechargeable non-aqueous Li–O2 batteries: experiment and theory. Physical Chemistry Chemical Physics, 16(24), 12093. doi:10.1039/c4cp01309c

[28] Assary, R. S., Lu, J., Du, P., Luo, X., Zhang, X., Ren, Y., Amine, K. (2013). The Effect of Oxygen Crossover on the Anode of a Li-O 2 Battery using an Ether-Based Solvent: Insights from Experimental and Computational Studies. ChemSusChem, 6(1), 51-55. doi:10.1002/cssc.201200810

[29] Wang, D., Zhang, W., Zheng, W., Cui, X., Rojo, T., & Zhang, Q. (2017). Towards High-Safe Lithium Metal Anodes: Suppressing Lithium Dendrites via Tuning Surface Energy. Advanced Science, 4(1), 1600168. doi:10.1002/advs.201600168

[30] Kraytsberg, A., & Ein-Eli, Y. (2011). Review on Li–air batteries—Opportunities, limitations and perspective. Journal of Power Sources, 196(3), 886-893. doi:10.1016/j.jpowsour.2010.09.031

[31] Zhang, T., Imanishi, N., Hasegawa, S., Hirano, A., Xie, J., Takeda, Y., Sammes, N. (2009). Water-Stable Lithium Anode with the Three-Layer Construction for Aqueous Lithium–Air Secondary Batteries. Electrochemical and Solid-State Letters, 12(7), A132-A135. doi:10.1149/1.3125285

[32] Aleshin, G. Y., Semenenko, D. A., & Belova, A. I. (2011). Protected anodes for lithium-air batteries. Solid State Ionics, 184(1), 62-64. http://dx.doi.org/10.1016/j.ssi.2010.09.018

[33] Crowther, O., Meyer, B., Morgan, M., & Salomon, M. (2011). Primary Li-air cell development. Journal of Power Sources, 196(3), 1498-1502. doi:10.1016/j.jpowsour.2010.08.061

[34] Kim, J., Woo, H., Kim, W. K., Ryu, K. H., & Kim, D. (2016). Improved Cycling Performance of Lithium–Oxygen Cells by Use of a Lithium Electrode Protected with Conductive Polymer and Aluminum Fluoride. ACS Applied Materials & Interfaces, 8(47), 32300-32306. doi:10.1021/acsami.6b10419

[35] Hassoun, J., Jung, H., Lee, D., Park, J., Amine, K., Sun, Y., & Scrosati, B. (2012). A Metal-Free, Lithium-Ion Oxygen Battery: A Step Forward to Safety in Lithium-Air Batteries. Nano Letters, 12(11), 5775-5779. doi:10.1021/nl303087j

[36] Thapa, A. K., Hidaka, Y., Hagiwara, H., Ida, S., & Ishihara, T. (2011). Mesoporous β-MnO2 Air Electrode Modified with Pd for Rechargeability in Lithium-Air Battery. Journal of The Electrochemical Society, 158(12). doi:10.1149/2.090112jes

[37] Read, J., Mutolo, K., Ervin, M., Behl, W., Wolfenstine, J., Driedger, A., & Foster, D. (2003). Oxygen Transport Properties of Organic Electrolytes and Performance of Lithium/Oxygen Battery. Journal of The Electrochemical Society, 150(10), A1351-A1356. doi:10.1149/1.1606454

[38] Xu, W., Xiao, J., Zhang, J., Wang, D., & Zhang, J. (2009). Optimization of Nonaqueous Electrolytes for Primary Lithium/Air Batteries Operated in Ambient Environment. Journal of The Electrochemical Society, 156(10), A773-A779. doi:10.1149/1.3168564

[39] Kowalczk, I., Read, J., & Salomon, M. (2007). Li-air batteries: A classic example of limitations owing to solubilities. Pure and Applied Chemistry, 79(5), 851-860. doi:10.1351/pac200779050851

[40] Xu, W., Xiao, J., Wang, D., Zhang, J., & Zhang, J. (2010). Effects of Nonaqueous Electrolytes on the Performance of Lithium/Air Batteries. Journal of

The Electrochemical Society, 157(2), A219-A224. doi:10.1149/1.3269928

[41] Zhang, S. S., Foster, D., & Read, J. (2010). Discharge characteristic of a non-aqueous electrolyte Li/O2 battery. Journal of Power Sources, 195(4), 1235-1240. doi:10.1016/j.jpowsour.2009.08.088

[42] Crowther, O., Keeny, D., Moureau, D. M., Meyer, B., Salomon, M., & Hendrickson, M. (2012). Electrolyte optimization for the primary lithium metal air battery using an oxygen selective membrane. Journal of Power Sources, 202, 347-351. doi:10.1016/j.jpowsour.2011.11.024

[43] Freunberger, S. A., Chen, Y., Peng, Z., Griffin, J. M., Hardwick, L. J., Bardé, F., .Bruce, P. G. (2011). Reactions in the Rechargeable Lithium–O_2 Battery with Alkyl Carbonate Electrolytes. Journal of the American Chemical Society, 133(20), 8040-8047. doi:10.1021/ja2021747

[44] Xu, W., Viswanathan, V. V., Wang, D., Towne, S. A., Xiao, J., Nie, Z., . . . Zhang, J. (2011). Investigation on the charging process of Li2O2-based air electrodes in Li–O2 batteries with organic carbonate electrolytes. Journal of Power Sources, 196(8), 3894-3899. doi:10.1016/j.jpowsour.2010.12.065

[45] Xu, W., Xu, K., Viswanathan, V. V., Towne, S. A., Hardy, J. S., Xiao, J., . . . Zhang, J. (2011). Reaction mechanisms for the limited reversibility of Li–O2 chemistry in organic carbonate electrolytes. Journal of Power Sources, 196(22), 9631-9639. doi:10.1016/j.jpowsour.2011.06.099

[46] Lu, Y., Kwabi, D. G., Yao, K. P., Harding, J. R., Zhou, J., Zuin, L., & Shao-Horn, Y. (2011). The discharge rate capability of rechargeable Li–O_2 batteries. Energy & Environmental Science, 4(8), 2999-3007. doi:10.1039/c1ee01500a

[47] Xu, W., Xiao, J., Wang, D., Zhang, J., & Zhang, J. (2010). Crown Ethers in Nonaqueous Electrolytes for Lithium/Air Batteries. Electrochemical and Solid-State Letters, 13(4). doi:10.1149/1.3305330

[48] Bryantsev, V. S., Giordani, V., Walker, W., Blanco, M., Zecevic, S., Sasaki, K., . . . Chase, G. V. (2011). Predicting Solvent Stability in Aprotic Electrolyte Li–Air Batteries: Nucleophilic Substitution by the Superoxide Anion Radical (O2•–). The Journal of Physical Chemistry A, 115(44), 12399-12409. doi:10.1021/jp2073914

[49] Freunberger, S. A., Chen, Y., Drewett, N. E., Hardwick, L. J., Bardé, F., & Bruce, P. G. (2011). The Lithium-Oxygen Battery with Ether-Based Electrolytes. Angewandte Chemie International Edition, 50(37), 8609-8613.

doi:10.1002/anie.201102357

[50] Kuboki, T., Okuyama, T., Ohsaki, T., & Takami, N. (2005). Lithium-air batteries using hydrophobic room temperature ionic liquid electrolyte. Journal of Power Sources, 146(1-2), 766-769. doi:10.1016/j.jpowsour.2005.03.082

[51] Giorgio, F. D., Soavi, F., & Mastragostino, M. (2011). Effect of lithium ions on oxygen reduction in ionic liquid-based electrolytes. Electrochemistry Communications, 13(10), 1090-1093. doi:10.1016/j.elecom.2011.07.004

[52] Allen, C. J., Mukerjee, S., Plichta, E. J., Hendrickson, M. A., & Abraham, K. M. (2011). Oxygen Electrode Rechargeability in an Ionic Liquid for the Li–Air Battery. The Journal of Physical Chemistry Letters, 2(19), 2420-2424. doi:10.1021/jz201070t

[53] Zhang, D., Li, R., Huang, T., & Yu, A. (2010). Novel composite polymer electrolyte for lithium air batteries. Journal of Power Sources, 195(4), 1202-1206. doi:10.1016/j.jpowsour.2009.08.063

[54] Zhang, J., Xu, W., Li, X., & Liu, W. (2010). Air Dehydration Membranes for Nonaqueous Lithium–Air Batteries. Journal of The Electrochemical Society, 157(8), A940-A946. doi:10.1149/1.3430093

[55] Kumar, J., & Kumar, B. (2009). Development of membranes and a study of their interfaces for rechargeable lithium–air battery. Journal of Power Sources, 194(2), 1113-1119. doi:10.1016/j.jpowsour.2009.06.020

[56] Hassoun, J., Croce, F., Armand, M., & Scrosati, B. (2011). Investigation of the O2 Electrochemistry in a Polymer Electrolyte Solid-State Cell. Angewandte Chemie, 123(13), 3055-3058. doi:10.1002/ange.201006264

[57] Zhang, J., Wang, D., Xu, W., Xiao, J., & Williford, R. (2010). Ambient operation of Li/Air batteries. Journal of Power Sources, 195(13), 4332-4337. doi:10.1016/j.jpowsour.2010.01.022

[58] He, P., Wang, Y., & Zhou, H. (2010). A Li-air fuel cell with recycle aqueous electrolyte for improved stability. Electrochemistry Communications, 12(12), 1686-1689. doi:10.1016/j.elecom.2010.09.025

[59] Zheng, J. P., Andrei, P., Hendrickson, M., & Plichta, E. J. (2011). The Theoretical Energy Densities of Dual-Electrolytes Rechargeable Li-Air and Li-Air Flow Batteries. Journal of The Electrochemical Society, 158(1), A43-A46. doi:10.1149/1.3515330

[60] Aono, H., Sugimoto, E., Sadaoka, Y., Imanaka, N., & Adachi, G. (1989).

ChemInform Abstract: Ionic Conductivity of the Lithium Titanium Phosphate (Li1 xMxTi2-x(PO4)3, M: Al, Sc, Y, and La) Systems. ChemInform, 20(29), 590- 591. doi:10.1002/chin.198929007

[61] Aono, H. (1990). Ionic Conductivity of Solid Electrolytes Based on Lithium Titanium Phosphate. Journal of The Electrochemical Society, 137(4), 1023-1027. doi:10.1149/1.2086597

[62] Thokchom, J. S., & Kumar, B. (2010). The effects of crystallization parameters on the ionic conductivity of a lithium aluminum germanium phosphate glass–ceramic. Journal of Power Sources, 195(9), 2870-2876. doi:10.1016/j.jpowsour.2009.11.037

[63] Hasegawa, S., Imanishi, N., Zhang, T., Xie, J., Hirano, A., Takeda, Y., & Yamamoto, O. (2009). Study on lithium/air secondary batteries—Stability of NASICON-type lithium ion conducting glass–ceramics with water. Journal of Power Sources, 189(1), 371-377. doi:10.1016/j.jpowsour.2008.08.009

[64] Shimonishi, Y., Zhang, T., Imanishi, N., Im, D., Lee, D. J., Hirano, A., . . . Sammes, N. (2011). A study on lithium/air secondary batteries—Stability of the NASICON-type lithium ion conducting solid electrolyte in alkaline aqueous solutions. Journal of Power Sources, 196(11), 5128-5132. doi:10.1016/j.jpowsour.2011.02.023

[65] Zhang, M., Takahashi, K., Imanishi, N., Takeda, Y., Yamamoto, O., Chi, B., Li, J. (2012). Preparation and Electrochemical Properties of Li1 xAlxGe2-x(PO4)3 Synthesized by a Sol-Gel Method. Journal of the Electrochemical Society, 159(7), A1114-A1119. doi:10.1149/2.080207jes

[66] Stevens, P., Toussaint, G., Caillon, G., Viaud, P., Vinatier, P., Cantau, C., Mallouki, M. (2010). Development of a Lithium Air Rechargeable Battery. 1-12. doi:10.1149/1.3507922

[67] Puech, L., Cantau, C., Vinatier, P., Toussaint, G., & Stevens, P. (2012). Elaboration and characterization of a free standing LiSICON membrane for aqueous lithium–air battery. Journal of Power Sources, 214, 330-336. doi:10.1016/j.jpowsour.2012.04.064

[68] Moureaux, F., Stevens, P., Toussaint, G., & Chatenet, M. (2013). Development of an oxygen-evolution electrode from 316L stainless steel: Application to the oxygen evolution reaction in aqueous lithium–air batteries. Journal of Power Sources, 229, 123-132. doi:10.1016/j.jpowsour.2012.11.133

[69] Zhang, T., Imanishi, N., Shimonishi, Y., Hirano, A., Takeda, Y., Yamamoto, O., & Sammes, N. (2010). A novel high energy density rechargeable lithium/air battery. Chemical Communications, 46(10), 1661-1663. doi:10.1039/b920012f

[70] Endo, M., Kim, C., Nishimura, K., Fujino, T., & Miyashita, K. (2000). Recent development of carbon materials for Li ion batteries. Carbon, 38(2), 183-197. doi:10.1016/s0008-6223(99)00141-4

[71] Sharma, S., & Pollet, B. G. (2012). Support materials for PEMFC and DMFC electrocatalysts—A review. Journal of Power Sources, 208, 96-119. doi:10.1016/j.jpowsour.2012.02.011

[72] Luntz, A. C., Viswanathan, V., Voss, J., Varley, J. B., Nørskov, J. K., Scheffler, R., & Speidel, A. (2013). Tunneling and Polaron Charge Transport through Li2O2in Li–O2Batteries. The Journal of Physical Chemistry Letters, 4(20), 3494-3499. doi:10.1021/jz401926f

[73] Lei, Y., Lu, J., Luo, X., Wu, T., Du, P., Zhang, X., Amine, K. (2013). Synthesis of Porous Carbon Supported Palladium Nanoparticle Catalysts by Atomic Layer Deposition: Application for Rechargeable Lithium–O2Battery. Nano Letters, 13(9), 4182-4189. doi:10.1021/nl401833p

[74] Qin, Y., Lu, J., Du, P., Chen, Z., Ren, Y., Wu, T., Amine, K. (2013). In situ fabrication of porous-carbon-supported α-MnO2 nanorods at room temperature: application for rechargeable Li–O2 batteries. Energy & Environmental Science, 6(2), 519-531. doi:10.1039/c2ee23621d

[75] Xu, W., Xiao, J., Zhang, J., Wang, D., & Zhang, J. (2009). Optimization of Nonaqueous Electrolytes for Primary Lithium/Air Batteries Operated in Ambient Environment. Journal of The Electrochemical Society, 156(10), A773-A779. doi:10.1149/1.3168564

[76] Xiao, J., Wang, D., Xu, W., Wang, D., Williford, R. E., Liu, J., & Zhang, J. (2010). Optimization of Air Electrode for Li/Air Batteries. Journal of The Electrochemical Society, 157(4), A487-A492. doi:10.1149/1.3314375

[77] Lin, X., Zhou, L., Huang, T., & Yu, A. (2013). Hierarchically Porous Honeycomb-Like Carbon as a Lithium–Oxygen Electrode. J. Mater. Chem. A, 1(4), 1239-1245. doi:10.1039/c2ta00236a

[78] Mitchell, R. R., Gallant, B. M., Thompson, C. V., & Shao-Horn, Y. (2011). All-carbon-nanofiber electrodes for high-energy rechargeable Li–O2 batteries. Energy & Environmental Science, 4(8), 2952-2958. doi:10.1039/c1ee01496j

[79] Zhang, G. Q., Zheng, J. P., Liang, R., Zhang, C., Wang, B., Au, M., Plichta, E. J. (2011). α-MnO2/Carbon Nanotube/Carbon Nanofiber Composite Catalytic Air Electrodes for Rechargeable Lithium-air Batteries. Journal of The Electrochemical Society, 158(7), A822-A827. doi:10.1149/1.3590736

[80] Etacheri, V., Sharon, D., Garsuch, A., Afri, M., Frimer, A. A., & Aurbach, D. (2013). Hierarchical Activated Carbon Microfiber (ACM) Electrodes for Rechargeable Li–O_2 Batteries. Journal of Materials Chemistry A, 1(16), 5021-5030. doi:10.1039/c3ta01659e

[81] Shen, Y., Sun, D., Yu, L., Zhang, W., Shang, Y., Tang, H., Huang, Y. (2013). A high-capacity lithium–air battery with Pd modified carbon nanotube sponge cathode working in regular air. Carbon, 62, 288-295. doi:10.1016/j.carbon.2013.05.066

[82] Li, J., Peng, B., Zhou, G., Zhang, Z., Lai, Y., & Jia, M. (2012). Partially Cracked Carbon Nanotubes as Cathode Materials for Lithium-Air Batteries. ECS Electrochemistry Letters, 2(2), A25-A27. doi:10.1149/2.009302eel

[83] Liu, S., Wang, J., Zeng, J., Ou, J., Li, Z., Liu, X., & Yang, S. (2010). “Green” electrochemical synthesis of Pt/graphene sheet nanocomposite film and its electrocatalytic property. Journal of Power Sources, 195(15), 4628-4633. doi:10.1016/j.jpowsour.2010.02.024

[84] Seger, B., & Kamat, P. V. (2009). Electrocatalytically Active Graphene-Platinum Nanocomposites. Role of 2-D Carbon Support in PEM Fuel Cells. The Journal of Physical Chemistry C, 113(19), 7990-7995. doi:10.1021/jp900360k

[85] Yoo, E., Kim, J., Hosono, E., Zhou, H., Kudo, T., & Honma, I. (2008). Large Reversible Li Storage of Graphene Nanosheet Families for Use in Rechargeable Lithium Ion Batteries. Nano Letters, 8(8), 2277-2282. doi:10.1021/nl800957b

[86] Jung, H., Jeong, Y. S., Park, J., Sun, Y., Scrosati, B., & Lee, Y. J. (2013). Ruthenium-Based Electrocatalysts Supported on Reduced Graphene Oxide for Lithium-Air Batteries. ACS Nano, 7(4), 3532-3539. doi:10.1021/nn400477d

[87] Li, Y., Wang, J., Li, X., Geng, D., Li, R., & Sun, X. (2011). Superior energy capacity of graphene nanosheets for a nonaqueous lithium-oxygen battery. Chemical Communications, 47(33), 9438-9440. doi:10.1039/c1cc13464g

[88] Liu, S., Zhu, Y., Xie, J., Huo, Y., Yang, H. Y., Zhu, T., Zhang, S. (2014). Direct Growth of Flower-Like δ-MnO 2 on Three-Dimensional Graphene for High-Performance Rechargeable Li-O 2 Batteries. Advanced Energy Materials, 4(9),

1301960. doi:10.1002/aenm.201301960

[89] Xiao, J., Mei, D., Li, X., Xu, W., Wang, D., Graff, G. L., Zhang, J. (2011). Hierarchically Porous Graphene as a Lithium–Air Battery Electrode. Nano Letters, 11(11), 5071-5078. doi:10.1021/nl203332e

Chapter 3

Experimental Procedures

3. 1. Introduction:

Chapter 3 gives a detailed description of the preparation method and the experimental techniques used for the present work. The results and the discussion will be given in the succeeding two chapters.

This chapter is divided into three main sections. The first section is the material synthesis, which covers all the steps taken to prepare the perovskite samples. The second section discusses the material characterization techniques used to study the physical properties of these samples. The last section presents the lithium ionic conductivity measurements of the perovskite samples using the Electrochemical Impedance Spectroscopy (EIS).

3. 2. Material Synthesis:

There are many different procedures to synthesize perovskite materials such as solid-state reaction method, glycine-nitrate method, sol–gel method and freeze drying method. These procedures are used depending on the application of the synthesised material. However, the final structure and purity of the synthesised samples are the most important parameters when choosing the most appropriate synthesis method. [1]

In this work, a Solid-State Reaction (SSR) was the only synthesis method used for the preparation of all perovskites (SLFO and SLFO*). This is done to compare the differences in the lithium ionic conductivity of the prepared perovskite as the ratio of Li^{+} and Sm^{3+} are varied at the A sites. This method is also called

sintering reaction method where the reactants react with each other at high temperature in absence of solvents. The high sintering temperature (500-2000°C) is generally required in this method, because the cation or the anion needs a significant amount of energy to overcome the lattice energy and diffuse into a different site in the perovskite structure. [2]

Samarium lithium iron oxide samples were prepared using Li_2CO_3 (99%), $Sm(NO_3)_3.6H_2O$ (99% REO crystalline) and Fe_2O_3 (99.99% metals basis) or $Fe(NO_3)_3.9H_2O$ (ACS, 98.0-101.0%, crystalline). They were mixed together using an agate mortar and pestle in order to get a fine dry powder. However, the mixture looks like a paste due to presence of H_2O in starting materials. So, the paste was heated in an alumina crucible on the hot pot between 150°C to 200°C for 24 - 30 h to eliminate water. The dry mixture, thus obtained was calcined in the high temperature furnace at 800°C for 4 h with a heating and a cooling ramp rates of 5°C/min. The calcined mixture was again grained using the agate mortar and the pestle to a fine dry powder. The powder (powder weight between 4.5 g to 5.5 g) was pressed to form a pellet using a Pellet Die with diameter of 25 mm, **figure (3. 1. a)**, and a Carver Pellet Press (model 4350) with a pressure of 15000 pounds, **figure (3. 1. c)**. The pellet formed has a thickness of 2 - 3 mm. Then, the pellet is placed on an individual alumina disk for sintering again at 800°C for 4 h with the same heating and cooling ramp rates. The pressing and the sintering steps were repeated twice for both 1100°C for 3 h and 1350°C for 6 h to get better crystal structure in the final perovskite. At 1100°C, the pellets are pressed using a Pellet Die with a diameter of 13 mm, **figure (3. 1. b)**, and the Carver Pellet Press under a pressure of 20000 pounds to get a pellet thickness of 1.5 – 2.5 mm (powder weight between 0.7 g to 1.2 g). While, at 1350°C, the pellets are pressed using the same Pellet Die as at 1100°C, however, the Carver Pellet Press

applied has a pressure of 24000 pounds to attain 1 - 2 mm thick pellet(powder weight between 0.9 g to 1.3 g). The final pellet is used for analysis of prepared perovskite structure using SEM and EDS. The ionic conductivity measurements are performed for this pellet employing EIS.

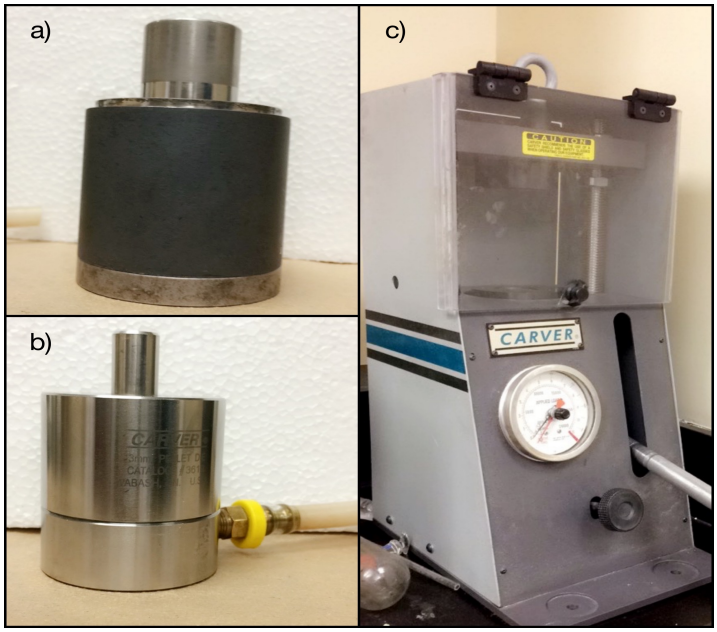

Figure 3. 1: Pellet die with diameter a) 25 mm and b) 13 mm and c) Carver Pellet Press.

3. 3. Material Characterizations:

3. 3. 1. Powder X-Ray Diffraction (PXRD):

Powder X-Ray diffraction is one of the most important techniques used to characterize the solid-state materials. By using this technique, it is possible to determine the physical properties of a crystalline material such as lattice parameters, phase identity, phase purity, crystal structure and the crystallite size. In 1913, William Lawrence Bragg and his father William Henry Bragg gave an explanation to

the diffraction of x-ray pattern in the form of Bragg's Law [3] **equation [3. 1]**, as shown in **figure (3. 2)**:

$$\boldsymbol{n\lambda = 2d\,sin\theta} \qquad [3.1]$$

Where, $\boldsymbol{n}$ is the order of the diffraction peak (1, 2, 3, etc.), $\boldsymbol{\lambda}$ is the wavelength of the x-ray radiation, $\boldsymbol{d}$ is the spacing of the crystal layers and $\boldsymbol{\theta}$ is the incident angle (the angle between incident ray and the scatter plane).

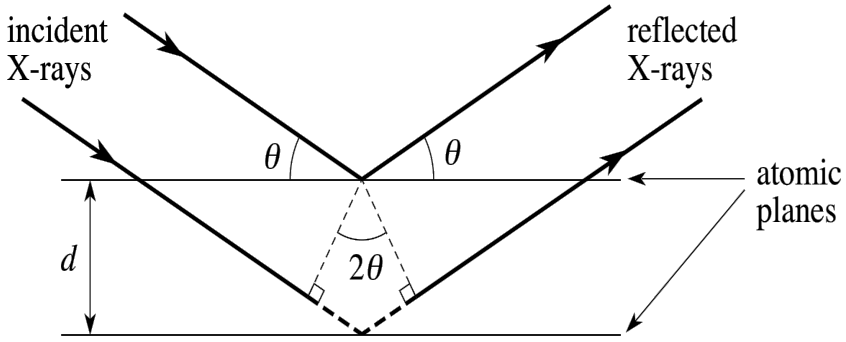

Figure 3. 2: Bragg's Law representation of x-ray diffraction.

It is known that the crystal structure of the material is formed from a repeating block pattern called the unit cell. The size and the shape of the unit cell control the direction of possible diffractions, where as the type and arrangement of atoms in the unit cell control the intensity of the diffracted waves. [3]

In the present work, XRD was performed using an Ultima IV X-ray diffractometer with Cu Kα radiation (λ=1.54 Å). The instrument was operated at room temperature for all perovskite samples and the scattering angle (2θ) was scanned between 20°- 70° at a rate of 0.02°/s. The system is connected to Rigaku PDXL Software (Version 1.8.0.3) designed to analyze the physical properties of the perovskite samples. A diffractogram of standard $SmFeO_3$ with code number of (01-

086-1330) was used to define the phase composition of all perovskite diffractograms. Additionally, the lattice parameters of perovskite unit cell were corrected using the same standard $SmFeO_3$.

3. 3. 2. Surface Structures:

3. 3. 2. 1. *Scanning Electron Microscopy (SEM):*

Scanning Electron Microscopy (SEM) is a significant tool to study the surface structure in the solid-state samples. It can provide scanned images of different spots of the sample surface without cutting the sample into segments.

In this work, the perovskite morphologies were investigated using a JEOL JSM-7500F field emission scanning electron microscopy (FE-SEM). This SEM system can provide high-resolution imaging of large specimen because it collimates the electron beam even at low accelerating voltages (0.1 kV) [4]. It is used mainly to observe the microstructure morphology of a fine surface of the pellet calcined at 1350°C without any assistance of a sprayed coating. Additionally, two different detection modes called low energy secondary electron image (**LEI)** and composition image (**COMPO**) are employed to show the microstructure morphology of the surface at different electron energies. The images of the **LEI** and **COMPO** mode are taken at a magnification of 1000X.

3. 3. 3. 2. *Energy Dispersive X-ray Spectroscopy:*

Energy Dispersive X-ray Spectroscopy (EDS) was used in a combination with SEM to determine the elemental composition of particles formed on the surface of the pellet samples. For EDS experiments, the acceleration voltage of the electron beam was increased from 2 kV to 15 kV. INCA software in combination with EDS was

employed to analyze the imaging spectra that formed using SEM with **COMPO** mode. Square analysis was done at different light and dark spots of the image that represent different elements of the chosen perovskite sample.

3. 4. Ionic Conductivity Measurement:

In solid-state compounds, it is hard to conduct electricity in the neutral state of the material because the ions cannot freely move to different sites. However, the ions can only move in solid electrolytes and conduct current if defects exist in the crystal. The defects in the crystal lattice may take several forms [5], as mentioned in chapter 1 **figure (1. 4)**. The movement of ions in the crystal structure can be explained as the hopping of ions from an occupied site to a vacant site.

One of the most important tools to measure the ionic conductivity for lithium perovskites is Electrochemical impedance spectroscopy (EIS). EIS is a non-destructive technique and gives a physical explanation to the mechanisms or processes involved in an electrochemical cell. It is also called AC Impedance or just Impedance Spectroscopy. For all experiments, a Princeton Applied Research PARSTAT 2273 instrument with Power Suite software were used to measure the AC impedance (Z). The conditions for the experiments were fixed at a sine wave of 10 mV amplitude and over a frequency range of 1 MHz to 100 Hz. In addition, all AC impedance measurements were carried out in the air at room temperature of 25°C.

In this study, all the perovskite pellet samples calcined at 1350°C were analysed through EIS. The first step in this analysis includes the measurement of the pellet dimensions (l = thickness and a = area) before placing it in between the electrodes. Then, the sample is placed in between two similar electrodes called Conductive Lift-N-Press Adhesive Tabs, Double Sided with 0.6 % nickel and < 0.3

% copper content. One side of the electrode was pressed on the sample and the other side of the electrode was used to sandwich the wire with another electrode tab, as shown in **figure (3. 3)**.

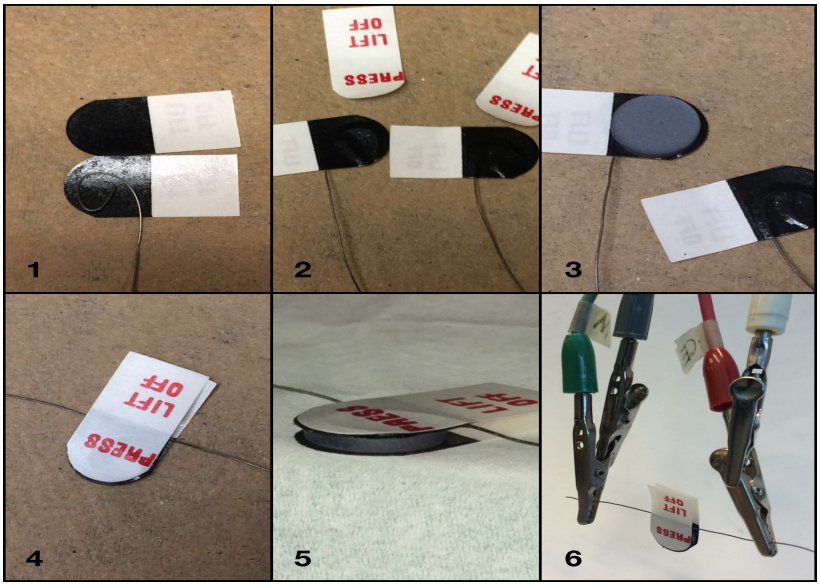

Figure 3. 3: EIS analysis setup for measuring the ionic conductivity of the perovskite.

By using this technique, it is possible to collect impedance as a function of the frequency of the AC signal for different electrode configurations. This can be simply done by connecting the electrode to an impedance analyzer. The AC data can then be graphically presented using Nyquist plot, which is a plot of the imaginary part of impedance Z" versus the real part of impedance Z'. However, it is necessary to fit AC data to an equivalent circuit in order to determine the electrical characteristics of the samples such as resistors (R), constant phase element (Q) and inductors (L).

Impedance fitting was performed using ZSimpWin software. The experimental AC data is fitted with a specific equivalent circuit model $\mathbf{LR_b(QR)_{gb}}$, **figure (3. 4)**, to determine the values of the elements in the equivalent circuit. This equivalent circuit is useful for all Li perovskite in chapter 4 and 5 except for

$Sm_{0.4}Li_{0.4}FeO_3$. For this perovskite, another equivalent circuit $\mathbf{LR_b(QR)_{gb}(Q_{dl}R_{ct})}$, **figure (3. 5)**, is used due to the existing of the second semicircle in the AC actual data, as what is presented in chapter 5.

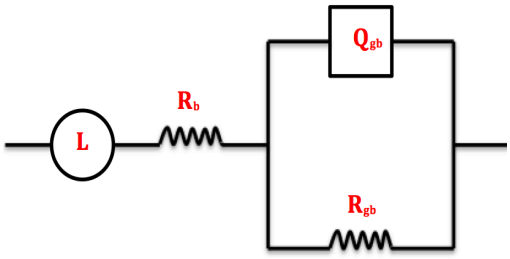

Figure 3. 4: Schematic representation of the equivalent circuit $\mathbf{LR_b(QR)_{gb}}$.

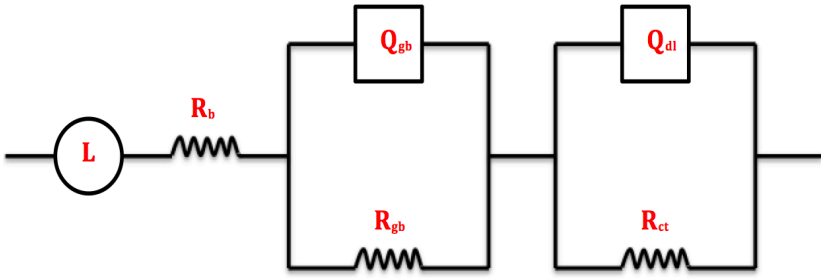

Figure 3. 5: Schematic representation of the equivalent circuit $\mathbf{LR_b(QR)_{gb}(Q_{dl}R_{ct})}$.

Where **L** is the inductor, $\mathbf{R_b}$ is the bulk resistance, $\mathbf{Q_{gb}}$ is the constant phase element for grain boundary resistance, $\mathbf{R_{gb}}$ is the grain boundary resistance, $\mathbf{Q_{dl}}$ **is the** constant phase element for the double layer and $\mathbf{R_{ct}}$ is the electrolyte/electrode interface resistance (charge transfer resistance).

For example, the bulk resistance in the equivalent circuit is present at the highest frequency intercept on the real axis of the Nyquist plot. This value of the bulk resistance is used to calculate the lithium ionic conductivity for each perovskite sample by the following **equation [3. 2]**.

$$\textbf{\textit{The ionic conductivity}}\ (\sigma) = \frac{l}{Z\,.\,a}\quad \textbf{\textit{S.cm}}^{-1} \qquad [3.2]$$

Where l is the thickness of the sample, Z is the bulk resistance impedance and a is the area of the sample.

3. 5. Summary:

This chapter focuses on the experimental set-up and the synthesis procedure for preparing both groups of lithium perovskites. A total of ten Lithium perovskites have been prepared at different Li and Sm concentrations. A detailed description of the experimental conditions for their synthesis method is provided. Standard analysis techniques like the PXRD, SEM, EDS and EIS used to investigate the physical profile of the prepared perovskites are discussed.

3. 6. References:

[1] Mastai, Yitzhak, 1966. (2012). *Advances in crystallization processes / Synthetic Methods for Perovskite Materials – Structure and Morphology*.

[2] Sambandan, E. (2008). *Inorganic Materials Chemistry: General Concepts and Research Topics*. iUniverse.

[3] Fultz, B., Fultz, B., & Howe, J. M. (2013). *Transmission electron microscopy and diffractometry of materials*. Retrieved from http://link.springer.com/chapter/10.1007%2F978-3-642-29761-8_1

[4] Copyright. *JSM-7500F field emission scanning electron microscope*. Retrieved August 2, 2016, from http://www.jeol.co.jp/en/products/detail/JSM-7500F.html#about

[5] Chen, D., Chen, C., Baiyee, Z. M., Shao, Z., & Ciucci, F. (2015). Nonstoichiometric oxides as low-cost and highly-efficient oxygen reduction/evolution catalysts for low-temperature Electrochemical devices. *Chemical Reviews*, *115*(18), 9869–9921. doi: 10.1021/acs.chemrev.5b00073

Chapter 4

Experimental Results and Discussion for the First Group of Lithium Perovskites (SLFO)

4. 1. Introduction:

A new family of perovskite-type oxides with a general formula $Sm_xLi_{1-x}FeO_{2+x}$ (where x = 0.1, 0.2, 0.3, 0.5 and 0.7) have been prepared using a solid-state reaction method. Inserting Li^+ into the lattice at the A site of $SmFeO_3$ perovskite can affect the crystal structure as well as the ionic conductivity. The experimental details for synthesis method, characterization techniques and ionic conductivity measurements are discussed in detail in chapter 3. The synthesised perovskites were characterised by powder X-ray diffraction and SEM techniques and EIS was employed to measure the lithium ionic conductivity for particular samples that were calcined twice at 1350°C for 6 h.

In this following sections, the experimental results and discussion for the first group of lithium perovskite that obtained by the partial substitution of Sm^{3+} by Li^+ in SFO perovskite are discussed in details. Through such a process, we have obtained a lithium perovskite material that has higher lithium ionic conductivity than the previously reported data and has a value of 4.60×10^{-3} S/cm when the lithium concentration equals to 0.7.

4. 2. Experimental Method:

4. 2. 1. Synthesis of the Perovskite Materials:

Samarium lithium ferrite (SLFO) have been synthesized by a sintering method with stoichiometric amounts of Li_2CO_3 (99%), $Sm(NO_3)_3.6H_2O$ (99% REO crystalline)

and Fe_2O_3 (99.99% metals basis) or $Fe(NO_3)_3.9H_2O$ (ACS, 98.0-101.0%, crystalline). All the materials were weighted to obtain the desired metal ratios, as given in **table (4. 1)**, and grinded together by an agate mortar and pestle to get a fine powder. However, since $Sm(NO_3)_3.6H_2O$ and $Fe(NO_3)_3.9H_2O$ release water upon grinding, the fine powder is converted into a paste. The mixture is washed with a small amount of distilled water, and then transferred to a crucible in order to eliminate the amount of water by gently heating on the hot plate at 150°C for one day. After that, the mixture is calcined at 800°C for 4 h with heating and cooling ramp rates of 5°C /min to get a dry mixture. The dry mixture is ground and pressed into a pellet at 15000 pounds with a diameter of 25 mm and thickness between 2 to 3 mm. The pellet is calcined for the second time at 800°C for 4 h with the same heating and cooling ramp rates and then ground into a fine powder. After that, a small amount of the powder was taken for XRD while the remaining powder was pressed into a pellet at 20000 pounds with a diameter 25 mm and a thickness between 1.5 to 2.5 mm. Then, the pellet is calcined for the first time at 1100°C for 3 h with heating and cooling ramp rates of 5°C/ min and then crushed into a fine powder. This step was repeated again with the same conditions and also a small amount of the powder was taken from each step in order to analyse the changes in the crystal structure using XRD. In addition, the remaining powder from the calcination step of heating at 1100°C for the second time was pressed into a pellet at 24000 pounds with a diameter of 13 mm and thickness between 1 to 2 mm. The pellet is fired at 1350°C for 6 h with heating and cooling ramp rates of 5°C/ min and then crushed again into a fine powder to measure the characterization changes by XRD. The remaining powder was pressed into a pellet with the same conditions for the last time and then calcined again at 1350°C for

6h with the same heating and cooling ramp rates. The final sample was then used for further analysis in SEM and EIS.

Table 4. 1: List of the Starting Materials in gram**.**

Perovskite formula	Amount Synthesised (g)	Li_2CO_3 (g)	$Sm(NO_3)_3.6H_2O$ (g)	$Fe(NO_3)_3.9H_2O$ (g)	Fe_2O_3 (g)
$Sm_{0.1}Li_{0.9}FeO_{2.1}$	5	1.331	1.780	16.161	0
$Sm_{0.2}Li_{0.8}FeO_{2.2}$	5	1.060	3.190	0	2.862
$Sm_{0.3}Li_{0.7}FeO_{2.3}$	3	0.504	2.605	0	1.561
$Sm_{0.5}Li_{0.5}FeO_{2.5}$	2	0.202	2.442	4.430	0
$Sm_{0.7}Li_{0.3}FeO_{2.7}$	3	0.124	3.464	0	0.892

4. 2. 2. Physical and Electrochemical Characterization:

4. 2. 2. 1. *Powder X-Ray Diffraction (PXRD):*

The crystal structure of the perovskite samples was identified using powder x-ray diffraction. The Ultima IV X-ray diffractometer instrument [1] was operated at room temperature for all the sample powders calcined at 800°C, 1100°C and 1350°C. The powders were filled and pressed into the sample holder using a glass microscope slide in order to get a flat surface. After that, the diffractograms were scanned in 2θ from 20° to 70° at a rate of 0.02°/s with Cu Kα radiation (λ=1.54 Å). The diffraction data is analyzed by Rigaku PDXL Software (Version 1.8.0.3) [2] to determine the phase composition of the perovskite structure. The lattice parameters were obtained using a standard diffractogram of $SmFeO_3$ with code number of (01-086-1330) [3] in

order to define the effect of inserting lithium ion into the lattice.

4. 2. 2. 2. ***Scanning Electron Microscopy & Energy Dispersive X-ray Spectroscopy:***

Scanning Electron microscopy was employed to observe the microstructure morphology of the pellets that were calcined twice at 1350°C for 6 h using a JEOL JSM-7500F field emission scanning electron microscope (FE-SEM) [4]. (**LEI**) and (**COMPO**) modes were used to compare the microstructure morphology of the surface at low (2-3 eV) and high (15-20 eV) electron energies [5]. The magnification for both modes was set at 1000X and the image of the COMPO mode was analysed using the EDS technique.

Furthermore, Energy Dispersive X-ray Spectroscopy (EDS) was also used in combination with the (SEM) to establish the elemental compositions of particles formed on the surface of pellet samples. However, this technique cannot detect the amount of the lithium composition because it is a light element. Therefore, the results of using this technique were not helpful to compare the elemental compositions for Li perovskite but it was used determine the kind of elements that appeared at different spots in the COMPO image.

4. 2. 2. 3. ***Ionic Conductivity Measurements:***

The lithium ionic conductivity measurements were investigated for pellets that are calcined twice at 1350°C using a Princeton Applied Research PARSTAT 2273 instrument [6]. Power suite software [7] was used in combination with this instrument to detect the impedance measurements using Nyquist plot, which present the relationship between the real value of Z' at x-axis and the imaginary value of Z'' at

y-axis for specific frequency range. Impedance measurements were performed at Ac level of 10 mV rms in the frequency range of 1MHz to 100 Hz.

Moreover, by using ZSimpWin software [8], the EIS data were fitted to an equivalent circuit model **[$LR_b(QR)_{gb}$],** as shown in **figure (4. 1)** and **table (4. 2).,** to determine the bulk resistance value **(R_b)** which is then used to compute the lithium ionic conductivity from **equation [4. 1]**.

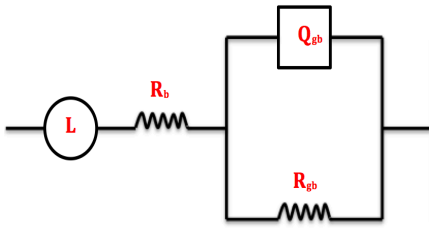

Figure 4. 1: Geometry of the equivalent circuit [**$LR_b(QR)_{gb}$**].

Table 4. 2: Randles Circuit Elements used in the model.

Equivalent element	Description	Impedance
L	Inductance	$j\omega L$
R	Resistance	R
Q	CPE (constant phase element)	$1/\ Y_0\ (j\omega)^{\alpha}$

Where j is the imaginary unit, $\omega = 2\pi f$ is the angular frequency, f is the frequency, Y_0 is the pre-factor of CPE and α is related to the frequency dispersion with the range of 0 to 1 the ($\alpha = 0 \Rightarrow$ Q = Resistance and $\alpha = 1 \Rightarrow$ Q = Capacitor)

$$\textbf{\textit{The ionic conductivity}}\ (\sigma) = \frac{l}{R_b.\ a}\quad S.cm^{-1} \qquad [4.\ 1]$$

Where ***l*** is the thickness of the sample, R_b is the real resistance (bulk resistance), ***a*** is the area of the pellet = $r^2 \times \pi$, r is the radius of the pellet and π is a constant value equals to 3.14.

4. 3. Results:

4. 3. 1. Powder X-ray Diffraction (PXRD):

Powder X-Ray diffraction was used to determine the phase composition of the Li perovskite lattice (LSFO). It is seen that the crystal structure of the unit cell sets in when the material is calcined twice at 800°C for 4h. However, it has a lot of impurity phases (shown as small additional peaks), which can be reduced by increasing the calcination temperature. So, the sample was calcined further at 1100°C and 1350°C and a comparative study was done for all the calcination temperatures and their corresponding PXRD patterns. The PXRD patterns obtained for different calcination temperatures (800°C, 1100°C and 1350°C) at different concentrations of Li+ and Sm3+ are presented in **figures** (**4. 2 - 4. 6)**. From these figures, it is possible to recognise the differences in the peak positions and shapes. For example, as the temperature is increased from 800 C to 1100°C and 1350°C respectively, an impurity phase in the perovskite samples that appears as a result of the preparation method is reduced (e.g. peak labelled ▲ in **figure 4. 3** is present at 800°C and disappears for the higher temperature diffractograms). Also, the shape of X-ray peaks becomes sharper and narrower at 1350°C, which explain the effect of increasing the sintering temperature on the crystal size [9]. Clearly, increasing the sintering temperature can increase the grain size and decrease the grain boundary, which causes crystal growth.

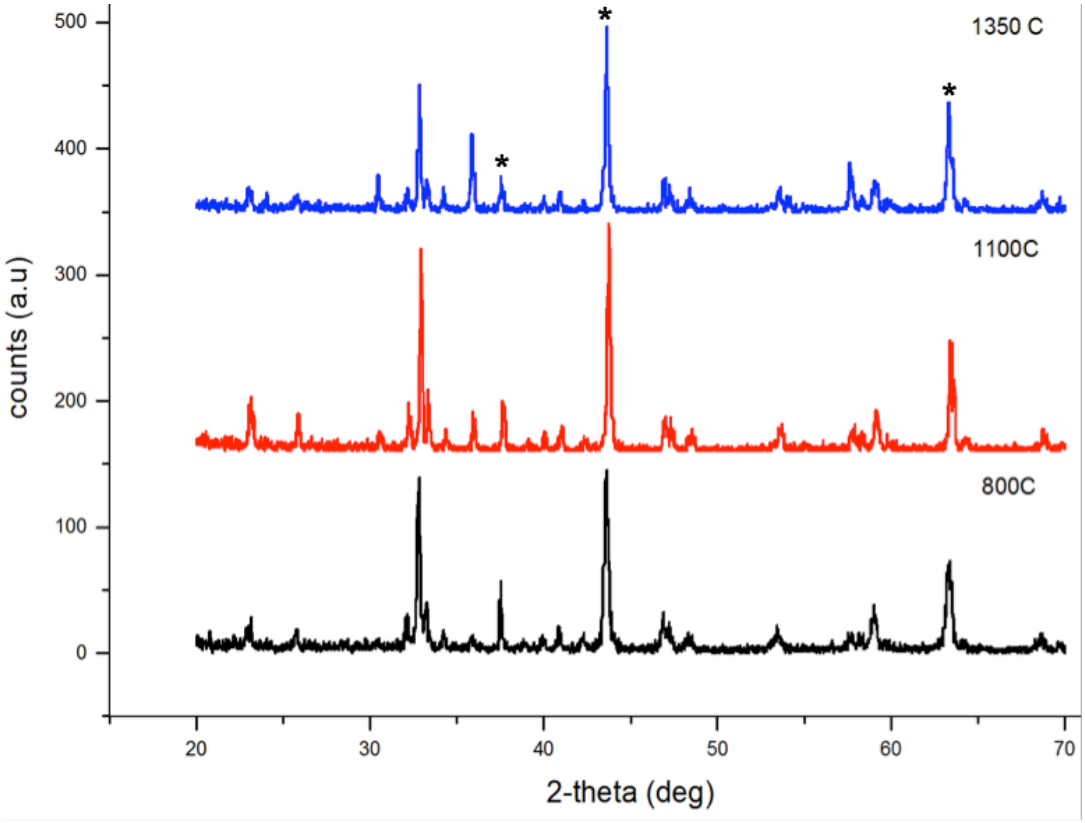

Figure 4. 2: The effect of increasing temperature on the peak position for $Sm_{0.1}Li_{0.9}FeO_{2.1}$, where * presents $LiFeO_2$.

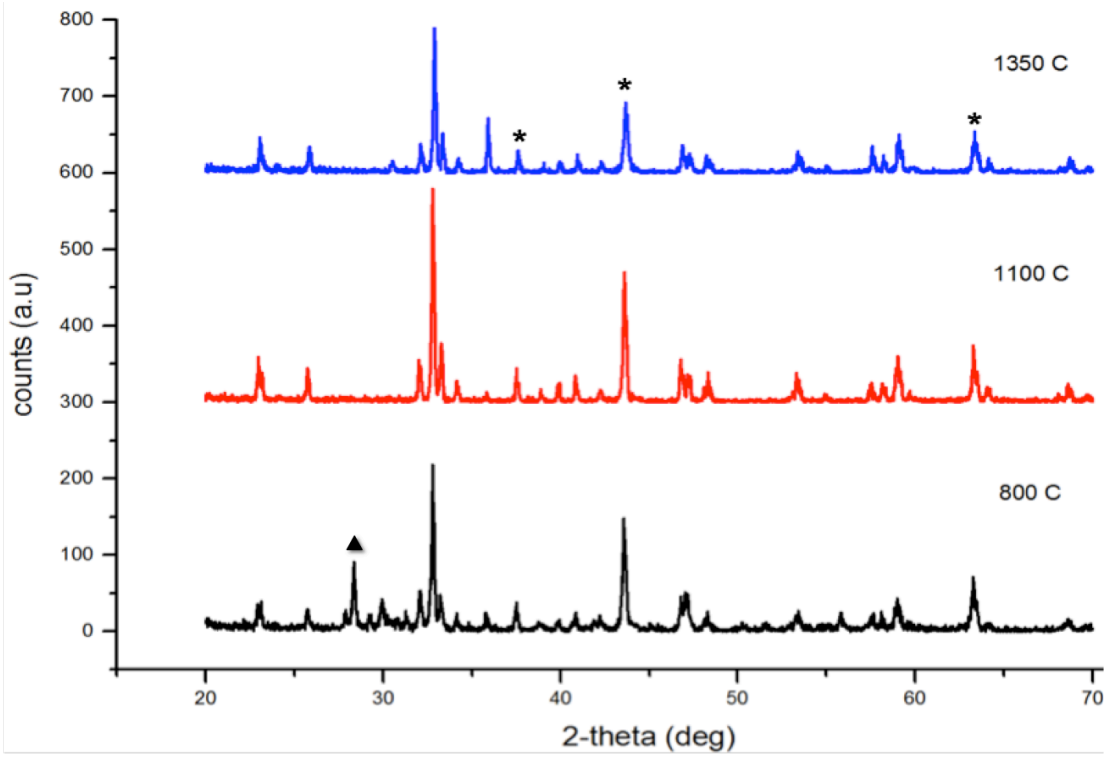

Figure 4. 3: The effect of increasing temperature on the peak position for $Sm_{0.2}Li_{0.8}FeO_{2.2}$, where * presents $LiFeO_2$ and ▲ presents an impurity phase.

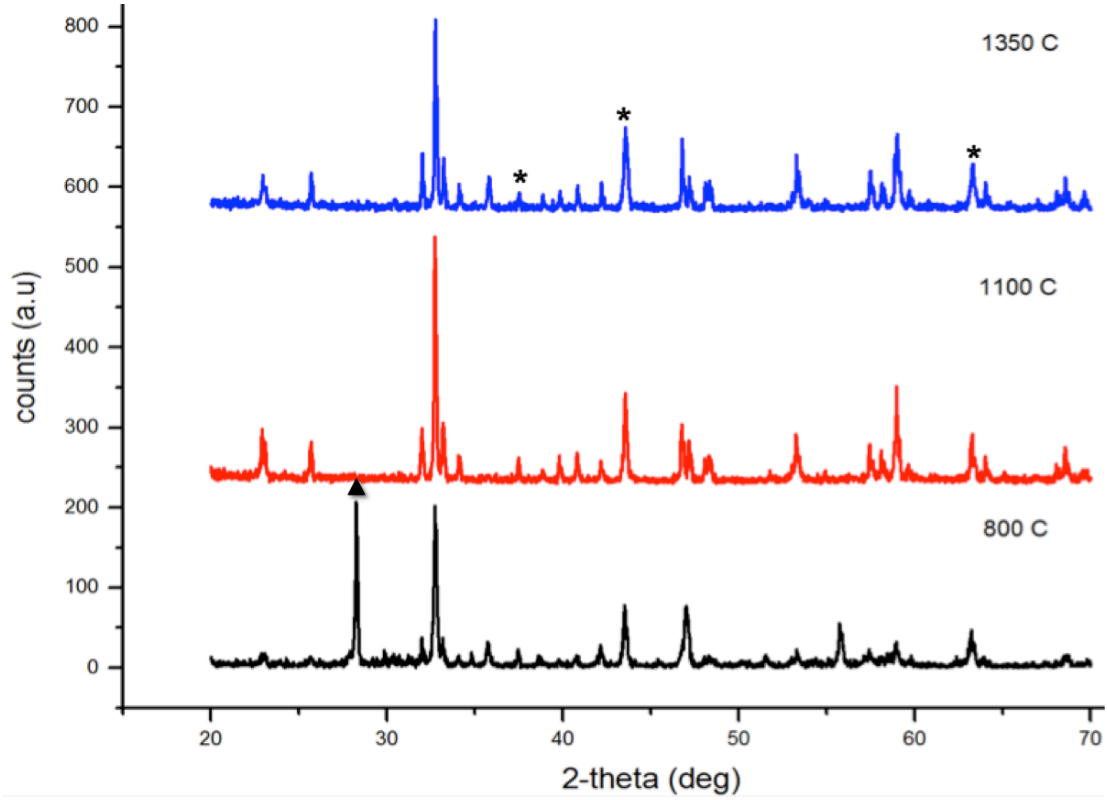

Figure 4. 4: The effect of increasing temperature on the peak position for $Sm_{0.3}Li_{0.7}FeO_{2.3}$, where * presents $LiFeO_2$ and ▲ presents an impurity phase.

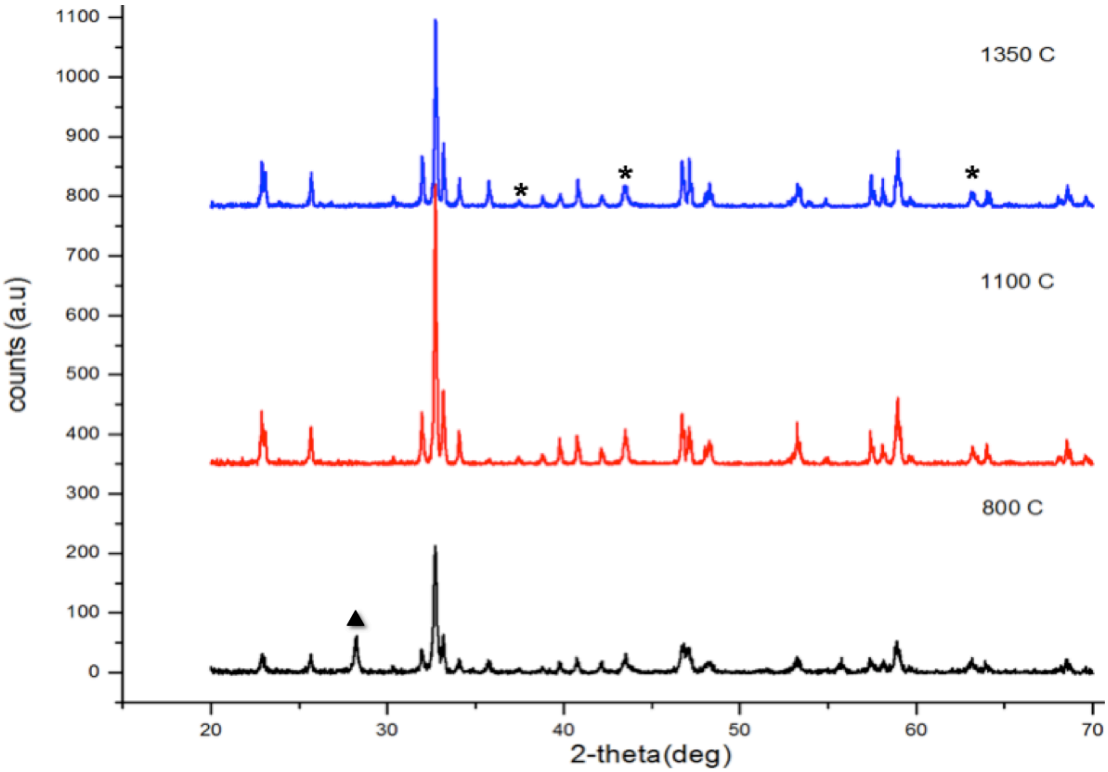

Figure 4. 5: The effect of increasing temperature on the peak position for $Sm_{0.5}Li_{0.5}FeO_{2.5}$, where * presents $LiFeO_2$ and ▲ presents an impurity phase.

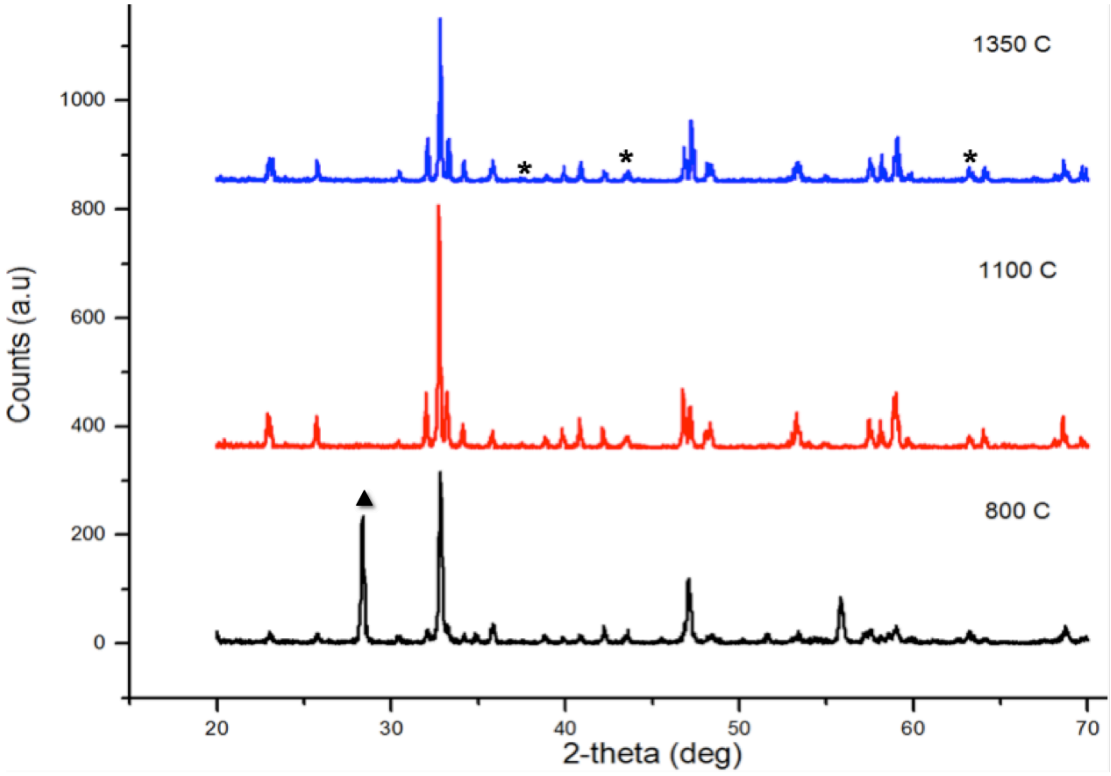

Figure 4. 6: The effect of increasing temperature on the peak position for $Sm_{0.7}Li_{0.3}FeO_{2.7}$, where * presents $LiFeO_2$ and ▲ presents an impurity phase.

For a more clear comprehension of the perovskite structure in each of the materials prepared, the spectra of all the perovskites obtained at 1350°C are compared with the Standard $SmFeO_3$ perovskite and the $LiFeO_2$ in **figure (4. 7)**. Here, all the peaks present in the standard $SmFeO_3$ perovskite are also observed in all SLFO perovskites. As a result, the prominent phase of $SmFeO_3$ is indexed in all SLFO's as an orthorhombic structure and a Pnma (62) space group. Moreover, the lattice parameters of SLFO perovskites were obtained using this standard perovskite as shown in **table (4. 3)**. Nevertheless, five more peaks are observed in all perovskites spectra at 2θ = 30.44, 35.80, 37.52, 43.58 and 63.30, with intensities that vary with Li content. The two peaks at 2θ = 30. 44 and 35.80 have not been clearly identified and perhaps correspond to additional planes by intercalated Li on SmFeO3, since they do not correspond to known lithium compounds. The other three peaks at

2θ = 37.52, 43.58 and 63.30 suggests another separate phase of lithium iron oxide ($LiFeO_2$) (01-070-2711) [10], labelled by (*) in **figures (4. 2 - 4. 6)**. This is consistent with the fact that reducing the amount of lithium that is inserted in the A-site for SLFO perovskites also decreases the $LiFeO_2$ phase. Therefore, the crystal structure consists of a mixture of orthorhombic and cubic phases.

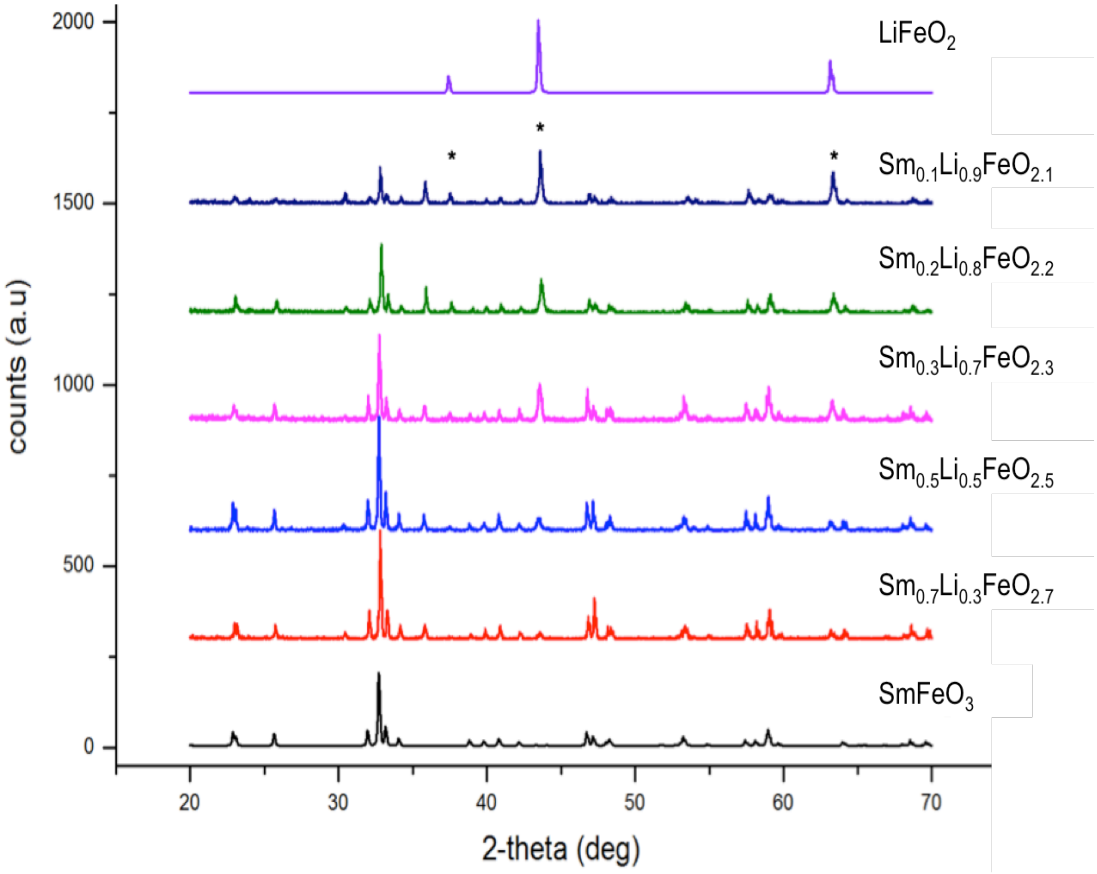

Figure 4. 7: Comparison of XRD patterns for the first group of SLFO perovskites calcined at 1350°C with the Standard $SmFeO_3$ perovskite (01-0861330) and the impurity phase $LiFeO_2$ (01-070-2711).

Figure (4. 7) shows a region of high intensity around 2θ=32º which is the maximum intensity for all the perovskites. Hence, this peak is further analysed to compare peak shifts between samples as represented in **figure (4. 8)**. It is clear that the diffraction peaks are shifted towards higher angle with inserting Li+ into the

perovskite structure compared with the standard $SmFeO_3$ with 2θ = 32.70, which accepted to have lower density volume due the partial substitution of Sm (big atom) with Li (small atoms). For Li+ concentration = 0.5, 0.7 and 0.8, the angle value is increased as 32.72, 32,74, and 32.88 respectively. However, for $[Li^+]$ = 0.3 and 0.9 the same angle value is observed at 32.80. The result of these shifts is reflected in the data presented in **table (4. 3)** for the lattice parameters and the volumes for each perovskite after the correcting by the standard $SmFeO_3$.

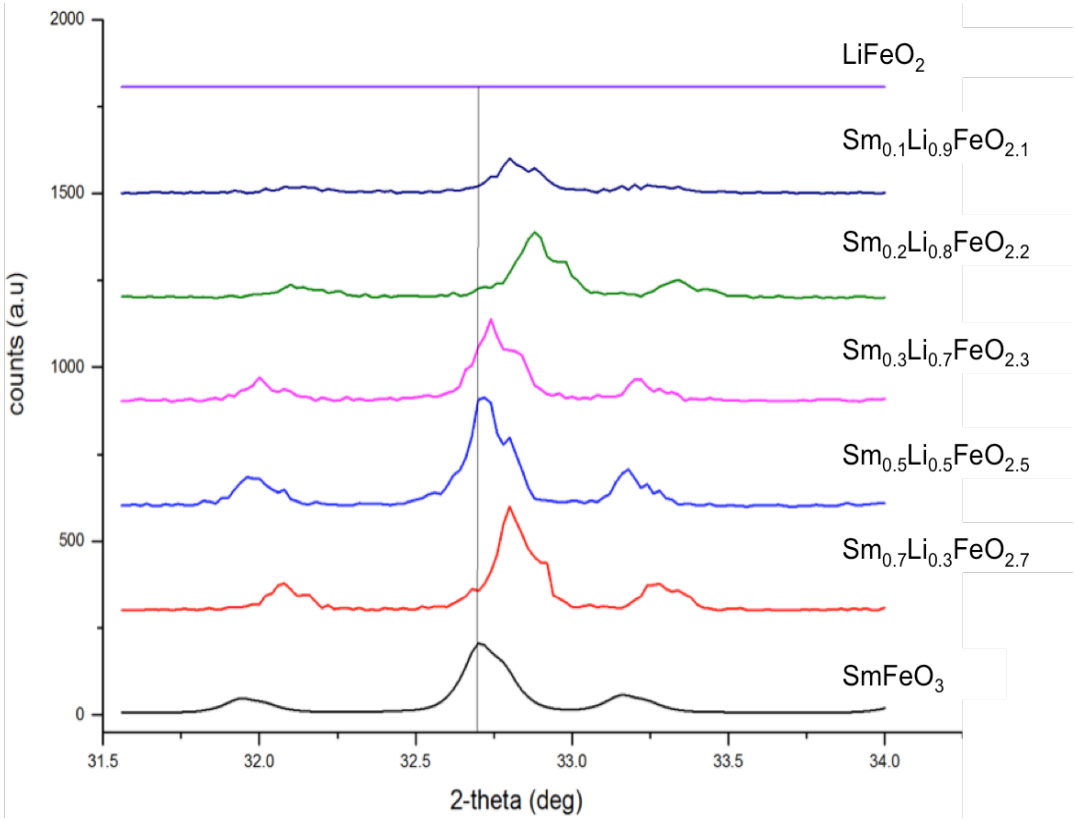

Figure 4. 8: Zoom-in region for the XRD patterns of all samples fired at 1350°C and the Standard $SmFeO_3$ perovskite (01-086-1330) and $LiFeO_2$ phase (01-070-2711).

Table 4. 3: Present lattice parameters for the standard $SmFeO_3$ and the lithium perovskite samples after the corrections using the standard.

Perovskite Formula	a (Å)	b (Å)	c (Å)	Volume ($Å^3$)	Tolerance Factor (t)
$Sm_{0.1}Li_{0.9}FeO_{2.1}$	5.584(6)	7.695(9)	5.386(8)	231.4(5)	0.845
$Sm_{0.2}Li_{0.8}FeO_{2.2}$	5.584(6)	7.686(1)	5.373(9)	230.6(6)	0.852
$Sm_{0.3}Li_{0.7}FeO_{2.3}$	5.600(4)	7.705(8)	5.388(7)	232.5(4)	0.860
$Sm_{0.5}Li_{0.5}FeO_{2.5}$	5.598(2)	7.703(5)	5.395(4)	232.6(3)	0.875
$Sm_{0.7}Li_{0.3}FeO_{2.7}$	5.598(3)	7.699(3)	5.392(2)	232.4(19)	0.890
$SmFeO_3$	5.6001	7.7060	5.3995	233.01	0.913

From these results, it is possible to say that all of the samples contain two phases (SLFO) and ($LiFeO_2$). The presence of the $LiFeO_2$ phase is due to the synthesis method. In addition, the peaks for each SLFO perovskite sample are shifted to higher 2θ value compared with the standard phase $SmFeO_3$. This is due to the replacement of Sm^{3+} (big cation) with Li^+ (small cation) thus decreasing the unit cell volume of the crystal. This shift is, within error, the same for all the peaks in the XRD pattern, which confirms the stability of the perovskite. Moreover, it is possible to check the stability of the perovskites using tolerance factor equation (t) as below:

$$t = \frac{r_A + r_O}{\sqrt{2}\,(r_B + r_O)} \qquad [4.\ 2]$$

where r_A = ionic radius of the A-site, r_B = ionic radius of the B-site and r_O = ionic radius of oxygen ion

In the present work, tolerance factors were calculated using the bond lengths between A cation and O anion ($r_A + r_O$) and between B cation and O anion ($r_B + r_O$). For instance: the bond lengths between Sm-O, Li-O and Fe-O are 2.601 Å, 2.385 Å and 2.015 Å respectively. The bond lengths are calculated as the following equations

$$d_{Sm-O} = 2.088 - 0.37 \log\left(\frac{x=3}{y=12}\right) = 2.601 \text{ Å} \quad [4.3]$$

$$d_{Li-O} = 1.466 - 0.37 \log\left(\frac{x=1}{y=12}\right) = 2.385 \text{ Å} \quad [4.4]$$

$$d_{Fe-O} = 1.759 - 0.37 \log\left(\frac{x=3}{y=6}\right) = 2.015 \text{ Å} \quad [4.5]$$

Where 2.088, 1.466 and 1.759 are the recommended bond valence parameters for Sm, Li and Fe, respectively [11]. 0.37 is an empirical constant and log (x/y) is the logarithm of the ratio of the formal valence to the coordination number of A-site (12) and B-site (6). The present calculations for the Goldschmidt tolerance factor (t) for synthesised perovskites lie within a range of 0.75 to 1.0. Hence, the perovskites synthesised in the present work are stable and can be used for practical purposes.

4. 3. 2. Scanning Electron Microscopy & Energy Dispersive X-ray Spectroscopy:

Scanning electron microscopy produces an image with the help of secondary electrons that gives the view of a three-dimensioned image. In this chapter, it is utilized to observe surface morphologies of lithium perovskite pellets that were calcined at 1350°C for 6 h. **Figure (4. 9)** presents the microstructure morphology of $Sm_xLi_{1-x}FeO_{2+x}$ samples (at x = 0.1, 0.3, 0.3, 0.5 and 0.7). As seen in the figure, there are no pores on the surface morphologies for all the perovskite samples. Cavities and

cracks are observed, caused by a human error during the process of pressing the pellets.

All the lithium perovskite samples are presented in two different modes **(LEI** and **COMPO)** at 1000x magnification. From the **(LEI)** images, it is possible to see different sizes of nanoparticles on the surface. The different morphologies suggest two types of phases in the crystal structure and the **(COMPO)** images clearly show the phase separation on the surface as light and dark particles. From the **COMPO** images, it is possible to determine the change in terms of shape, size and amount of the light and dark particles. For example, at x = 0.1, the amount of the light particles are small and the space between them is large. However, as x is increased to 0.2 and 0.3, the size and the amount of the light particles are increased and the amount of the impurity phase is decreased. While at x = 0.5, the dark and light particles have a crystal shape (have angles) and the number of the light particles is more than the dark ones. In case of x = 0.7, the light particles have larger size than the previous perovskites particles and the intermediate spaces are greatly reduced. So, it is assumed that, the light particles contain the Lithium perovskite phase and the dark partials contain the $LiFeO_2$ phase. This assumption is confirmed through EDS analysis performed for all samples. The results of the EDS analysis are presented in **table (4. 4)**. The dark areas on the image indicate the presence of Fe and O, while at the light spots Sm, Fe and O are seen. This is consistent with the high atomic number of Sm which has a large cross section for electron scattering. By the same token, lithium cannot be detected using EDS because it is a light (small atomic number) element. Increasing the Samarium concentration from x= 0.1 to 0.7 increases the amount of the light particles in the **COMPO** image, which suggest that the light

particles are based on the SLFO perovskite structure while the dark particles would be primarily formed by lithium iron oxide.

LEI Mode **COMPO Mode**

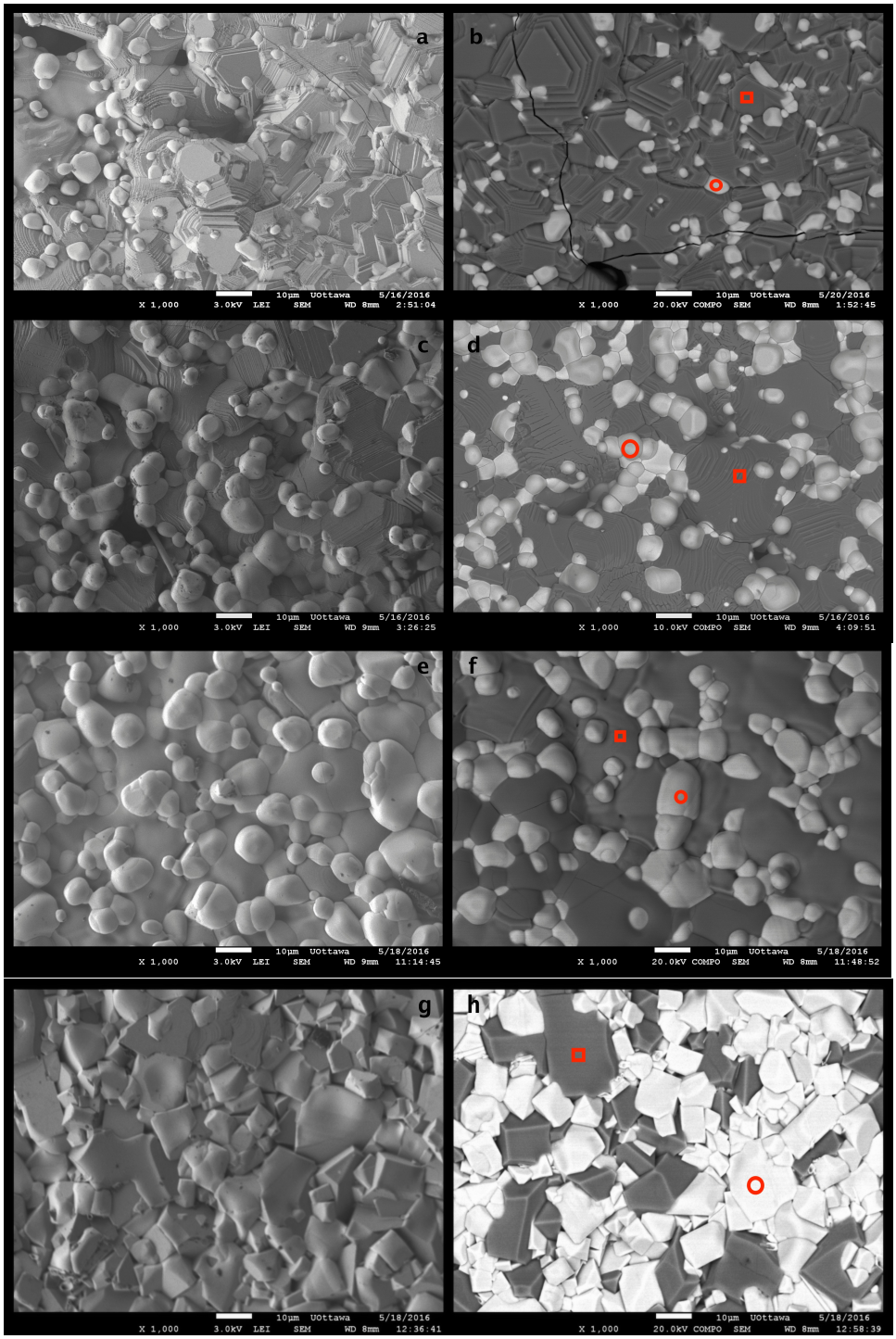

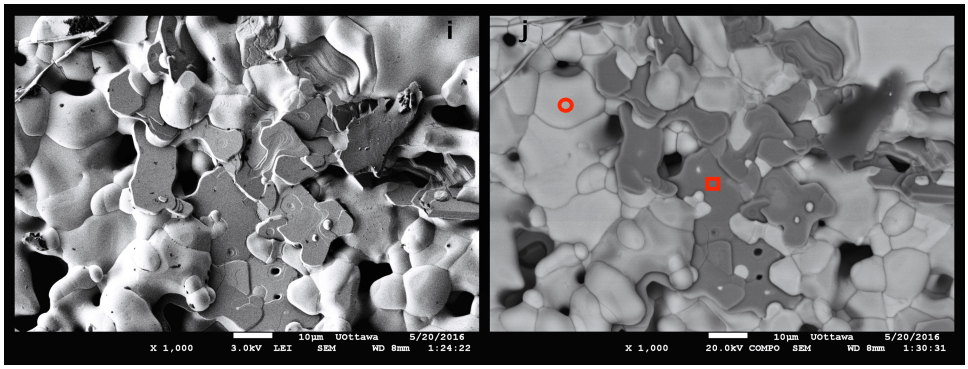

Figure 4. 9: SEM images for all SLFO Perovskites ($Sm_{[x]}Li_{[1-x]}FeO_{2+x}$) calcined at 1350°C for 6 h, a) and b) for x=0.1, c) and d) for x=0.2, e) and f) for x= 0.3, g) and h) for x= 0.5 and i) and j) for x= 0.7. a, c, e, g, i obtained by LEI detection; b, d, f, h, j collected by COMPO detection. Areas marked in red correspond to locations where EDS measurements were performed.

Table 4. 4: EDS results obtained from COMPO images for the first group of SLFO.

Perovskite Formula	Dark Area □		Light Area ○	
	Element	Atomic %	Element	Atomic %
$Sm_{0.1}Li_{0.9}FeO_{2.1}$	O K	76.41	O K	73.83
	Fe K	23.30	Fe K	12.63
	Sm L	0.28	Sm L	13.54
$Sm_{0.2}Li_{0.8}FeO_{2.2}$	O K	78.59	O K	79.60
	Fe K	21.52	Fe K	10.95
	Sm L	0.11	Sm L	9.94
$Sm_{0.3}Li_{0.7}FeO_{2.3}$	O K	78.17	O K	75.61
	Fe K	21.93	Fe K	12.45
	Sm L	0.10	Sm L	11.94
$Sm_{0.5}Li_{0.5}FeO_{2.5}$	O K	74.20	O K	74.60
	Fe K	25.43	Fe K	12.99
	Sm L	0.37	Sm L	12.41
$Sm_{0.7}Li_{0.3}FeO_{2.7}$	O K	73.41	O K	69.49
	Fe K	26.45	Fe K	15.94
	Sm L	0.14	Sm L	14.57

4. 3. 3 The Ionic Conductivity Measurements:

Most oxide perovskites are electrical insulators. However; they may allow charge transport and therefore conductivity (particularly ionic) due to their tendency to arrange with a large number of structure defects. There are different ways to explain the conductivity in the perovskite, most commonly is the ionic conductivity. The defect structure is due to the replacement of one or more atoms by either donors or acceptors atoms. In this case, replacing Sm^{3+} by Li^{+} would increase the electrical charge of the perovskite by +2 and change the electrical neutrality of the perovskite. To preserve this electrical neutrality, oxygen ions leave the structure leaving behind a large network of vacancies. The highly defective structure allows the rapid movement of the small Li ions through the electrolyte. Hence, inserting Li^{+} to the $SmFeO_3$ perovskite makes the perovskite conducting.

Impedance spectroscopy is considered as a beneficial technique to measure the ionic conductivity since it can distinguish between different resistance contributions such as bulk, grain boundary and electrode resistance. In the present work, it was applied to measure the ionic conductivities for all the lithium perovskite pellets that are calcined at 1350°C for 6 h using two similar carbon based electrodes called Conductive Lift-N-Press Adhesive Tabs, Double Sided with 0.6% nickel and <0.3% copper content. The measurements were performed in a frequency range from 1 MHz to 100 Hz and a sine wave = 10 mV amplitude at room temperature. The experimental setup is previously presented in chapter 3.

The AC data was analysed by means of the Randles equivalent circuit $\mathbf{[LR_b(QR)_{gb}]}$. This equivalent circuit has been chosen because it is the best equivalent circuits that match our actual AC data. Additionally, similar circuit $\mathbf{[LR_b(QR)_{gb}]}$ was used in many studies previously to measure the lithium ionic

conductivity. However, this circuit did not match our AC data. Thus, **C** was replaced with **Q** to introduce the behavior of the imperfect capacitor, which may appear as a result of the distribution in some physical property of the system.

In **figure (4. 10)**, it is possible to see the Nyquist plots of AC impedance measurement for all SLFO perovskites. For all samples, just a curve portion data were obtained in high and low frequency regions. Also, the fits in the figure below are good for the high frequency but not for low frequency. This is due to the noise appearing in the low frequency region for the actual AC data, which is attributed to presence of the impurity phase $LiFeO_2$ in the perovskite samples.

$[LR_b(QR)_{gb}]$ was used via the ZSimpWin software to investigate the bulk resistance **(R_b)** and the grain boundary resistance **(R_{gb})** for all SLFO samples. After that, the values of the bulk resistance were employed to measure the lithium ionic conductivity for each perovskite using **equation [4. 1]** as mentioned before.

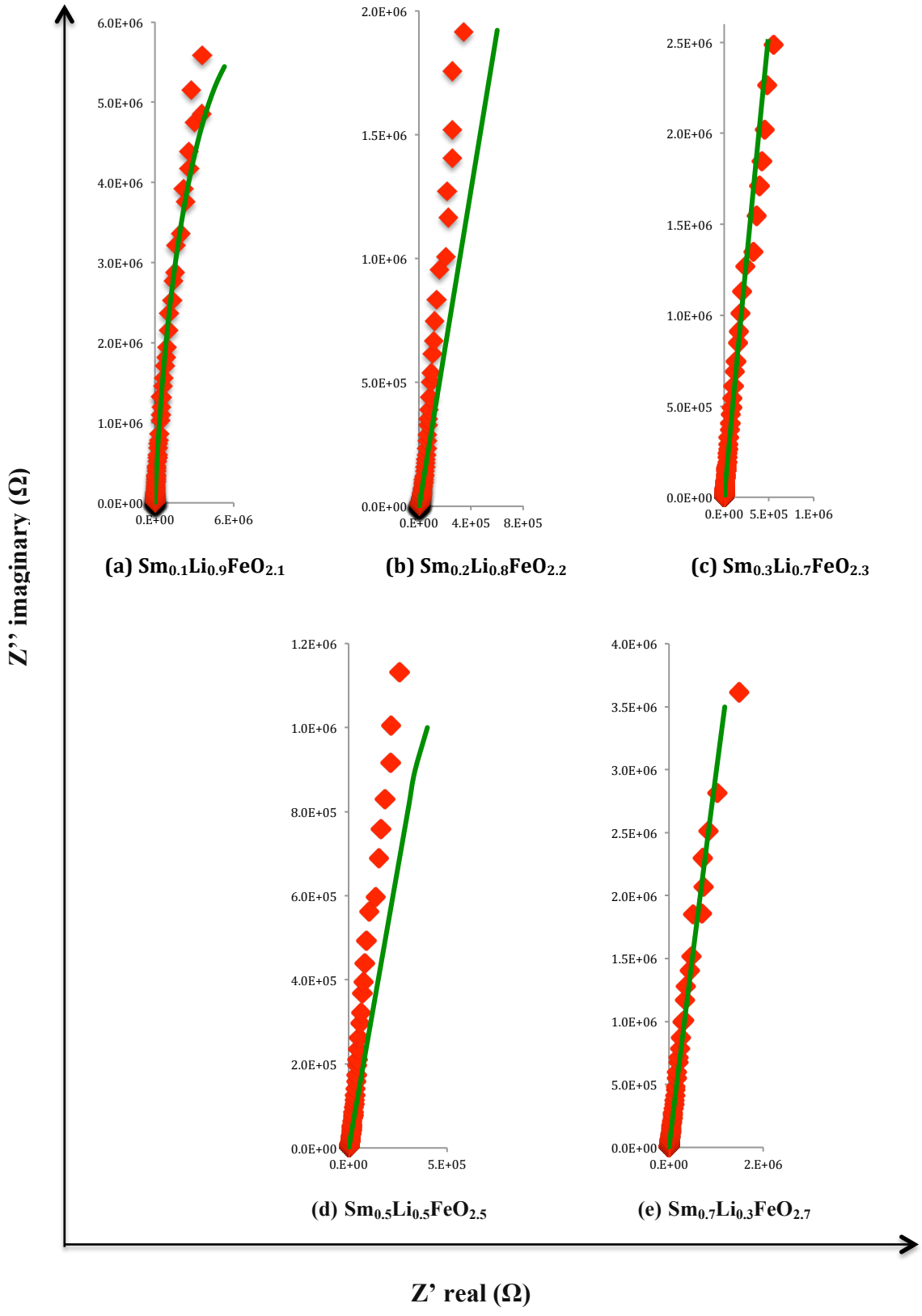

Figure 4. 10: Nyquist plots present the AC data measurement points in red color and the calculated fitting curve in green color for the first group of lithium perovskites SLFO calcined at 1350°C for 6 h.

The value of $\mathbf{R_b}$ is obtained at the high frequency for all the perovskite samples and corresponds to the movement of the lithium ions in the bulk. However, for 0.9 mol of Li^+ concentration, it is difficult to obtain a valid value of $\mathbf{R_b}$ in the high frequency region using this equivalent circuit. This is due to the presence of enormous amount of the $LiFeO_2$ phase, which obstructs the diffusion of the lithium ions inside the bulk. So, the value of the $\mathbf{R_b}$ for this concentration is arbitrarily assumed to be 0.01 as it cannot be zero or negative. The value of the $\mathbf{R_{gb}}$ cannot be directly obtained from the actual AC data because the frequency range was limited to 100Hz. Therefore the calculated data is interpolated to obtain a semicircle where the other end of the complete plot gives the value of the $\mathbf{R_{gb}}$. The values of all the components of the equivalent circuit are given in **table (4. 5)**. In addition, **table (4. 6)** gives the calculated ionic conductivity for all the perovskite samples. This is shown graphically in **figure (4. 11)** giving a comparison between the lithium atomic concentration for the perovskites and the ionic conductivities in (S/cm) that are calculated previously.

Table 4. 5: The calculation components of the equivalent circuit.

Perovskite Formula	L[b] (Ω.s)	R_b (Ω)	Q_{gb} (s/ Ω)	R_{gb} (Ω)
$Sm_{0.1}Li_{0.9}FeO_{2.1}$[a]	3.54×10^{-14}	0.01	4.11×10^{-10}	1.67×10^{7}
Rel. Std. Error (%)	2.67×10^{11}	2.97×10^{6}	9.967	15.1
$Sm_{0.2}Li_{0.8}FeO_{2.2}$	1.10×10^{-14}	1428	2.73×10^{-9}	8.25×10^{13}
Rel. Std. Error (%)	4.43×10^{11}	13.75	9.055	8.29×10^{7}
$Sm_{0.3}Li_{0.7}FeO_{2.3}$	3.13×10^{-17}	315.6	1.39×10^{-9}	2.78×10^{8}
Rel. Std. Error (%)	2.19×10^{13}	14.79	2.647	5.143
$Sm_{0.5}Li_{0.5}FeO_{2.5}$	1.03×10^{-18}	450.7	7.15×10^{-9}	8.22×10^{15}
Rel. Std. Error (%)	1.93×10^{15}	18.73	10.98	8.81×10
$Sm_{0.7}Li_{0.3}FeO_{2.7}$	3.06×10^{-13}	624.7	1.49×10^{-9}	1.65×10^{8}
Rel. Std. Error (%)	5.65×10	59.67	5.899	14.76

[a] This material was non-conductive. This resulted in a nonsensical error in the measurement of resistances.
[b] Fitting of the inductance component is included here only for completeness, but the number of points in the fitting and the intrinsic nature of this data produce very large errors.

Table 4. 6: The lithium ionic conductivity calculation.

Perovskite Formula	Real resistance Z' (Ω)	Pellet thickness (mm)	Pellet Radius r (mm)	Ionic Conductivity α (S/cm). 10^{-3}
$Sm_{0.1}Li_{0.9}FeO_{2.1}$	0.01	2.06	6.308	Non
$Sm_{0.2}Li_{0.8}FeO_{2.2}$	1428	1.84	6.133	1.09
$Sm_{0.3}Li_{0.7}FeO_{2.3}$	315.6	1.74	6.1915	4.60
$Sm_{0.5}Li_{0.5}FeO_{2.5}$	451	1.29	6.033	2.50
$Sm_{0.7}Li_{0.3}FeO_{2.7}$	624.7	1.23	6.1165	1.68

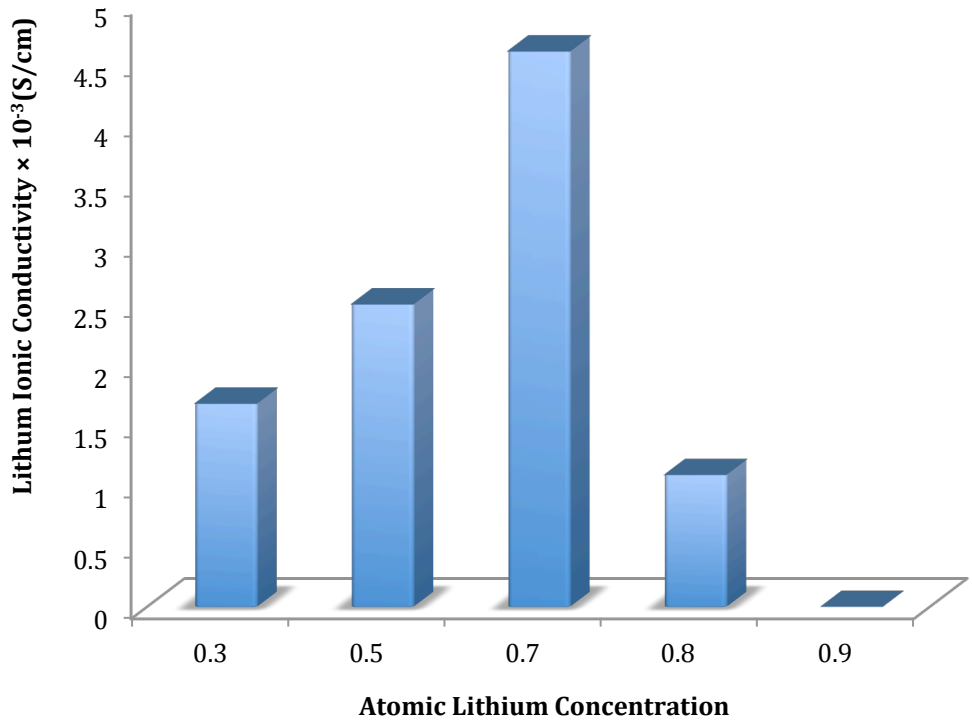

Figure 4. 11: Lithium ionic conductivity in (S/cm) versus and atomic lithium concentration for the first group of SLFO with formula of $Sm_xLi_{1-x}FeO_{2+x,}$ where (x = 0.1, 0.2, 0.3, 0.5 and 0.7).

4. 4. Discussion:

The presence of the impurity phase of $LiFeO_2$ observed in the XRD patterns and SEM images can affect the ionic conductivity of the lithium perovskites when the Li concentration is changed from 0.3 to 0.9. It is seen that the perovskite has lithium ionic conductivity for lithium ion concentrations from 0.3 to 0.8. However, the lithium ionic conductivity becomes null for 0.9 Lithium concentration. Also, Using different Fe sources during the synthesis for these perovskites, which are $Fe(NO_3)_3.9H_2O$ and Fe_2O_3, did not show any influence in the results as presented in previous sections. Thus, the presence of ionic conductivity for the Li concentrations with values 0.3-0.8 is due to the small space between lithium perovskite particles that help lithium ions to hop from one site to another. On the other hand, the $LiFeO_2$ phase for 0.9 Li concentration builds larger spacing between the SLFO perovskite particles that obstructs the mobility of the lithium ion inside the crystal. This impurity phase is not showing any ionic conductivity since it is an electronic conductor [12]. Also, it is possible to confirm the ionic conductivity is coming form the SLFO perovskites and not from the $LiFeO_2$ phase when Li concentration = 0.9 mol. This perovskite shows no ionic conductivity although it has a large amount of $LiFeO_2$. So the ionic conductivity in these samples is coming from the SLFO perovskite partials it is depend on the lithium ion concentration and the spaces between the perovskite partials inside the sample.

The dependence of ionic conductivity on the Li^+ concentration for each perovskite sample is summarized below:

$Sm_{0.1}Li_{0.9}FeO_{2.1}$

Increasing the amount of lithium ions to 0.9 at the A-site is still giving the perovskite structure of $SmFeO_3$ family, but the amount of the secondary phase increases

considerably. This results in huge spaces between the LSFO perovskite particles preventing the conduction of the lithium ions.

$Sm_{0.2}Li_{0.8}FeO_{2.2}$

Adding 0.8 mol of the lithium ions and 0.2 mol of the samarium ions to the A-sites of the perovskite structure is also giving a good ionic conductivity equals to 1.09×10^{-3} S /cm. However, the ionic conductivity is less than the value for other perovskites due to large amounts of impurity phases in the crystal structure.

$Sm_{0.3}Li_{0.7}FeO_{2.3}$

Inserting 0.7 mol of the lithium ions and 0.3 mol of the samarium ions at the A- sites gives the maximum ionic conductivity of 4.60×10^{-3} S /cm. The increased amount of the lithium ions contributes towards the higher ionic conductivity of this perovskite, and it appears that at this concentration the distance between equivalent Li sites facilitates mobility.

$Sm_{0.5}Li_{0.5}FeO_{2.5}$

Increasing the lithium concentration to 0.5 and reducing the samarium concentration to 0.5 generates more mobile Li+ in the crystal that further increases the ionic conductivity of the perovskite. The value of ionic conductivity for this perovskite material is 2.50×10^{-3} S /cm.

$Sm_{0.7}Li_{0.3}FeO_{2.7}$

Adding 0.7 mol of samarium ions and 0.3 mol of lithium ions at the A-site increase the number of conducting particles in the perovskite structure which gives good lithium ionic conductivity having a value of 1.68×10^{-3} S /cm.

4. 5. Conclusion:

Chapter 4 presents the results and the discussion for the first group of the lithium perovskite materials with formula of $Sm_xLi_{1-x}FeO_{2+x}$ (x= 0.1, 0.2, 0.3, 0.5 and 0.7). The highest lithium ionic conductivity obtained was 4.60×10^{-3} S/cm for Li= 0.7, which is larger than the lithium ionic conductivity for **(LLTO)** as discussed in chapter 1. The high lithium ionic conductivity is attributed to the increase in the lithium concentration to 0.7, which means increase in the number and the mobility of the charge carriers. In addition, the decrease in the lithium ionic conductivity after raising the lithium concentration to 0.8 is due to the saturation of the lithium ions at A-sites of the perovskite compared to samarium ions, hence reducing the number of charge carriers. For 0.9 Li concentration, the ionic conductivity becomes non-existent due to the huge amounts of the impurity phases in the crystal.

4. 6. References:

[1] Multipurpose X-ray diffraction system. (n.d.). Retrieved from http://www.rigaku.com/en/products/xrd/ultima

[2] Rigaku PDXL Software Version 1.8.0.3 Copyright 2007. (n.d.). Retrieved from http://manualzz.com/doc/6701023/rigaku-pdxl-software-version-1.8.0.3-copyright-2007.

[3] I. http://www.icdd.com/. ($SmFeO_3$) (01-086-1330).

[4] S. S. JSM-7500F Scanning Electron Microscope by JEOL USA. (n.d.). Retrieved from http://www.selectscience.net/products/jsm-7500f-scanning-electron microscope/?prodID=106753.

[5] Bukhari, S. M., & Giorgi, J. B. (2013). Ni doped Sm0.95Ce0.05FeO3−δ perovskite based sensors for hydrogen detection. Sensors and Actuators B: Chemical, 181, 153-158. doi:10.1016/j.snb.2013.01.073.

[6] European Virtual Institute for Speciation Analysis (EVISA). Princeton Applied Research - PARSTAT 2273. (n.d.). Retrieved from http://www.speciation.net/Database/Instruments/Princeton-Applied-Research/PARSTAT-2273-;i109.

[7] PowerSuite Software | Voltammetry | Princeton Applied Research. (n.d.). Retrieved from http://www.ameteksi.com/products/software/powersuite-software.

[8] ZSimpWin. (n.d.). Retrieved from http://www.ameteksi.com/products/software/zsimpwin.

[9] Vidal, K., Ortega-San-Martín, L., Larrañaga, A., Merino, R. I., Orera, A., & Arriortua, M. I. (2014). Effects of synthesis conditions on the structural, stability and ion conducting properties of Li0.30(La0.50Ln0.50)0.567TiO3 (Ln=La, Pr, Nd) solid electrolytes for rechargeable lithium batteries. Ceramics International, 40(6), 8761-8768. doi:10.1016/j.ceramint.2014.01.097

[10] I. http://www.icdd.com/. ($LiFeO_2$) (01-070-2711).

[11] Brese, N. E., & O'Keeffe, M. (1991). Bond-Valence Parameters for Solids . Acta Cryst, B47, -192-197. Retrieved October 3, 1990, from http://slapper.apam.columbia.edu/bib/papers/brese_acb91.pdf

[12] Lan, R., & Tao, S. (2014). High Ionic Conductivity in a LiFeO2-LiAlO2Composite Under H2/Air Fuel Cell Conditions. Chemistry - A European Journal, 21(3), 1350-1358. doi:10.1002/chem.201404476

Chapter 5

Experimental Results and Discussion for the Second Group of Lithium Perovskites (SLFO*)

5. 1. Introduction:

As seen in the previous chapter, inserting Li^+ into the lattice at the A-site of the $SmFeO_3$ perovskite can increase the ionic conductivity. For this reason, it would be useful to consider the synthesis of a second group of lithium perovskite by inserting Li^+ into the lattice and generating one or more vacancies at the A-sites of the perovskite. The presence of vacancies in these perovskites can improve the ionic conductivity because it allows the lithium ions to hop or jump easily from one site to another when the system is operated [1]. The general formula of this group is $Sm_{(x)}Li_{([1-x] - [0.1] \text{ or } [0.2])}FeO_{3-\delta}$ (where x = 0.3, 0.4, 0.5 and 0.6). These perovskites have been synthesised and characterized using the same approach as discussed in chapter 3. The synthesis and characterization procedures are kept similar to evaluate the change in lithium ionic conductivity for both groups of lithium perovskites (SLFO) and (SLFO*).

In the following subsections, the experimental results for the second group of lithium perovskites will be discussed. The endeavour of the present work is to achieve the highest lithium ionic conductivity for the second group. The perovskites for the second group are obtained by the partial substitution of Sm^{3+} by Li^+ in SFO perovskite and then creating vacancies at the A sites using three different ways: 1) stabilizing Sm ions at 0.3 mol and reducing the amount of Li ions by 0.1 or 0.2 mol; 2) stabilizing the amount of lithium ions at 0.3 mol and reducing Sm ions by 0.1 or

0.2 mol; 3) reducing both of Sm and Li ions by 0.1 mol. Through this process, the highest lithium ionic conductivity is obtained for $Sm_{0.3}Li_{0.6}FeO_3$ equals to $2.8*10^{-2}$ S/cm.

5. 2. Experimental Procedure:

5. 2. 1. Synthesis of the Perovskite Materials:

As mentioned in chapter 3, all of the samarium lithium ferrite materials with the formula $Sm_{(x)}Li_{([1- x] - [0.1or\ 0.2])}FeO_{3-\delta}$ (where x = 0.3, 0.4, 0.5 and 0.6) were synthesized using solid state reaction method (SSR). A measured amount of each starting material, Li_2CO_3 (99%), $Sm(NO_3)_3.6H_2O$ (99% REO crystalline) and $Fe(NO_3)_3.9H_2O$ (ACS, 98.0-101.0%, crystalline), was used to prepare these perovskites, as shown in **(table 5. 1)**. The balanced materials were then mixed together in a mortar and transferred into a crucible to be heated on the hot plate at 200°C for 24 h. This step had to be done before the calcination step in order to eliminate the water content in the starting materials. The dry mixture was calcined at 800°C for 4 h with heating and cooling ramp rates of 5°C /min and grained using the mortar and pestle to get a fine powder. Then, it was pressed into a pellet with a diameter of 25 mm and a pressure of 15000 pounds to obtain a pellet thickness between 2.5 to 3 mm. The pellet was calcined in the furnace for the second time under the same conductions. After the second calcination at 800°C, this pellet was grained into a fine powder and then a small amount of the powder was used for XRD measurement. The remaining powder was pressed again into a pellet at 20000 pounds with the Press diameter of 25 mm to get a thickness between 2 to 2.5 mm. Then, it was calcined at 1100°C for 3 h with heating and cooling ramp rates of 5°C/ min. The calcined pellet was grained again into a fine powder then pressed under the same

conditions. The pellet was calcined for the second time at 1100°C for 3 h with the same heating and cooling ramp rates. It was further grained into a fine powder and a small amount was used for XRD measurement. The remaining powder was pressed into a pellet at 24000 pounds by the Press with a diameter of 13 mm to get the pellet thickness between 1.5 to 2 mm. At the last, the pellet was calcined at 1350°C for 6 h with heating and cooling ramp rates equal to 5°C/min. The calcined pellet was grained into a fine powder and a slight amount was taken for XRD analysis. The powder was pressed for the last time into a pellet at 24000 pounds with Press diameter of 13 mm to obtain a pellet thickness that lies between 1 to 2 mm. The pellet was calcined again at 1350°C for 6 h with the same heating and cooling rate conditions and employed for SEM and EDS to study the structure morphology and EIS to measure the ionic conductivity.

Table 5. 1: List of the Starting Materials in gram**.**

Perovskite formula	Amount of the material (g)	Li_2CO_3 (g)	$Sm(NO_3)_3.6H_2O$ (g)	$Fe(NO_3)_3.9H_2O$(g)
$Sm_{0.3}Li_{0.6}FeO_{3-\delta}$	5	0.5105	3.0715	12.9399
$Sm_{0.3}Li_{0.5}FeO_{3-\delta}$	5	0.6060	4.3742	13.2531
$Sm_{0.4}Li_{0.4}FeO_{3-\delta}$	5	0.4435	5.3313	12.1131
$Sm_{0.5}Li_{0.3}FeO_{3-\delta}$	7	0.4216	8.4506	15.3610
$Sm_{0.6}Li_{0.3}FeO_{3-\delta}$	7	0.3897	9.3744	14.2050

5. 2. 2. Physical and Electrochemical Characterization:

5. 2. 2. 1. *Powder X-Ray Diffraction (PXRD):*

Ultima IV X-ray diffractometer instrument [2] and Rigaku PDXL Software (Version 1.8.0.3) [3] were used to determine the phase composition of crystal structure in the perovskite samples. A glass microscope slide was used to press the fine powder into the sample holder and get a flat surface. The XRD scattering for the sample was measured in between 20°- 70°(2θ) at rate equal to 0.02°/s and Cu Kα radiation of (λ=1.54 Å). Additionally, a standard diffractogram $SmFeO_3$ with code number of (01-086-1330) [4] was employed by Rigaku PDXL Software to obtain the lattice parameters and to observe the effect of inserted lithium and generated vacancies in the $SmFeO_3$ lattice.

5. 2. 2. 2. *Scanning Electron Microscopy & Energy Dispersive X-ray Spectroscopy:*

The pellets were used to detect the microstructure morphology of the lithium perovskites using a JEOL JSM-7500F field emission scanning electron microscopy (FE-SEM) [5]. Two different modes (**LEI**) and (**COMPO**) were used for the samples in order to compare the surface morphology at different electron energies, **(LEI = 2 - 3 eV)** and **(COMPO = 15 - 20 eV)** [6]. The magnification for both modes was fixed at 1000X to get better image.

In combination with SEM, energy dispersive x-ray spectroscopy (EDS) was applied for the **COMPO** images in order to distinguish the elemental composition formed on the pellets surface. Though, the EDS results did not help in identifying Li composition because of its lower atomic number. Thus, these results were used to label the elemental compositions for the other elements Sm, Fe and O at different spots existing on the surface.

5. 2. 2. 3. *Ionic Conductivity Measurements:*

Princeton Applied Research PARSTAT 2273 instrument [7] and power suite software [8] were used to measure the lithium ionic conductivity for the second group of lithium perovskites. The impedance measurements were investigated at room temperature with a specific frequency range between 1 MHz and 100 Hz with sinusoidal wave amplitude of 10 mV. These measurements were interpreted to the Nyquist plot where x-axis represents the real value of impedance Z' and y-axis represents the imaginary value of impedance Z".

In addition, ZSimpWin software [9] was used to fit the actual AC data with an equivalent circuit model **$[LR_b(QR)_{gb}]$, figure (5. 1) ,** for all perovskites excluding $Sm_{0.4}Li_{0.4}FeO_{3-\delta}$. This perovskite cannot be fitted using **$[LR_b(QR)_{gb}]$** equivalent circuit due to the presence of the two arcs in the AC actual data. Therefore, another equivalent circuit was used, which is **$[LR_b(QR)_{gb}(Q_{dl}R_{ct})]$, figure (5. 2)**. The meaning of every elemental parameter in the equivalent circuit is presented in **table (5. 2)**. The lithium ionic conductivity was calculated by applying the bulk resistance in the equation shown below:

$$\textbf{\textit{The ionic conductivity}}\ (\sigma) = \frac{l}{R_b.\ a}\quad S.cm^{-1} \qquad [5.\ 1]$$

Where *l* is the thickness of the sample

R_b is the real resistance (bulk resistance)

a is the area of the pellet = $r^2 \times \pi$

r is the radius of the pellet

π is a constant value equals to 3.14.

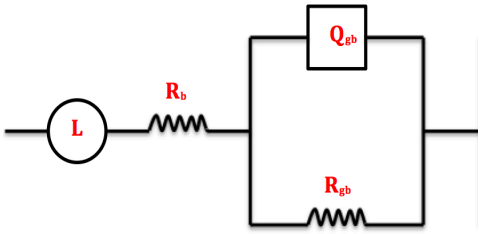

Figure 5. 1: Geometry of the equivalent circuit [$\mathbf{LR_b(QR)_{gb}}$].

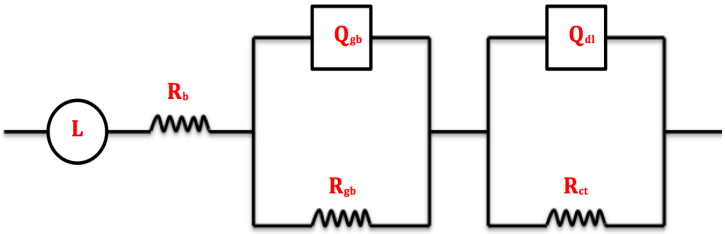

Figure 5. 2: Geometry of the equivalent circuit **[$\mathbf{LR_b(QR_{gb})(Q_{dl}R_{ct})$]**.

Table 5. 2: Randles Circuit Elements used in the model.

Equivalent element	Description	Impedance
L	Inductance	$j\omega L$
R	Resistance	R
Q	CPE (constant phase element)	$1/\ Y_0\ (j\omega)^{\alpha}$

Where j is the imaginary unit, $\omega = 2\pi f$ is the angular frequency, f is the frequency, Y_0 is the pre-factor of CPE and α is related to the frequency dispersion with the range of 0 to 1 the ($\alpha = 0 \Rightarrow$ Q = Resistance and $\alpha = 1 \Rightarrow$ Q = Capacitor)

5. 3. Results:

5. 3. 1. Powder X-ray Diffraction (PXRD):

PXRD was used to establish the effect of inserted Li ions and generated vacancies in the $SmFeO_3$ lattice. For each lithium perovskite sample, the XRD patterns at different

calcination temperatures (800°C, 1100°C and 1350°C) are presented from **figure (5. 3)** to **figure (5. 7)**. As seen from the figures, the crystal structure of the unit cell becomes arranged for the perovskite calcined twice at 800°C for 4 h. When the temperature is moved up to 1100C, the x-ray peak at 2θ = 28° is eliminated which is an impurity in the perovskite samples corresponding to the preparation method. For further increase in temperature to 1350°C, x-ray peaks become sharper and narrower with reduced intensities of the refraction peaks. This happened because the atoms in the crystal are undergoing thermal vibration about their mean position [10]. Thus, the size of crystal becomes larger due to the growth in grain size compared to the grain boundary.

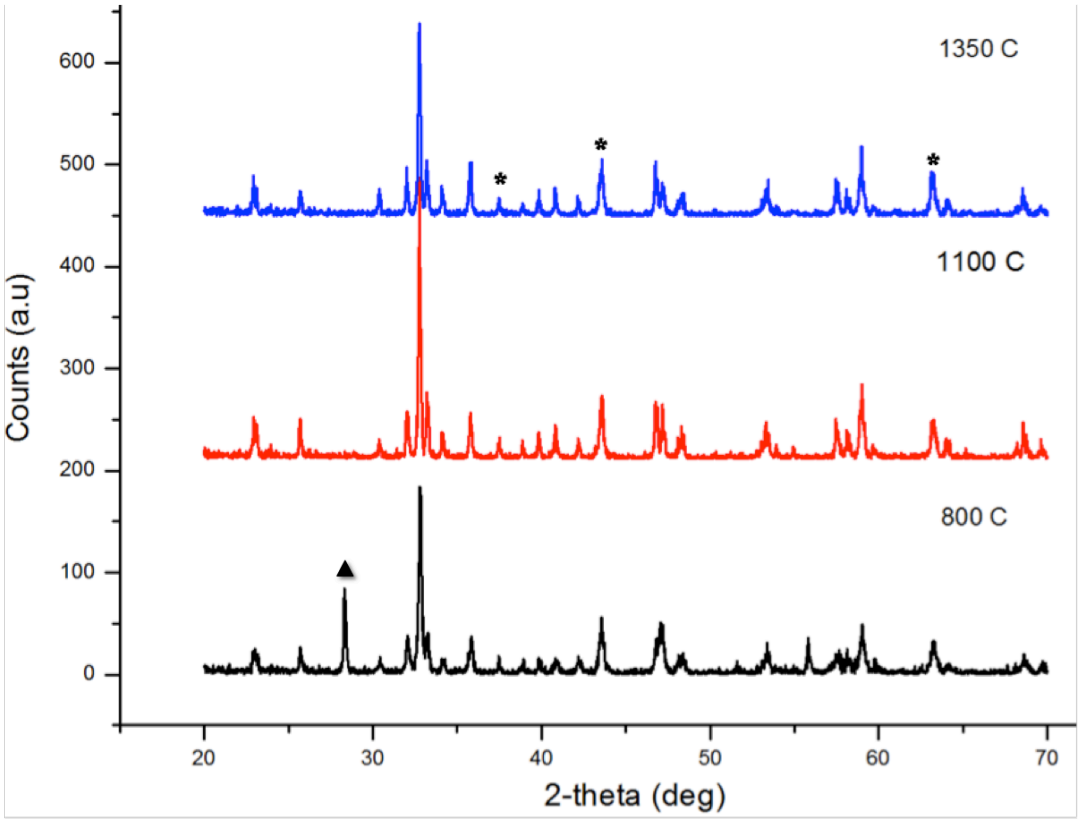

Figure 5. 3: The effect of increasing temperature on the peak position for $Sm_{0.3}Li_{0.6}FeO_{3-\delta}$, where * presents $LiFeO_2$ and ▲ presents the impurity phase.

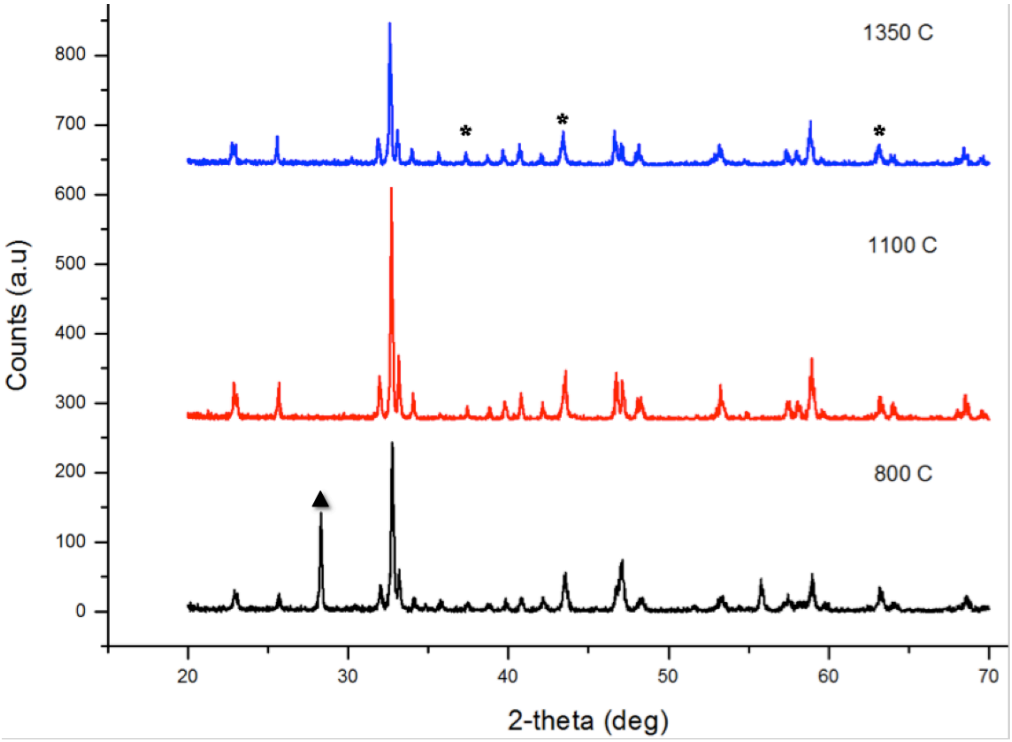

Figure 5. 4: The effect of increasing temperature on the peak position for $Sm_{0.3}Li_{0.5}FeO_{3-\delta}$, where * presents $LiFeO_2$ and ▲ presents the impurity phase.

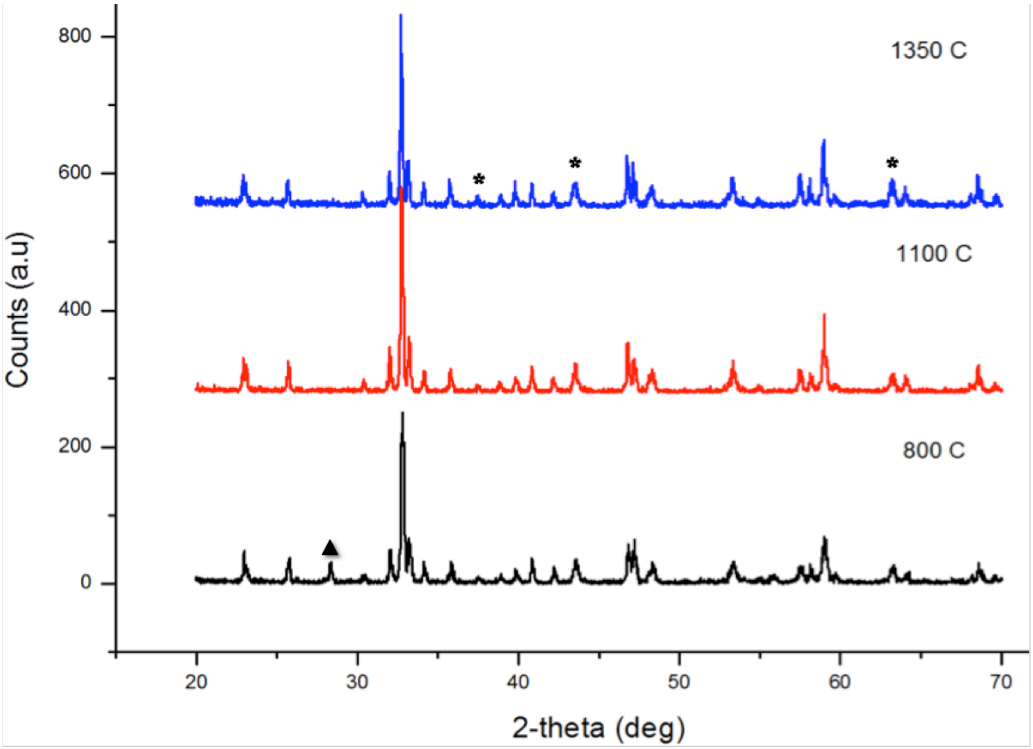

Figure 5. 5: The effect of increasing the temperature on the peak position for $Sm_{0.4}Li_{0.4}FeO_{3-\delta}$, where * presents $LiFeO_2$ and ▲ presents the impurity phase.

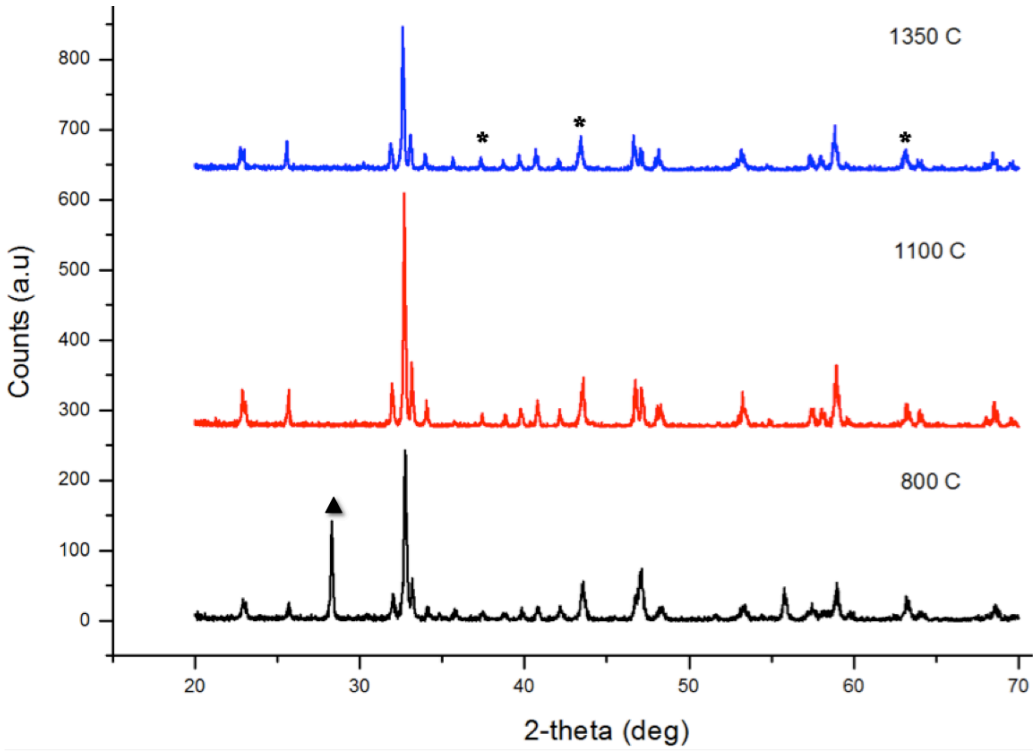

Figure 5. 6: The effect of increasing temperature on the peak position for $Sm_{0.5}Li_{0.3}FeO_{3-\delta}$, where * presents $LiFeO_2$ and ▲ presents the impurity phase.

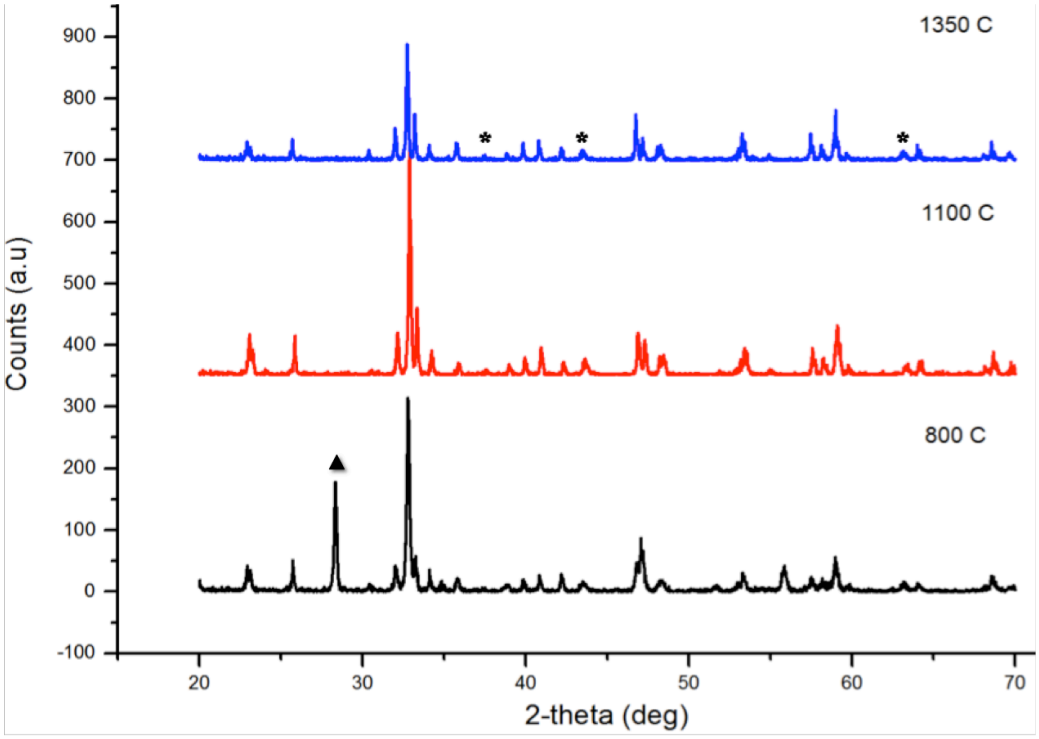

Figure 5. 7: The effect of increasing temperature on the peak position for $Sm_{0.6}Li_{0.3}FeO_{3-\delta}$, where * presents $LiFeO_2$ and ▲ presents the impurity phase.

Furthermore, the comparison between all the x-ray spectra's for the perovskite samples calcined at 1350°C, and the standard $SmFeO_3$ perovskite are presented in **figure (5. 8)**. In this figure, all the peaks existing in the standard $SmFeO_3$ perovskite also appear for all SLFO* perovskites. Therefore, the prominent phase is indexed to be $SmFeO_3$ with an orthorhombic structure and a space group of Pnma (62). Moreover, the lattice parameters for all SLFO* perovskites were corrected using the standard $SmFeO_3$ perovskite, as presented in **table (5. 2)**. However, two peaks at 2θ= 30.44 and 35.80 are observed which do not coincide to any recognised lithium compounds peaks. They may correspond to additional planes appearing as a result of inserting Li into $SmFeO_3$ lattice. Also, a separate phase of lithium iron oxide ($LiFeO_2$) (01-070-2711) [11] is also observed at 2θ = 37.52, 43.58 and 63.30 for SLFO* perovskite samples. Additionally, $LiFeO_2$ phase varies depending on the different amount of lithium ions inserted into the A-site for SLFO* perovskites. Hence, the SLFO* samples are composed of two phases, which are orthorhombic and cubic phases.

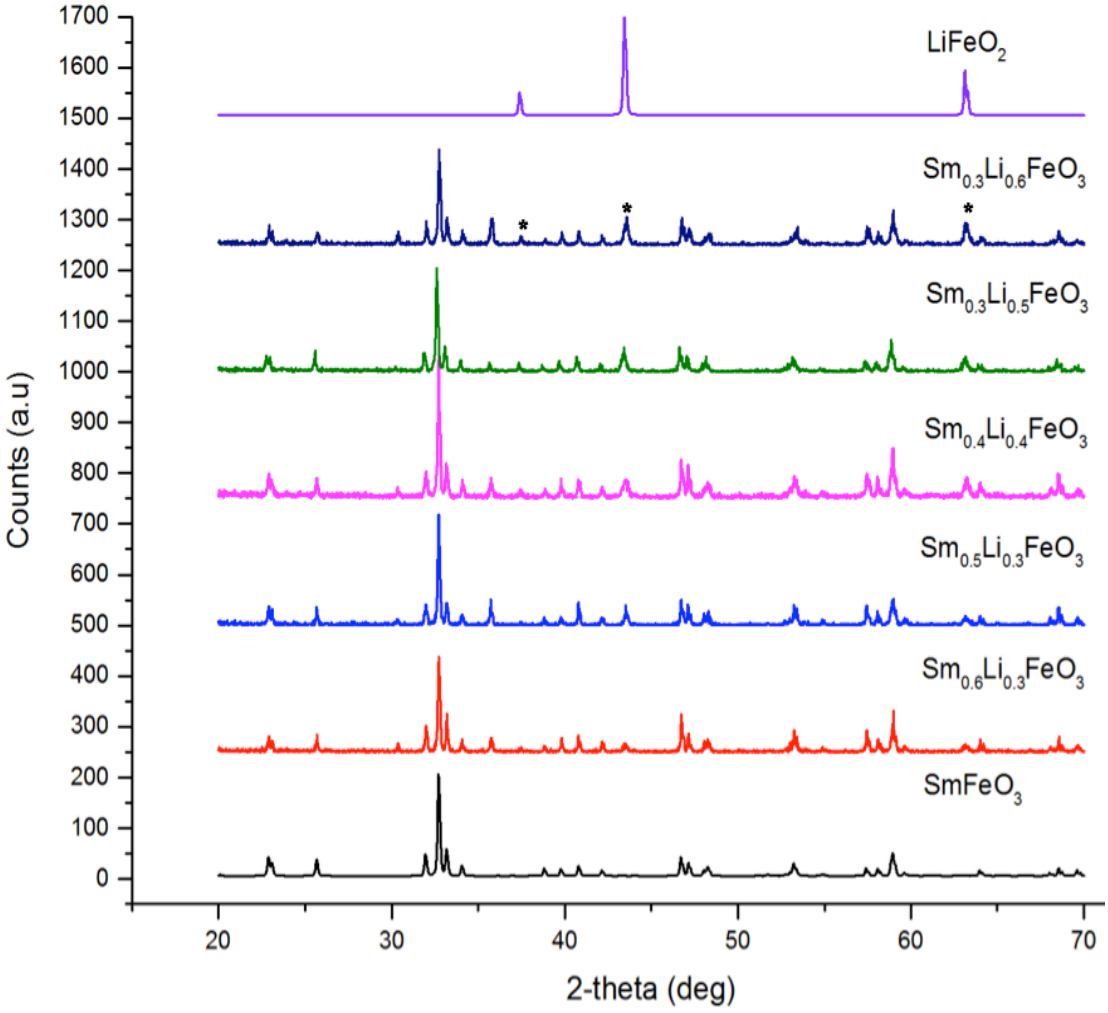

Figure 5. 8: Comparison of the XRD patterns for samples of increasing Li content fired at 1350°C with the Standard $SmFeO_3$ perovskite (01-086-1330) and $LiFeO_2$ phase (01-070-2711).

In **figure (5. 8)**, the highest peak around 2θ=32º presents the maximum intensity for all the perovskites. The magnification of this peak shows the peak shifts in SLFO* samples and the standard $SmFeO_3$, as shown in **figure (5. 9)**. In this chapter, vacancy concentration in addition to lithium and samarium concentrations is considered as the most important factor that effect the peak position. It is assumed to increase the 2θ value due to the vacancies in the crystal. Practically, most of (SLFO)* show an increase in the 2θ value to 32.72° for $Sm_{0.6}Li_{0.3}FeO_{3-\delta}$, $Sm_{0.5}Li_{0.3}FeO_{3-\delta}$ and

$Sm_{0.4}Li_{0.4}FeO_{3-\delta}$ perovskites as compared to SmFeO3 ($2\theta = 32.70°$). In addition, the value of 2θ is further increased to 32.74° for $Sm_{0.3}Li_{0.6}FeO_{3-\delta}$ perovskite due to the high amount of lithium ions (small ionic radii). On the other hand, $Sm_{0.3}Li_{0.5}FeO_{3-\delta}$ has huge shift to lower angle ($2\theta = 32.60°$), which is not easily explained by the high amount of vacancy and Li compared to the low amount of Sm. So, the shift to higher or lower angle value is not only due to the partial substitution of Sm with Li, but also due to the presence of vacancies, which distorts the lattice and decreases or increases the crystal volume, respectively, as seen in **table (5. 3)**. In this table, the lattice parameters and the volumes for each perovskite are corrected using the standard $SmFeO_3$.

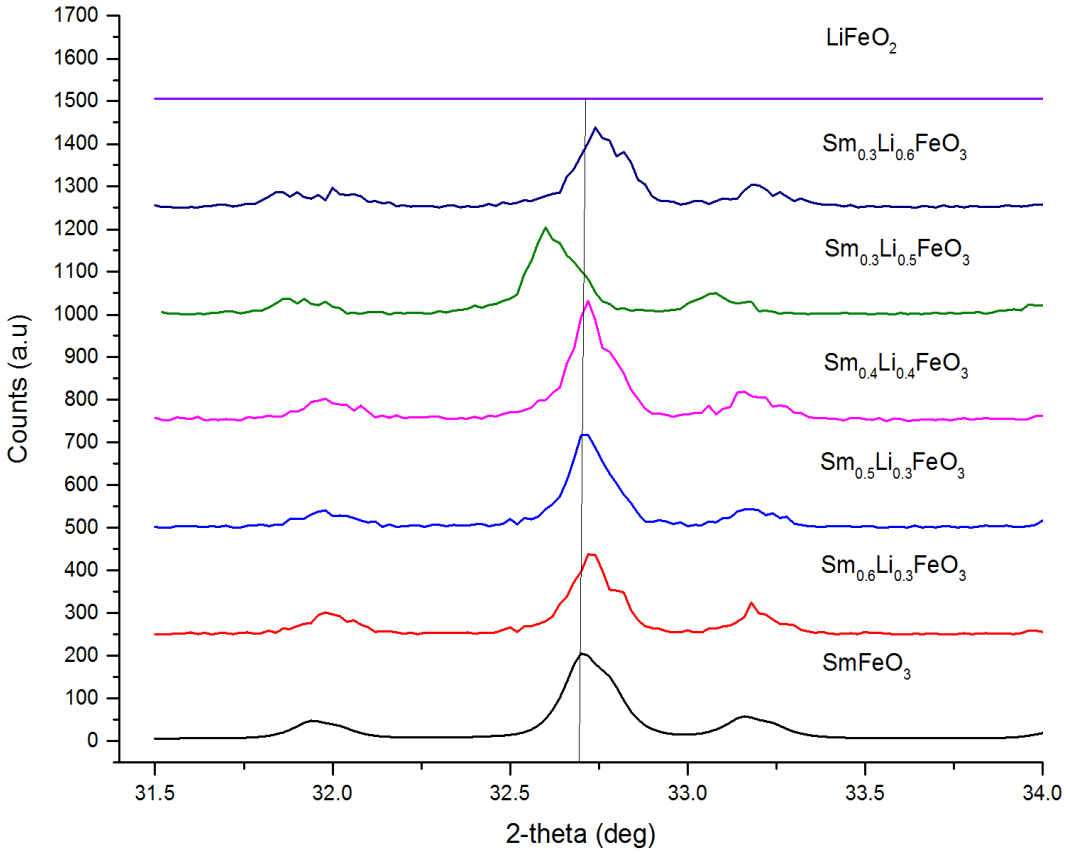

Figure 5. 9: Magnified region for the XRD patterns of all samples fired at 1350°C and the Standard $SmFeO_3$ perovskite (01-086-1330) and $LiFeO_2$ phase (01-070-2711).

Moreover, as mentioned in chapter 4, tolerance factor(t) is an important tool to check the stability of the perovskite structure.

$$\boldsymbol{t} = \frac{\boldsymbol{r_A + r_O}}{\sqrt{\boldsymbol{2}}\,(\boldsymbol{r_B + r_O})} \qquad [5.\ 2]$$

Where r_A = ionic radius of the A-site, r_B = ionic radius of the B-site and r_O = ionic radius of oxygen ion

The bound lengths of A-O and B-O that used to calculate tolerance factor are listed in the following equations:

$$d_{Sm-O} = 2.088 - 0.37 \log\left(\frac{x=3}{y=12}\right) = 2.601 \text{ Å} \qquad [5.3]$$

$$d_{Li-O} = 1.466 - 0.37 \log\left(\frac{x=1}{y=12}\right) = 2.385 \text{ Å} \qquad [5.4]$$

$$d_{Fe-O} = 1.759 - 0.37 \log\left(\frac{x=3}{y=6}\right) = 2.015 \text{ Å} \qquad [5.5]$$

Where 2.080, 1.466 and 1.759 are recommended bond valence parameters for Sm, Li and Fe, respectively [12]. 0.37 is an empirical constant and Log (x/y) =the logarithm of the ratio between the formal valance and the coordination number of A-site (12) and B-site (6). The results of these calculations are also given in **table (5. 3)**.

Table 5. 3: Present lattice parameters for the standard $SmFeO_3$ and the lithium perovskite samples after the corrections using the standard.

Perovskite Formula	A (Å)	B (Å)	c (Å)	Volume ($Å^3$)	Tolerance Factor (t)
$Sm_{0.3}Li_{0.6}FeO_{3-\delta}$	5.594(7)	7.692(9)	5.393(8)	232.0(5)	0.776
$Sm_{0.3}Li_{0.5}FeO_{3-\delta}$	5.606(9)	7.698(11)	5.412(14)	233.6(8)	0.692
$Sm_{0.4}Li_{0.4}FeO_{3-\delta}$	5.598(5)	7.702(7)	5.385(6)	232.2(4)	0.700
$Sm_{0.5}Li_{0.3}FeO_{3-\delta}$	5.597(4)	7.704(6)	5.393(8)	232.6(4)	0.708
$Sm_{0.6}Li_{0.3}FeO_{3-\delta}$	5.596(3)	7.701(4)	5.394(5)	232.4(3)	0.799
$SmFeO_3$	5.6001	7.7060	5.3995	233.01	0.91

From XRD analysis, it is possible to prove the presence of the impurity phase ($LiFeO_2$), which appeared due to the synthesis method, beside the perovskite phase $SmFeO_3$ in all SLFO* perovskites. In addition, the presence of vacancies and the partial substitution of Sm (big atom) with Li (small atoms) change the peak position to high or low angle compared with the standard phase $SmFeO_3$. This variation in the peak position is dependent on the vacancies, Li and Sm concentrations. The values of computed tolerance factors are in between 0.75 and 1 when the vacancy concentration = 0.1. This confirms the structure stability for the synthesised perovskites and their suitability to be used for commercial needs. However, the tolerance factor is less than 0.75 for the vacancy concentration of 0.2, thus,

suggesting unstable perovskite structure for $Sm_{0.3}Li_{0.5}FeO_3$, $Sm_{0.4}Li_{0.4}FeO_3$ and $Sm_{0.5}Li_{0.3}FeO_3$.

5. 3. 2. ***Scanning Electron Microscopy & Energy Dispersive X-ray Spectroscopy:***

Chapter 4 describes in detail the use of scanning electron microscopy to produce an image with the help of secondary electrons to give a three-dimensioned view of the image. It is employed here to observe surface morphologies of lithium perovskite pellets calcined twice at 1350°C for 6 h. **Figure (5. 10)** presents the microstructure morphology of $Sm_{(x)}Li_{([1-x]-[0.1]\text{ or }[0.2])}FeO_{3-\delta}$ (where x= 0.3, 0.4, 0.5 and 0.6). These images have similar results that were observed previously in chapter 4. The surface morphologies contain no pores and these holes are produced by a human error during the pressing process. In addition, theses lithium perovskites are presented in two different modes, which are **LEI** and **COMPO** modes, with a magnification of 1000x at room temperature. The **LEI** images show different size of nanoparticles on the surface while the **COMPO** images show light and dark particles, which correspond to two phases in the perovskite samples. Thus, **LEI** and **COMPO** images confirm the previous result observed by PXRD suggesting the presence of $LiFeO_2$ phase in these pellets.

LEI mode **COMPO mode**

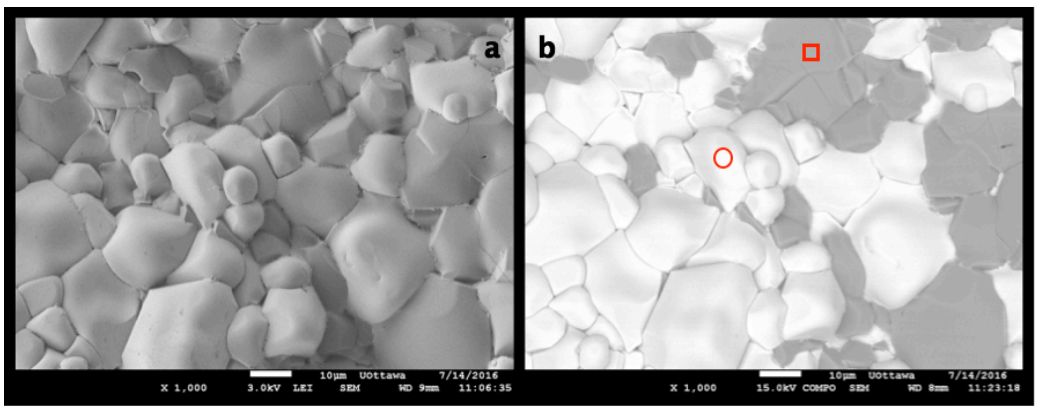

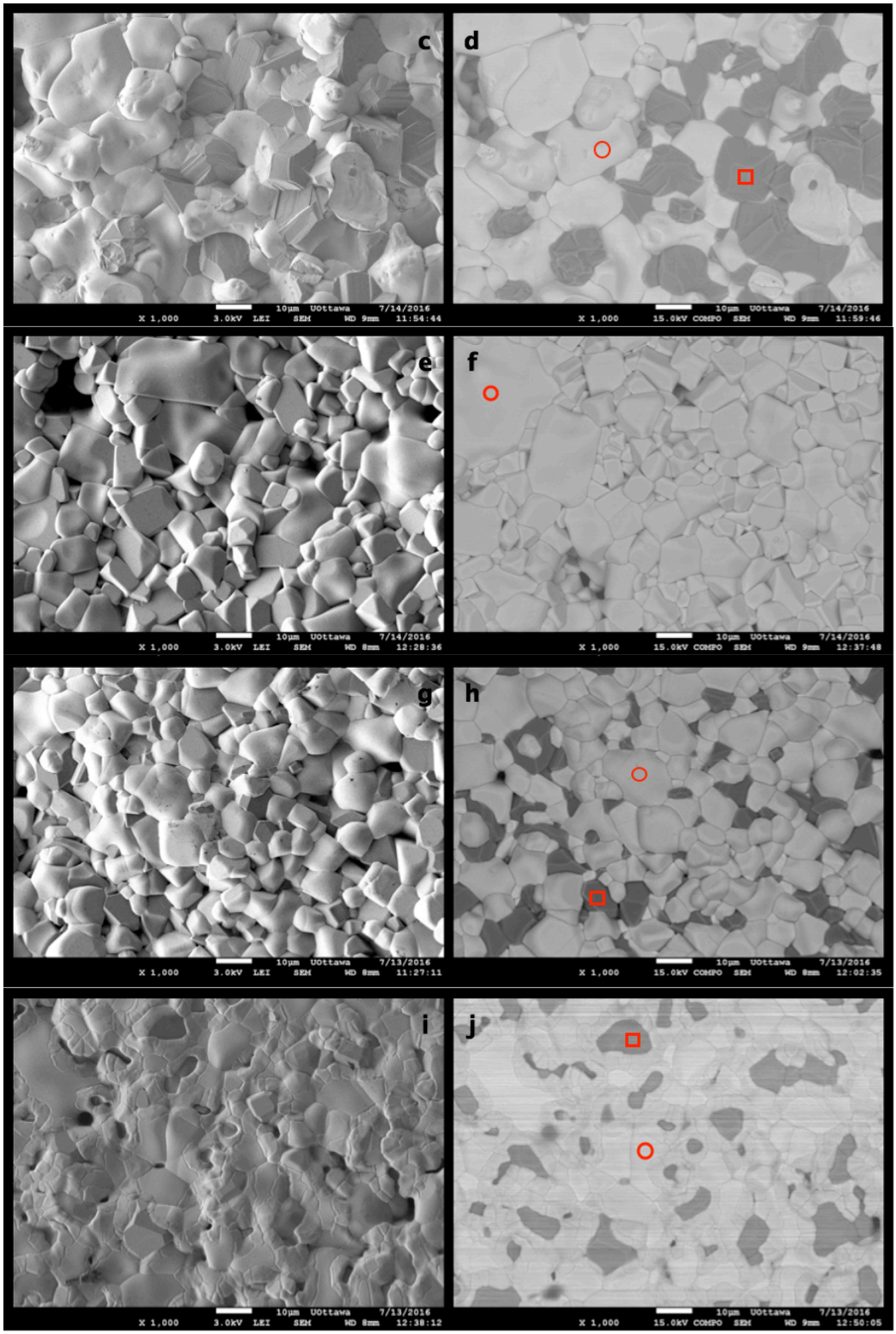

Figure 5. 10: SEM images for all SLFO* Perovskites presented in LEI and COMPO modes, a) and b) for $Sm_{0.3}Li_{0.6}FeO_{3-\delta}$, c) and d) for $Sm_{0.3}Li_{0.5}FeO_{3-\delta}$, e) and f) for $Sm_{0.4}Li_{0.4}FeO_{3-\delta}$, g) and h) for $Sm_{0.5}Li_{0.3}FeO_{3-\delta}$ and i) and j) for $Sm_{0.6}Li_{0.3}FeO_{3-\delta}$. a, c,

e, g, i obtained by LEI detection; b, d, f, h, j collected by COMPO detection. Areas marked in red correspond to locations where EDS measurements were performed.

From the images shown in the above figure, it is seen that at 0.3 mol of Sm and varying Li concentration to 0.5 and 0.6 mol, the surface morphology is unaffected. The dark particles appear bigger for Li=0.6 than at Li =0.5, which means there are more impurity phase in the former. The same result is also observed in terms of the surface structure when Li concentration is stabilized at 0.3 mol and Sm concentration is varied for 0.5 and 0.6 mol. However, the number of light particles are more for Sm= 0.6 than Sm = 0.5, which confirms that the amount of the perovskite phase is increased by increasing the Sm concentration. In the case of same concentration of Li and Sm (0.4 mol) at the A-sites of the perovskite structure, the surface morphology is completely changed and the particles almost have the same shape. Even the **COMPO** image shows the particles in the same color assuming that the impurity phase LiFeO2 is not detected by SEM. Conversely, the PXRD result still shows the impurity phase in the form of small peaks when the lithium and samarium have the same concentration in the perovskite.

Table 5. 4: EDS results obtained from COMPO images for the second group of SLFO*.

Perovskite formula	Dark Area □		Light Area ○	
	Element	**Atomic %**	**Element**	**Atomic %**
$Sm_{0.3}Li_{0.6}FeO_{3-\delta}$	O K	80.46	O K	74.73
	Fe K	19.72	Fe K	13.63
	Sm L	-0.18	Sm L	11.64
$Sm_{0.3}Li_{0.5}FeO_{3-\delta}$	O K	82.79	O K	70.04
	Fe K	16.85	Fe K	15.91
	Sm L	0.37	Sm L	14.05
$Sm_{0.4}Li_{0.4}FeO_{3-\delta}$	O K	Non	O K	75.09
	Fe K	Non	Fe K	12.52
	Sm L	Non	Sm L	12.39
$Sm_{0.5}Li_{0.3}FeO_{3-\delta}$	O K	79.28	O K	77.07
	Fe K	20.40	Fe K	11.33
	Sm L	0.32	Sm L	11.60
$Sm_{06}Li_{0.3}FeO_{3-\delta}$	O K	62.87	O K	45.57
	Fe K	36.82	Fe K	26.70
	Sm L	0.31	Sm L	27.73

The EDS analysis is used to investigate the kind of elements in the light and dark particles from the **COMPO** image. The result of this analysis is presented in **table (5. 4).** It is assumed that the perovskite phase would appear as the light particles since Sm scatter strongly because of its high atomic number and thus appear bright in the images. While the impurity phase of $LiFeO_3$ is assumed to appear as the dark particles because of the low atomic number of Fe as compared to Sm. However, as

discussed in chapter 4, lithium element cannot be distinguished by the EDS technique because of its **lower atomic number**

5. 3. 3. *Ionic Conductivity Measurements:*

Chapter 4 discusses that the ABO_3 perovskites could allow the charge transport and the conductivity because of the presence of the structure defects. The conductivity in the perovskites can be defined as an ionic and/or an electronic conductivity depending on the application that is used. In this chapter, the defects in the structure of the perovskite is not only due to the replacement of one or more atoms with either donors or acceptors atoms, e.g., replacing Sm^{3+} by Li^{+}, but also from the creation of vacancies in the A-sites. Theses vacancies are considered useful in increasing the lithium ionic conductivity in the SLFO* perovskite since there are a large amount of the unfilled vacant sites for Li ions to occupy and move freely.

The ionic conductivity measurements were determined using Electrochemical Impedance spectroscopy technique. Such a technique is beneficial to measure the ionic conductivity because it can distinguish between different resistance contributions such as bulk, grain boundary and electrode resistance. In this chapter, this spectroscopy technique was used to measure the ionic conductivities for all SLFO* perovskite pellets calcined at 1350°C for 6 h using two similar carbon based electrodes. The measurements were performed in a frequency range from 1 MHz to 100 Hz and a sine wave of (10 mV amplitude) at room temperature. The experimental set up for this arrangement is presented in chapter 3.

The AC data was analysed by the mean of the Randles equivalent circuit $\mathbf{[LR_b(QR)_{gb}]}$, for all the SLFO* perovskites except $Sm_{0.4}Li_{0.4}FeO_{3-\delta}$. This perovskite was analysed using another Randles equivalent circuit $\mathbf{[LR_b(QR)_{gb}(Q_{dl}R_{ct})]}$ because

its AC data has two semicircles and does not fits the first equivalent circuit [$\mathbf{LR_b(QR)_{gb}}$]. These circuits were used through the ZSimpWin software to investigate the circuit composition for all SLFO* samples. In addition, the Nyquist plots of AC impedance measurement data and AC impedance calculated data for all SLFO* perovskite pellets are presented in **figure (5. 11)**.

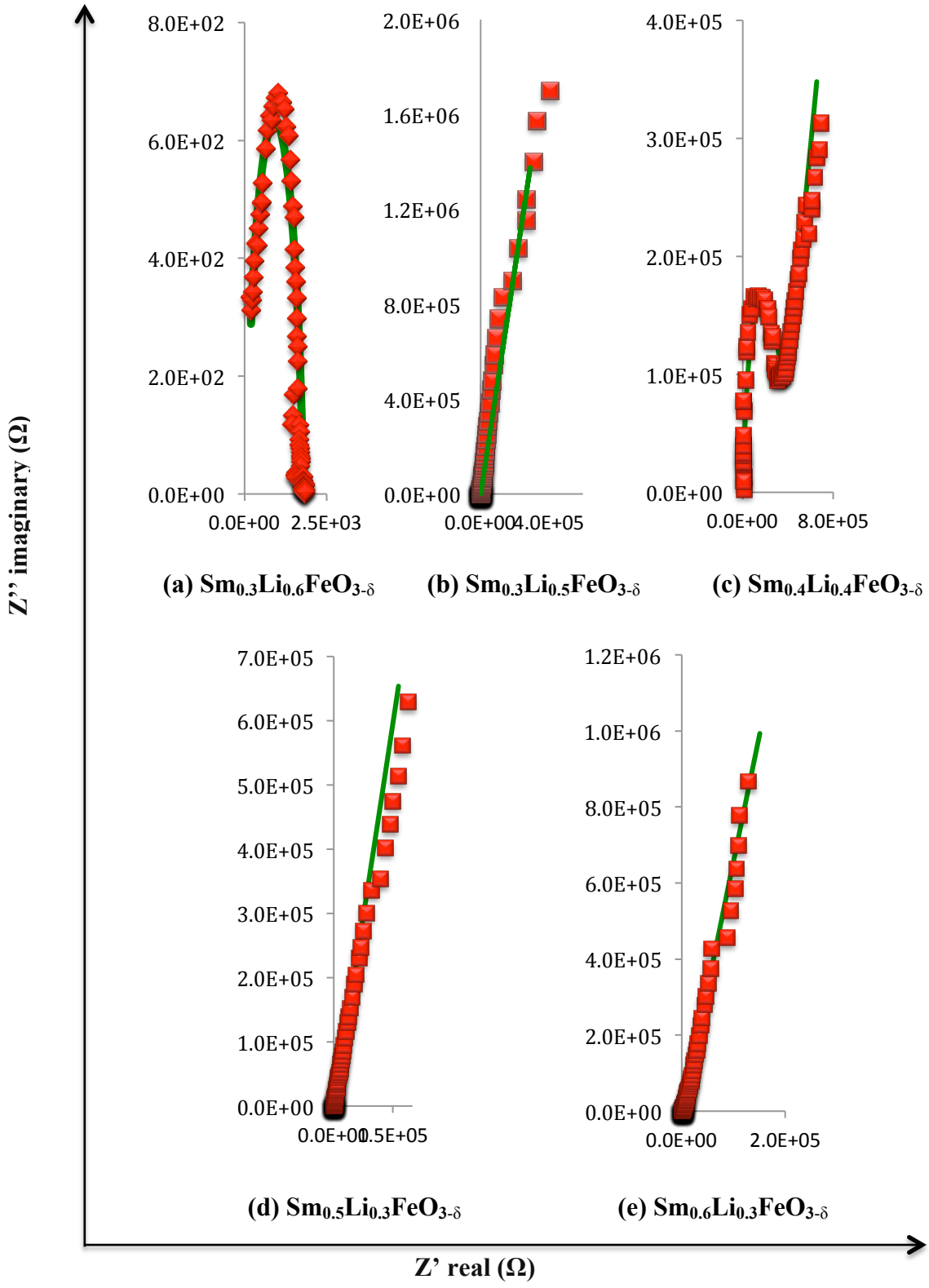

Figure 5. 11: Nyquist plots present the AC data measurement points in red color and the calculated fitting curve in green color for the second group of lithium perovskites SLFO* calcined at 1350°C for 6 h.

From **figure (5. 11),** it is possible to see different behaviour of these data depending on the Li, Sm and vacancies concentrations. For example, when the Sm concentration is stabilized at 0.3 and Li concentration is varied at 0.6 and 0.5, the curves show different features. In the case of vacancies generated for 0.4 mol of both Sm and Li concentrations, the AC measurement result shows two arcs for high and low frequencies. The fitting process for this perovskite cannot be completed using **[$LR_b(QR)_{gb}$]** equivalent circuit because of the presence of the second semicircle. As a result, additional **(QR)** parameters are added to previous equivalent circuit to get better fitting process which is **[$LR_b(QR)_{gb}(Q_{dl}R_{ct})$]**. The third criteria for generating vacancies as earlier discussed in this chapter is to stabilise the Li = 0.3 and vary the Sm = 0.5 or 0.6. The curves for both perovskites in **figure (5. 11. d)** and **figure (5. 11. e)** show linear behaviour, which is expected since the amount of the lithium concentration in both perovskites is the same.

Moreover, the values of the bulk resistance were obtained at high frequency region while the values of the grain boundary were obtained, as discussed in chapter 4, using the AC calculated data for all SLFO* perovskites since they cannot be directly obtained from the AC actual data. Thus, the calculated data is interpolated to obtain a semicircle, especially for $Sm_{0.3}Li_{0.5}FeO_3$, $Sm_{0.5}Li_{0.3}FeO_3$ and $Sm_{0.6}Li_{0.3}FeO_3$. The values of the component parameters in the equivalent circuits are provided in **table (5. 5)**. The $\mathbf{R_b}$ values were employed to calculate the lithium ionic conductivity for each perovskite using **equation [5. 1]** and the results are given in **table (5. 6)**. Also, the comparison between the lithium concentration for the perovskites and the ionic conductivities in (S/cm) that are shown in **figure (5. 12)**.

Table 5. 5: The calculation components of the equivalent circuit.

Perovskite Formula	L[a] (Ω.s)	R_b (Ω)	Q_{gb} (s/ Ω)	R_{gb} (Ω)	Q_{Id} (s/ Ω)	R_{ct} (Ω)
$Sm_{0.3}Li_{0.6}FeO_{3-\delta}$	5.13×10^{-19}	35.05	1.10×10^{-8}	1759	Non	Non
Rel. Std. Error (%)	5.86×10^{14}	13.89	20.59	1.806	Non	Non
$Sm_{0.3}Li_{0.5}FeO_{3-\delta}$	3.9×10^{-16}	183	2.40×10^{-9}	9.74×10^{14}	Non	Non
Rel. Std. Error (%)	1.40×10^{12}	16.8	5.678	3.919×10^{9}	Non	Non
$Sm_{0.4}Li_{0.4}FeO_{3-\delta}$	1.68×10^{-3}	1.13×10^{4}	1.51×10^{-11}	4.67×10^{5}	6.80×10^{-8}	3.16×10^{7}
Rel. Std. Error (%)	26.92	16.95	45.54	6.459	13.23	49.96
$Sm_{0.5}Li_{0.3}FeO_{3-\delta}$	2.35×10^{-17}	640.3	5.20×10^{-9}	1.39×10^{11}	Non	Non
Rel. Std. Error (%)	8.93×10^{17}	5.177	2.775	2.06×10^{8}	Non	Non
$Sm_{0.6}Li_{0.3}FeO_{3-\delta}$	2.79×10^{-16}	874.6	2.81×10^{-9}	1.13×10^{8}	Non	Non
Rel. Std. Error (%)	9.47×10^{12}	5.957	3.658	42.14	Non	Non

[a] Fitting of the inductance component is included here only for completeness, but the number of points in the fitting and the intrinsic nature of this data produce very large errors.

Table 5. 6: The lithium ionic conductivity calculation.

Perovskite formula	Real resistance Z' (Ω)	Pellet thickness *l* (mm)	Pellet Radius r (mm)	Ionic Conductivity α (S/cm)
$Sm_{0.3}Li_{0.6}FeO_{3-\delta}$	35.03	1.127	5.95	2.89×10^{-2}
$Sm_{0.3}Li_{0.5}FeO_{3-\delta}$	183	1.313	5.99	6.36×10^{-3}
$Sm_{0.4}Li_{0.4}FeO_{3-\delta}$	11300	1.123	5.97	8.89×10^{-5}
$Sm_{0.5}Li_{0.3}FeO_{3-\delta}$	640	1.437	6.17	1.88×10^{-3}
$Sm_{0.6}Li_{0.3}FeO_{3-\delta}$	874.6	1.84	6.11	1.80×10^{-3}

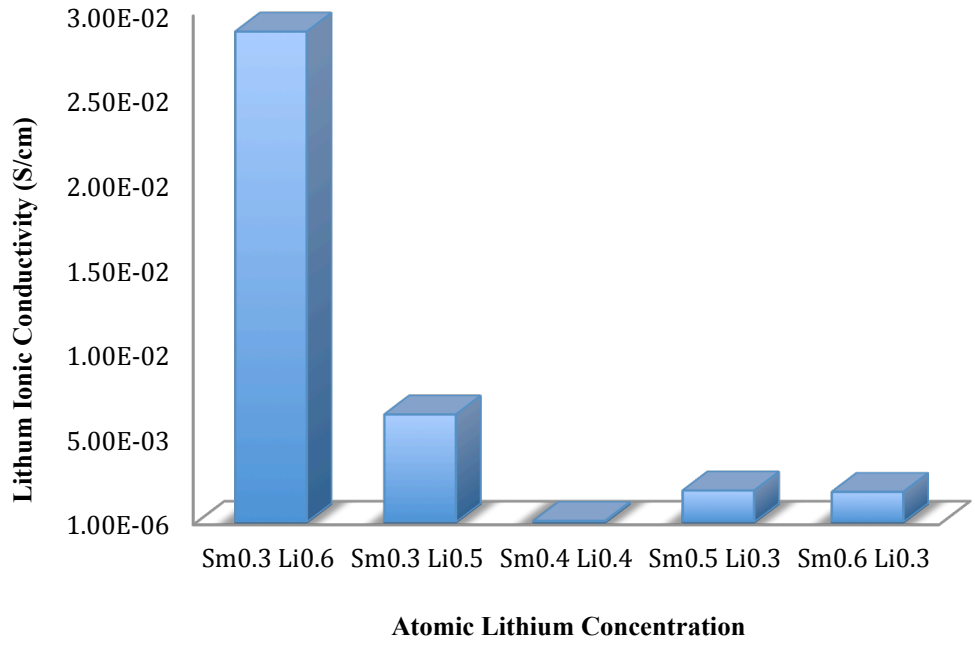

Figure 5. 12: Lithium Ionic conductivity and atomic lithium concentration for $Sm_{(x)}Li_{([1-x]-[0.1]\text{ or }[0.2])}FeO_{3-\delta}$, where (x = 0.3, 0.4, 0.5 and 0.6).

5. 4. Discussion:

In this work, SLFO* perovskites were synthesised using a solid-state reaction method (SSR) and employing two ways to generate vacancies. The first way of creating vacancies is by stabilizing the concentration of one of the cations (Sm or Li) and varying the other one. This approach helps to understand the differences in adding vacancies at the small atom (Li) site or the big atom (Sm) site. For example, at Sm=0.3, Li=0.6 and 0.1 mol of vacancy concentration, the perovskite shows higher conductivity with a value of 2.89×10^{-2} S/cm. While, when the Li concentration is reduced to 0.5 and the vacancy concentration is increased to 0.2, the lithium ionic conductivity is decreased to 6.36×10^{-3} S/cm. However, this result is still much higher than the ionic conductivity of other perovskites discussed in this chapter and the previous one. In addition, stabilizing the amount of Sm at 0.3 and varying the amount of Li to 0.6 and 0.5 is not changing the surface morphology much. However, at lithium = 0.6, the dark particles in the SEM images look bigger than that at Li = 0.5, which means there are more impurity phase at lithium = 0.6. The same result is also observed in term of the surface structure when lithium concentration is stabilized at 0.3 and samarium concentration is varied to 0.5 and 0.6. The light particles in this case are more at Sm= 0.6 than at Sm = 0.5, which confirms that the increase and the decrease in the amount of the impurity phase and the perovskite phase depends on the Li and Sm concentrations. However, the lithium ionic conductivity gives better result for Sm = 0.5 (1.88×10^{-3} S/cm) than for Sm = 0.6 (1.80×10^{-3} S/cm). The lower value of the ionic conductivity for $Sm_{0.6}Li_{0.3}FeO_{3-\delta}$ may be due to the low number of vacancies. In addition, it is known that the Sm atom has a high atomic size, which may take large space in crystal structure and thus hinder the movement of the lithium

ions towards the electrodes. This may also be the reason for less ionic conductivity for this perovskite.

The second way of generating vacancies is to create them at both lithium and samarium sites of $Sm_{0.4}Li_{0.4}FeO_{3-\delta}$ and observe the effect it has on the perovskite structure and the lithium ionic conductivity. In this case, the surface morphology is changed completely with respect to the other perovskites studied in this chapter. Also, the particles have almost the same shape, and show the same color in the **COMPO** image. Conversely, the PXRD result still shows small peaks for the impurity phase when the lithium and samarium have the same concentrations. The lithium ionic conductivity for this perovskite is calculated to be 8.89×10^{-5} S/cm, which is the lowest lithium ionic conductivity among the second group of perovskites (SLFO*).

5. 5. Conclusion:

In this chapter, the results and the discussion for the second group of the lithium perovskite materials with formula of $Sm_{(x)}Li_{([1-x] - [0.1] \text{ or } [0.2])}FeO_{3-\delta}$ (where x = 0.3, 0.4, 0.5 and 0.6) are presented in detail. The highest lithium ionic conductivity obtained for Li= 0.6 and Sm= 0.3 is 2.89×10^{-2} S/cm at room temperature. This result is higher than any previously reported value and than the ionic conductivity obtained for the perovskites studied in chapter 4. The high lithium ionic conductivity value of this perovskite is due to the large number of lithium ions (0.6) compared to samarium ions (0.3) and the generated vacancies. These vacancies exceedingly contribute to the conduction of lithium ions from one site to another. The amount of the impurity phase does not affect the lithium ionic conductivity significantly since the space in the lattice is adequate to permit the free movement of the lithium ions.

5. 6. References:

[1] Tilley, R. J., & Tilley, R. J. (2016). Diffusion and Ionic Conductivity. In Perovskites: structure-property relationships (pp. 159-162). Chichester: Wiley.

[2] Multipurpose X-ray diffraction system. (n.d.). Retrieved from http://www.rigaku.com/en/products/xrd/ultima

[3] Rigaku PDXL Software Version 1.8.0.3 Copyright 2007. (n.d.). Retrieved from http://manualzz.com/doc/6701023/rigaku-pdxl-software-version-1.8.0.3-copyright-2007.

[4] I. http://www.icdd.com/. ($SmFeO_3$) (01-086-1330).

[5] S. S. JSM-7500F Scanning Electron Microscope by JEOL USA. (n.d.). Retrieved from http://www.selectscience.net/products/jsm-7500f-scanning-electron microscope/?prodID=106753.

[6] Bukhari, S. M., & Giorgi, J. B. (2013). Ni doped Sm0.95Ce0.05FeO3−δ perovskite based sensors for hydrogen detection. Sensors and Actuators B: Chemical, 181, 153-158. doi:10.1016/j.snb.2013.01.073.

[7] European Virtual Institute for Speciation Analysis (EVISA). Princeton Applied Research - PARSTAT 2273. (n.d.). Retrieved from http://www.speciation.net/Database/Instruments/Princeton-Applied-Research/PARSTAT-2273-;i109.

[8] PowerSuite Software | Voltammetry | Princeton Applied Research. (n.d.). Retrieved from http://www.ameteksi.com/products/software/powersuite-software.

[9] ZSimpWin. (n.d.). Retrieved from http://www.ameteksi.com/products/software/zsimpwin.

[10] Vidal, K., Ortega-San-Martín, L., Larrañaga, A., Merino, R. I., Orera, A., & Arriortua, M. I. (2014). Effects of synthesis conditions on the structural, stability and ion conducting properties of Li0.30(La0.50Ln0.50)0.567TiO3 (Ln=La, Pr, Nd) solid electrolytes for rechargeable lithium batteries. Ceramics International, 40(6), 8761-8768. doi:10.1016/j.ceramint.2014.01.097

[11] I. http://www.icdd.com/. ($LiFeO_2$) (01-070-2711).

[12] Brese, N. E., & O'Keeffe, M. (1991). Bond-Valence Parameters for Solids . Acta Cryst, B47, 192-197. Retrieved October 3, 1990, from http://slapper.apam.columbia.edu/bib/papers/brese_acb91.pdf

Chapter 6

Conclusion and Recommendations

6.1. Conclusion:

In the present work, ten lithium ionic conducting perovskites were prepared using solid-state reaction method (SSR). This synthesis is done by the partial substitution of Sm^{3+} with Li^{+} in $SmFeO_3$ perovskite. The synthesized perovskites were characterized using different standard techniques to determine the crystal structure, surface morphology and their ionic conductivity. A brief introduction on ABO_3 perovskite type-oxides is presented in the first chapter. The second chapter emphasizes on the lithium-air batteries and their important applications in different fields of rechargeable batteries. This chapter also gives a review of recent literary works on the development of basic components (anode, electrolyte, cathode) of these batteries. The synthesis method and the characterization techniques employed for the preparation and analysis of these perovskites respectively is discussed in Chapter 3 while results and the discussion of the synthesised perovskites are described in Chapter 4 and 5.

The perovskites were divided into two groups depending on the existence of vacancies at the A-site of the lattice. The first group of lithium perovskite SLFO is prepared without vacancies to observe the effect of varying the Li and Sm concentrations on the lithium ionic conductivity. The highest lithium ionic conductivity that succeeded for this group of perovskites at room temperature is 4.60 $\times$ 10^{-3} S/cm for $\mathbf{Sm_{0.3}Li_{0.7}FeO_{2.3}}$. The value of highest lithium ionic conductivity obtained for the first group of perovskites is good, however, it is expected that this value would increase by creating vacancies in the perovskite lattice. This assumption

is proved as the highest lithium ionic conductivity obtained for the second group at room temperature is 2.89×10^{-2} S/cm for $\mathbf{Sm_{0.3}Li_{0.6}FeO_{3-\delta}}$. The ionic conductivity of this perovskite is greater than the highest lithium ionic conductivity published previously for lithium lanthanum titanate (LLTO). Thus, we can conclude that this perovskite is a suitable candidate for the protective film and/or the electrolyte in lithium-air rechargeable batteries.

6. 2. Recommendation:

Despite the highest lithium ionic conductivity obtained for $\mathbf{Sm_{0.3}Li_{0.6}FeO_{3-\delta}}$ in this work, there are still a number of challenges to overcome. The suggestions to solve the current problems are as following:

- It is reported that the impurity phase ($LiFeO_2$) appears as a result of using solid-state reaction method. So, changing the reaction method, for example, to sol-gel method can eliminate any impurity phases and provide a pure perovskite phase in the sample. Such a pure perovskite phase can provide higher ionic conductivity more than what is realized until now.
- The lithium ionic conductivities for some perovskites are quite low. A good option is to increase the sintering temperature to 1400°C or 1450°C, which can lead to grain growth and thus increase the ionic conductivities.
- Varying the Li, Sm and vacancy concentrations can provide more lithium ionic conducting perovskites.

Appendix I

This section is added to present the additional information that was not included in the rest of the document. In addition, it presents the oral presentation and poster presentations that made during this period of study.

I. 1 List of perovskite materials:

In addition to the SLFO perovskites, there are number of perovskites-type oxides that were prepared using solid-state reaction method. These perovskites, listed in **table [I.1]**, are not good candidates for lithium-air batteries because they show diferent behaviors in terms of PXRD peaks, instability at high sintering temperatures and no ionic conductivity. Moreover, another student (Faith Leroux) in the Giorgi lab worked on the same group of SLFO perovskite with the aim to obtain single phases. She successfully synthesized pure SLFO perovskites using sol-gel reaction method.

Table I.1: List of the materials that prepared during this study period.

Number	Perovskite formula	Reason for not being used
1	$Ce_{0.3}Li_{0.7}FeO_{2.7}$	The position of PXRD peaks is changed completely by increasing the sintering temperature
2	$Ce_{0.5}Li_{0.5}FeO_{2.5}$	The position of PXRD peaks is changed completely by increasing the sintering temperature
3	$Ce_{0.7}Li_{0.3}FeO_{2.3}$	The position of PXRD peaks is changed completely by increasing the sintering temperature
4	$Ce_{0.3}Li_{0.7}TiO_{2.7}$	The position of PXRD peaks is changed completely by increasing the sintering temperature
5	$Ce_{0.5}Li_{0.5}TiO_{2.5}$	The position of PXRD peaks is changed completely by increasing the sintering temperature
6	$Ce_{0.7}Li_{0.3}TiO_{2.3}$	The position of PXRD peaks is changed completely by increasing the sintering temperature
7	$Sm_{0.3}Li_{0.7}TiO_{2.7}$	The pellet is melted after calcination at 1350°C for 6 h
8	$Sm_{0.5}Li_{0.5}TiO_{2.5}$	Not show any ionic conductivity
9	$Sm_{0.7}Li_{0.3}TiO_{2.3}$	Not show any ionic conductivity

I. 2 Oral presentations

- I presented an oral seminar at the university of Ottawa as one of the requirements to get the master degree. The seminar was about $ABO_{3-\delta}$ perovskite type-oxides as cathode materials for intermediate temperature solid oxide fuel cells.

I. 3 Poster presentations

- I presented a poster showing results shown here in chapter 4 work at the Ottawa Carlton Chemistry Institute day 2016.

Appendix II

List of Figure Permissions

- **Figure 1. 4**

Title: Enhancing Electrocatalytic Activity of Perovskite Oxides by Tuning Cation Deficiency for Oxygen Reduction and Evolution Reactions

Author: Yinlong Zhu, Wei Zhou, Jie Yu, et al

Publication: Chemistry of Materials

Publisher: American Chemical Society Date: Mar 1, 2016

- **Figure 2. 1**

Title: Lithium−Air Battery: Promise and Challenges

Author: G. Girishkumar, B. McCloskey, A. C. Luntz, et al

Publication: Journal of Physical Chemistry Letters

Publisher: American Chemical Society

Date: Jul 1, 2010

- **Figure 2. 3**

Title: Lithium−Air Battery: Promise and Challenges

Author: G. Girishkumar, B. McCloskey, A. C. Luntz, et al

Publication: Journal of Physical Chemistry Letters

Publisher: American Chemical Society

Date: Jul 1, 2010

- **Figure 2. 4**

Title: Improved Cycling Performance of Lithium–Oxygen Cells by Use of a Lithium Electrode Protected with Conductive Polymer and Aluminum Fluoride

Author: Jae-Hong Kim, Hyun-Sik Woo, Won Keun Kim, et al

Publication: Applied Materials Publisher: American Chemical Society

Date: Nov 1, 2016

- **Figure 2. 5**

Title: A Metal-Free, Lithium-Ion Oxygen Battery: A Step Forward to Safety in Lithium-Air Batteries

Author: Jusef Hassoun, Hun-Gi Jung, Dong-Ju Lee, et al

Publication: Nano Letters

Publisher: American Chemical Society

Date: Nov 1, 2012